



2018

# Hydrophobicity of Low Temperature Vibrating Surfaces

Christian Fergusson

Follow this and additional works at: <https://scholarscompass.vcu.edu/etd>

 Part of the [Materials Science and Engineering Commons](#), and the [Mechanical Engineering Commons](#)

© Christian Fergusson

---

Downloaded from

<https://scholarscompass.vcu.edu/etd/5589>

This Thesis is brought to you for free and open access by the Graduate School at VCU Scholars Compass. It has been accepted for inclusion in Theses and Dissertations by an authorized administrator of VCU Scholars Compass. For more information, please contact [libcompass@vcu.edu](mailto:libcompass@vcu.edu).

# **Hydrophobicity of low temperature vibrating surfaces**

A thesis submitted in partial fulfillment of the requirements for the degree of Master of Science  
at Virginia Commonwealth University.

By

Christian P. Fergusson

Director: Dr. Reza Mohammadi

Assistant Professor, Department of Mechanical and Nuclear Engineering

Virginia Commonwealth University

Richmond, Virginia

August 2018

## **Acknowledgements**

I would like to express great appreciation for my advisor Dr. Reza Mohammadi for the support, encouragement, and wisdom he tirelessly provided.

I would also like to generously thank my committee members Dr. Ravi Hadimani and Dr. Dmitry Pestov for their time and advice.

As well, I have much gratitude for my friends at the Advanced Functional Materials Laboratory, Mehran Abolghasemibizaki and Ashton Bressler, whose collaboration and spirit were invaluable.

## Table of Contents

Acknowledgements.....	ii
Table of Contents.....	iii
List of Figures .....	iv
List of Tables .....	vi
Abstract.....	vii
Chapter 1 Introduction .....	1
Chapter 2 Experiments.....	6
2.1. Sample Preparation .....	6
2.2. Room Temperature Test Design .....	9
2.3. Sub-Zero Temperature Test Design.....	15
Chapter 3 Results and Discussion.....	22
3.1. Room Temperature .....	22
3.2. Sub-zero Temperature.....	28
Chapter 4 Conclusions .....	30
Chapter 5 Future Recommendations.....	31
References.....	32
Appendix A Microcontroller Code .....	35
Appendix B Publications .....	62



## List of Figures

<b>Fig. 1.1.</b> The contact angle formed by the surface of the liquid and the surface of the solid. Used courtesy of Shirtcliffe <i>et al.</i> [19] .....	2
<b>Fig. 1.2.</b> The two primary regimes of a sessile droplet. ....	2
<b>Fig. 1.3.</b> SEM imaging cross-section of soot coating. Used courtesy of Esmerlyan <i>et al.</i> [25] .....	4
<b>Fig. 2.1.</b> Chimney system for soot stabilization. Figure created by Christian Fergusson, used courtesy of Esmerlyan <i>et al.</i> [25] .....	6
<b>Fig. 2.2.</b> Modified chimney for tuning oxygen levels in combustion. ....	7
<b>Fig. 2.3.</b> Current revision of soot deposition system. Figure created by Christian Fergusson, used courtesy of Esmerlyan <i>et al.</i> [25] .....	8
<b>Fig. 2.4.</b> Diagram of room-temperature phase experimental setup. ....	9
<b>Fig. 2.5.</b> Room-temperature phase experimental setup. Note that the camera is not in place as shown. The large LED fixture above the setup was only used in preliminary trials and not in the final videos. ....	10
<b>Fig. 2.6.</b> The custom-built LED back light. ....	14
<b>Fig. 2.7.</b> Freezer phase experimental setup (cut-away view). ....	16
<b>Fig. 2.8.</b> The freezer is shown with the door and syringe in place, and the power supply, function generator, and amplifier are shown in the bottom right of the photo. ....	18
<b>Fig. 2.9.</b> Freezer door shelf with channel and plug. ....	19
<b>Fig. 2.10.</b> Model of the 3D-printed substrate. The flat-head style bolts will rest in the V-shaped notches, with the cantilever preventing water from potentially freezing the substrate to the acrylic bridge. ....	20

- Fig. 3.1.** The contact time of a 10  $\mu\text{L}$  droplet as a function of frequency given constant wave amplitude. The dashed line represents the line of best fit, showing a strong negative correlation ( $R^2 = 0.8253$ ). ..... 22
- Fig. 3.2.** The contact times of 10  $\mu\text{L}$  droplets as a function of frequency. (a) The total contact time. (b) The duration of the retracting phase of the impact. (c) The duration of the spreading phase. The effect of the vibration is more pronounced in the spreading phase, though the variance impedes practical assessment. .... 24
- Fig. 3.3.** The contact times of (a) 20  $\mu\text{L}$  droplets and (b) 30  $\mu\text{L}$  droplets as a function of frequency, with linear trend lines. Polynomial trend lines were a closer fit, though the data was too limited to properly extrapolate their accuracies. .... 25
- Fig. 3.4.** The contact times of 10  $\mu\text{L}$  droplets as a function of impact phase. The dashed line represents the polynomial best fit, which correlates with the expected trend well, but correlates very poorly with the experimental data. .... 27
- Fig. 3.5.** The mass of ice accreted on uncoated hydrophilic substrates and coated superhydrophobic substrates, at both  $-20\text{ }^{\circ}\text{C}$  and  $-30\text{ }^{\circ}\text{C}$ . The variation shows that the coating and temperature had significant effects, while the impact of the vibration on the results was unclear. .... 28

## List of Tables

<b>Table. 2.1.</b> Room-temperature phase experimental setup. ....	11
--	----

## **Abstract**

### **HYDROPHOBICITY OF LOW TEMPERATURE VIBRATING SURFACES**

By Christian P. Fergusson

A thesis submitted in partial fulfillment of the requirements for the degree of Master of Science at Virginia Commonwealth University.

Virginia Commonwealth University, 2018

Major Director: Reza Mohammadi, Assistant Professor, Department of Mechanical and Nuclear Engineering

This study proposes a method to enhance the anti-icing capabilities of superhydrophobic surfaces by utilizing vibration to further reduce contact time of an impacting droplet in addition to keeping the droplet in the Cassie-Baxter regime, where surface adhesion is lower than the opposing Wenzel regime. We tested this with two methods: by investigating the effects of vibration normal to the plane of a superhydrophobic surface being impacted by water droplets in a room temperature environment, with the surface horizontal in a room temperature environment and tilted in a sub-zero degree environment. The amplitude and frequency of the vibration were varied in our experiments. Our results show that the mean contact time of a 10 $\mu$ L droplet consistently decreased linearly as the vibration frequency increased, though the standard deviations drastically increased. The ice accretion in the second phase of the testing also had significant variance, which obfuscated any reliable trend from the introduction of vibration.

## Chapter 1 Introduction

Ice accretion is not only a source of inefficiency in certain industries such as bio-fouling of sensors [1,2] and increased drag of shipping and research vessels [3,4], as well as wind farms [5–7], but also a potential danger in some, like aviation [8–10]. Yet most research to date investigates ice removal technologies rather than prevention of accretion in the first place. These removal methods all rely on the accretion before removal can occur, and so require that the negative effects of ice must be experienced, even if briefly. As well, these are all active methods that require actuation under certain conditions and often need significant electricity to power. An effective ice prevention system could be completely passive and would negate the problems of icing entirely.

Superhydrophobic surfaces have proven to assist in preventing icing by shortening the contact time of water droplet impacts [11,12] as well as reducing the surface adhesion forces [13,14], enabling the self-cleaning nature of such surfaces [15–17] to prevent ice from crystallizing on the surface [18]. The primary metric associated with hydrophobicity is the contact angle  $\theta$  (Fig. 1.1) which is formed between the surface of the liquid and the surface of the solid upon which it rests [19]. A surface is considered hydrophobic if this angle is greater than  $90^\circ$ , which occurs in materials with low surface energy, and hydrophilic if less than  $90^\circ$ , which occurs in materials with higher surface energy. A superhydrophobic surface, one with a contact angle greater than  $150^\circ$ , is achieved by adding surface asperities to a material which is already hydrophobic. These asperities provide a platform for a water droplet to rest upon (Fig. 1.2), and impingement is avoided due to the surface tension of the droplet overpowering the attraction of the low surface energy and resisting being pulled into the gaps – known as the Cassie-Baxter state. If the droplet does impinge on the geometry – the Wenzel state – the droplet has wet the surface and will no longer behave superhydrophobically [19]. Further enhancement of the anti-wetting properties of a

superhydrophobic surface can be achieved by supplementing it with other techniques, including vibration, in order to repel the droplet before impingement can occur or to introduce enough energy to eject the droplet despite impingement.

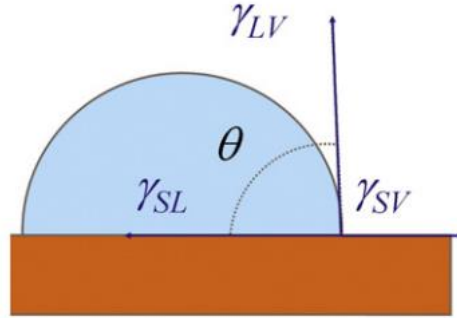


**Fig. 1.1.** The contact angle formed by the surface of the liquid and the surface of the solid. Used courtesy of Shirtcliffe *et al.* [19]

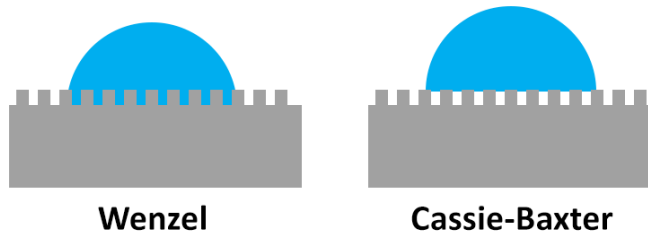


**Fig. 1.2.** The two primary regimes of a sessile droplet.

The dynamics of the impact of a water droplet on a surface can be viewed from multiple perspectives. The contact time  $\tau$  is the duration of the contact between the droplet and the solid surface during the impact. It generally scales with the inertial-capillary time scale, which is given as  $\tau_0 = \sqrt{\rho R_0^3 / \gamma}$  in which  $\rho$  is density,  $R_0$  is the radius, and  $\gamma$  is surface tension [20]. Given that ice nucleation is a function of duration of contact with the surface, reducing the contact time is the primary mechanism for preventing ice accretion. Another metric that heavily affects impact dynamics is the Weber number, which represents the influence of the fluid's inertial force compared to its surface tension. The dimensionless Weber number is formulated as

$We = \rho V^2 R_0 / \gamma$  in which  $V$  is the impact velocity [20]. The Weber number plays a role in the severity of the impact, with higher values indicating more likelihood of shearing on contact. For investigations like this one which focus solely on water as the fluid, only the droplet size and the impact velocity will control the final value. This study prioritized a high impact velocity in order to simulate real-world conditions, with three sizes of droplets to enable exploration of the effect of differing Weber numbers on the results.

The current state of the art has shown that vibration of superhydrophobic surfaces has been used to augment the Cassie-Wenzel wetting process as well as to induce Wenzel-Cassie dewetting depending on the conditions of the system. The driving factor that determines the preferred direction of the regime change is the critical contact angle, which is based on the balance of surface roughness and the solid surface fraction, which is the fraction of the solid's surface area that is wet by the liquid. This threshold represents the divide between a material upon which a droplet will find the Cassie-Baxter regime energetically favorable and one which finds the Wenzel regime more favorable [19,21]. The transition of a droplet from one regime to another occurs under both vertical and horizontal substrate vibrations on a sessile droplet due to increased LaPlace pressure or inertial forces from the droplet, depending on whether the vibration frequency was near or far from the resonance frequency of the drop [22]. Finally, vibration has been demonstrated to increase the freezing time of a sessile droplet due to the extra time taken wetting the surface before freezing begins, though the opposite effect could be prompted by tuning the surface vibration frequency to the resonant frequency of the droplet [23]. *None of the studies so far, however, have investigated the effects of vibration on droplet impacts in freezing conditions.*

A goal of this investigation is to facilitate development of a passive anti-icing system. The previous studies researching active systems focused on higher-power mechanisms, like ultrasonic

vibration. While these have been proven effective at removing a variety of ice, a passive system must use little or no extra energy. This study focuses on lower frequencies – up to 300 Hz – in search of a solution that can run off of the byproducts of other systems. An airplane wing, for example, might be tuned such that its aerodynamics give it an inherent vibration at a frequency conducive to anti-icing. With high-power systems, this would be insufficient and resorting to electrical or other inputs would be necessary.

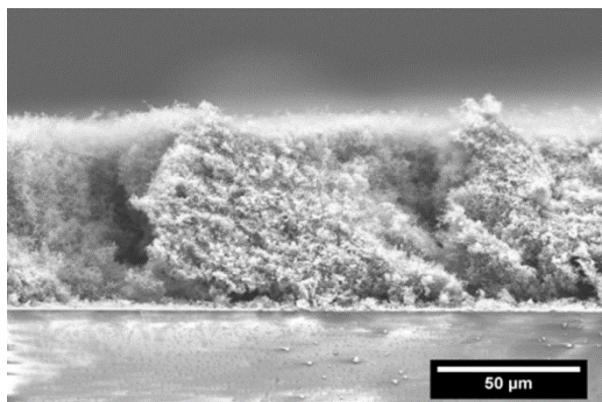


**Fig. 1.3.** SEM imaging cross-section of soot coating. Used courtesy of Esmerlyan *et al.* [25]

Our lab previously developed an improved method of synthesizing a superhydrophobic coating using the soot from the combustion of rapeseed oil upon a paper wick, which produced the inherently stable coating shown in Fig. 1.3 by lowering the levels of oxygen in the combustion using a specially-designed cone-shaped chimney [24,25]. This produced soot consisting of dense carbon chains, and the resulting superhydrophobic coating showed mechanical and thermal stability as well as being easily applied to a wide range of substrate materials without damage. The chimney was further refined to include an adjustable inlet for tuning of the oxygen levels, which allowed for further control over the morphology of the resultant coating – producing amorphous, graphitic-like and diamond-like phases [26]. A chemical functionalization stage was appended to the coating process by immersion in an ethanol bath and brief drying phase followed



by a bath in a fluorocarbon solution and another drying phase. The additional operations gave the soot coating greatly increased mechanical strength and surface adhesion [27].

We first investigated the effects of vibration of varying frequency (static, 20-300 Hz) and constant displacement (0.5 mm) on droplets impacting a superhydrophobic surface. We then investigated the effect of vibration of varying frequency (static, 20-300 Hz) and constant input power (0.028 W) on the anti-icing capabilities of a tilted superhydrophobic surface. From that, this study proposes that vibration can further enhance the anti-icing capabilities of a superhydrophobic surface impacted by water droplets.

## Chapter 2 Experiments

### 2.1. Sample Preparation

Superhydrophobicity was achieved by coating a solid substrate with soot produced from the incomplete combustion of rapeseed oil. The system used was based on the chimney-modified combustion processes previously developed in our lab, which included functionalizing the coating with an Ethanol bath followed by a perfluorocarbon bath.

The basic design as outlined in Fig. 2.1 consists of a Pyrex dish containing a pool of approximately 50 mL of rapeseed oil, in the center of which is a paper-based wick. This wick is ignited and then covered by an aluminum chimney in order to decrease the oxygen content in the combustion. Holding a solid object 7 cm above the opening of the chimney for approximately 5 s will collect upon it a soot coating with a high fraction of  $sp^3$  hybridized carbon. The resulting coating exhibited static contact angles around  $153\text{-}156^\circ$  and contact angle hysteresis of  $0.7\text{-}1.2^\circ$ . This method for obtaining a superhydrophobic surface is remarkably simple and quick and can be applied to virtually any solid material.

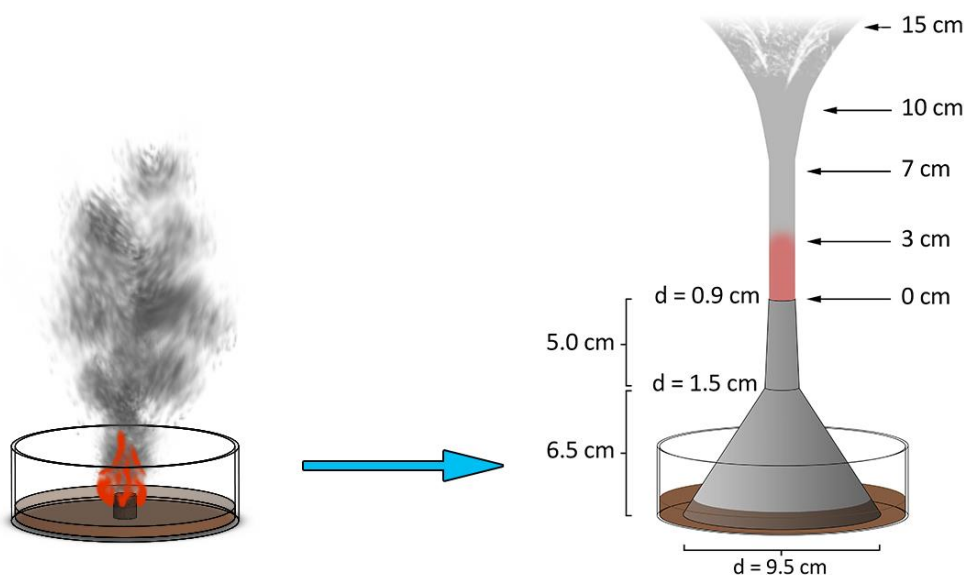


**Fig. 2.1.** Chimney system for soot stabilization. Figure created by Christian Fergusson, used courtesy of Esmeryan *et al.* [25]

Further research led our lab to improve the process by designing an adjustable air inlet to the chimney in order to tune the air-to-fuel ratio, and therefore the morphology of the soot produced. This chimney was formed by rolling aluminum foil into a cone shape and cutting the appropriate hole in the bottom edge, based on the dimensions given in Fig. 2.2. A matching sleeve was formed with a slightly wider hole in order to provide a means of adjusting the width of the opening, resulting in different combustion temperatures. This allowed for adjustment of the fraction of diamond-like, graphite-like, and amorphous carbon ratios.

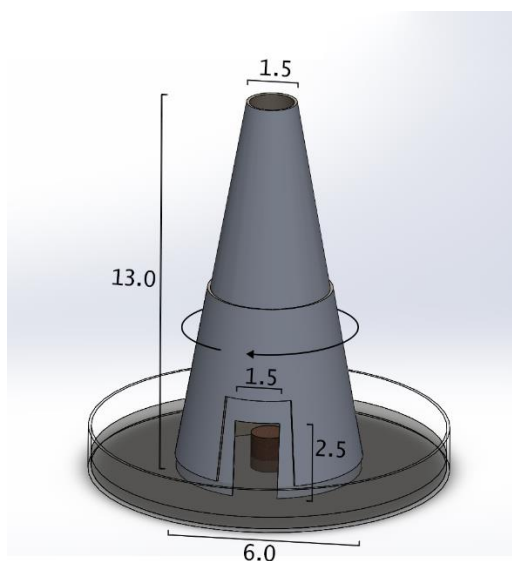


**Fig. 2.2.** Modified chimney for tuning oxygen levels in combustion.

A final upgrade to the coating process involved replacing the passive air inlet with an active intake, displayed in Fig. 2.3. An air compressor (Intex Quick-Fill 12v-DC), powered by a standard computer power supply (Antec BP550 PLUS), was connected through an adjustable flow meter (McMaster Carr 5079K25) to a specially modified tin funnel acting as a chimney (McMaster Carr 8996T12). Sealed to the funnel with high-temperature stove cement (McMaster Carr 7573A31) was a 20 cm aluminum tube with inner diameter of ~1.1 cm. The flow meter could adjust the air-

to-fuel ratio of the combustion by fine-tuning the flow to the flame from 0.00047 to 0.00519 m<sup>3</sup>/min, giving much finer control than the chimney with sleeve.

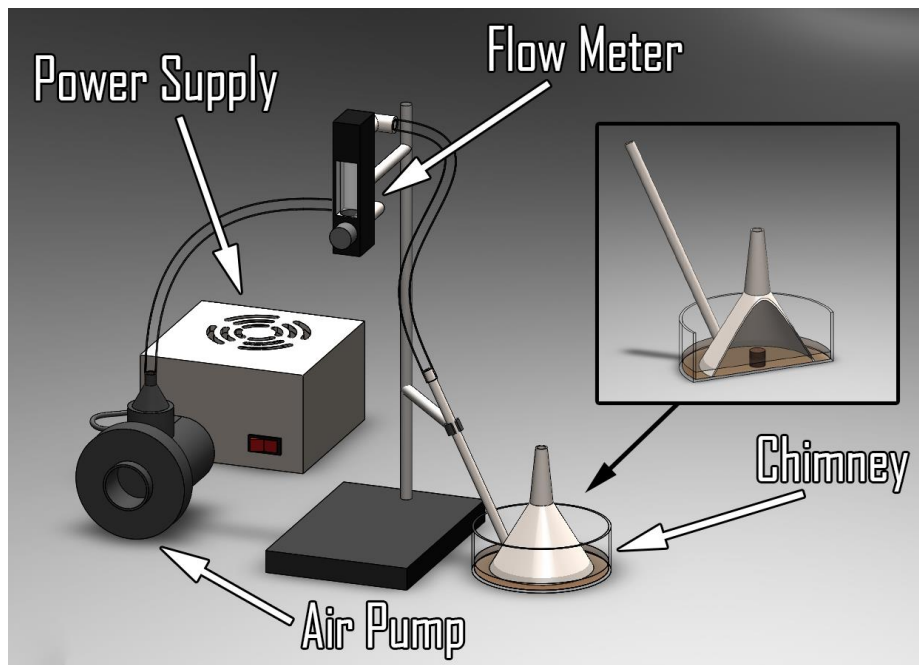


**Fig. 2.3.** Current revision of soot deposition system. Figure created by Christian Fergusson, used courtesy of Esmeryan *et al.* [25]

To further enhance the soot coating, a chemical functionalization process was applied to newly coated substrates. Subsequent to coating, the sample was submerged in ethanol (99%, Sigma-Aldrich, USA) for approximately 5 seconds, and then dried under a 250 W heat lamp (Feit Electric, USA) for 5 seconds. Finally, the substrate was submerged in a perfluorocarbon solution (Grangers Performance Proofer, UK) diluted 1:7 with de-ionized (DI) water for 10 min, followed by another 20 s under the heat lamp. This provided a robust and stable surface with high contact angle and low hysteresis (advancing and receding contact angles of  $166.2 \pm 2.6^\circ$  and  $164.1 \pm 1.2^\circ$  respectively using DI-water) [20].

The first phase of the experiment utilized soot-covered glass as the substrate due to its high availability. For the second phase, because of the need for a secure mount and the ability to quickly

release the substrate for mass measurement, we employed soot-covered 3D-printed PLA blocks in order to implement a shape that could be consistently secured accurately and which would only require removal of a single bolt in order to detach from the speaker system. The PLA blocks were polished with 600 and then 1200 grit sand papers (Allied High Tech Products Inc., USA) and then sonicated in DI-water for 30 min prior to coating with soot.

## 2.2. Room Temperature Test Design

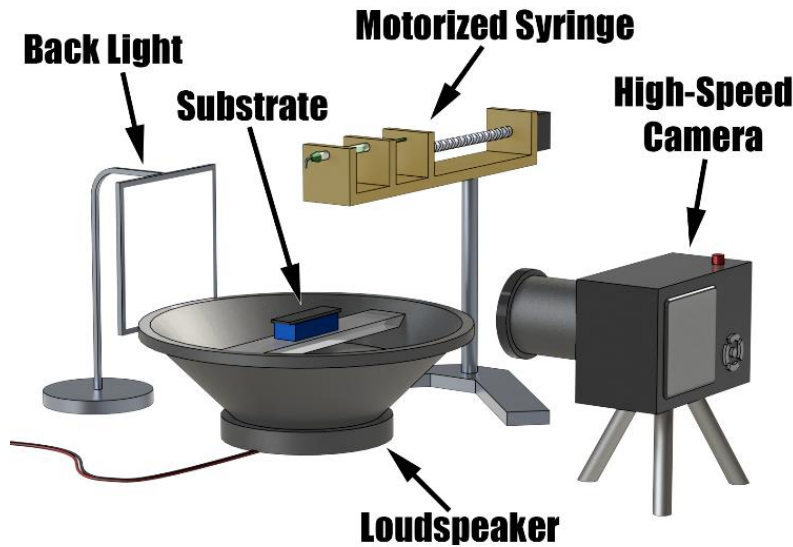


**Fig. 2.4.** Diagram of room-temperature phase experimental setup.

Initially, a baseline of the effects of frequency on the interaction of droplets impacting a superhydrophobic surface at room temperature must be gathered. The model of the room-temperature setup configuration is depicted in Fig. 2.4 and was in the general lab environment, including temperature around 21 °C and relative humidity around 40%. For this, a single droplet of de-ionized (DI) water is released from a motorized syringe onto a substrate coated with the aforementioned soot and functionalization procedure, which would be either static or vibrating. The interaction would be recorded with a high-speed camera in order to measure the various critical metrics of the interaction, primarily the contact time. The impact was observed for 20

repeat trials for any given set of circumstances – frequency from 0 Hz to 300 Hz in 20 Hz increments and droplet sizes of 10, 20 and 30  $\mu\text{L}$ . Subsequent to each drop, vibration would be ceased and the surface would be gently cleaned with a puff from a can of compressed air.

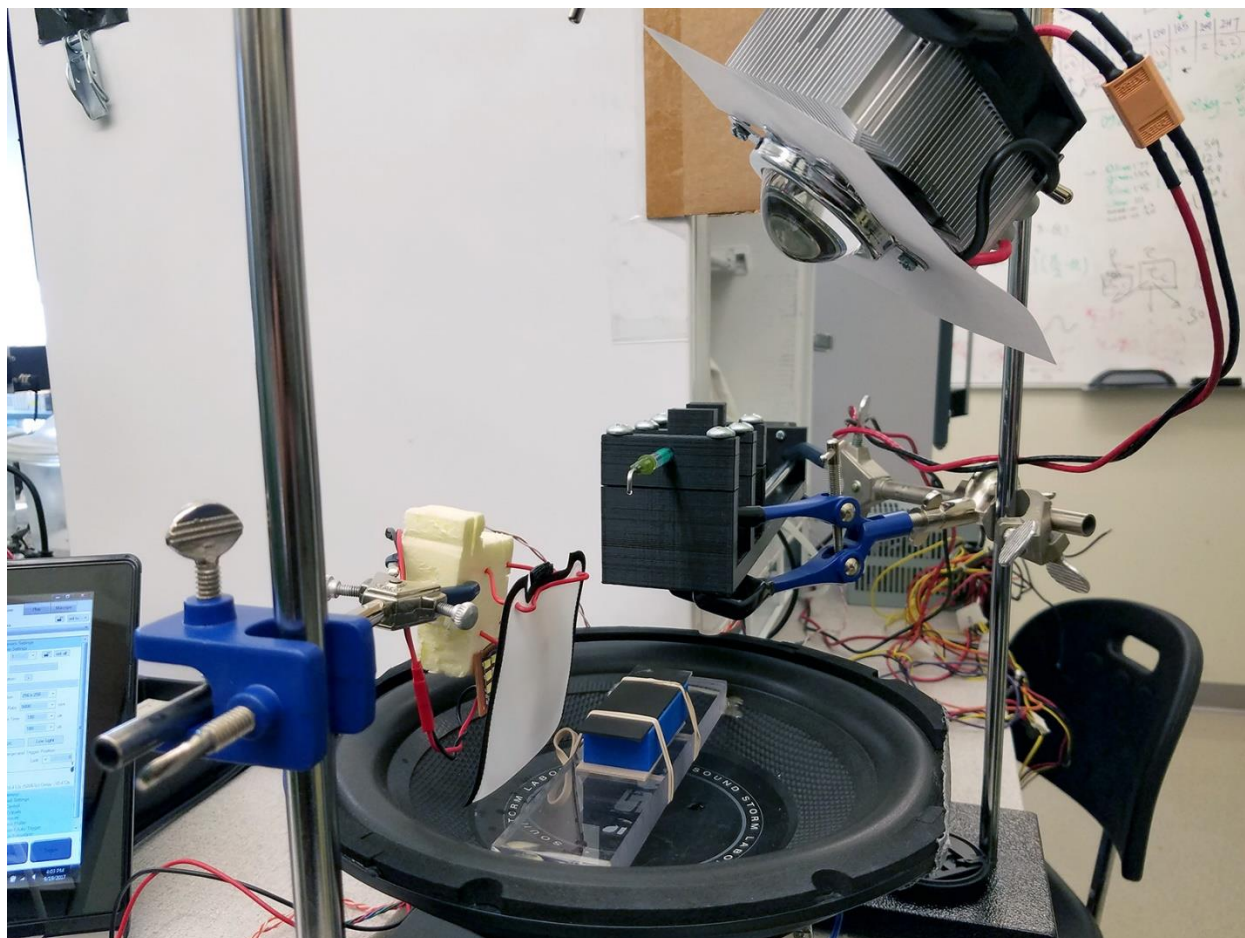


**Fig. 2.5.** Room-temperature phase experimental setup. Note that the camera is not in place as shown. The large LED fixture above the setup was only used in preliminary trials and not in the final videos.

In order to produce the vibration of the substrate, it was attached to the cone of a car-audio subwoofer (Sound Storm Laboratories SSL10, 10 inch 4-ohm single coil), normal to the direction of vibration, displayed in Fig. 2.5. The speaker was connected to a car-audio amplifier (Boss R1100M), which was fed a regular sine wave from a function generator (NI myDAQ). For the first phase, the amplitudes at each frequency were adjusted to normalize the vibration displacement to approximately  $0.5 \pm 0.02$  mm in order to determine the effect of frequency as energy input

increased. This was determined by estimating an output voltage that might produce the necessary displacement, recording the vibration along with the tip of a line gauge for scale, and analyzing the video using a physics analysis software (Tracker, physlets.org) to determine the actual displacement. The voltage was then adjusted in the direction of the desired displacement, and this was repeated until within the allowed tolerance of the goal displacement. The distance of 0.5 mm was selected in order to use the highest displacement possible (to ensure the effects of the vibration were apparent) while remaining below the approximate order of magnitude of the droplet size ( $10\ \mu\text{L} = \sim 1.34\text{mm}$  radius). The tolerance selected was, in this case, the nearest attainable given the resolution of the voltage adjustment of the function generator. The resultant amplitudes are shown in Table 2.1.

**Table 2.1.** Amplitudes used at each frequency to reach approximately 0.500mm of speaker displacement.

Frequency (Hz)	Amplitude (V)	Displacement (mm)
20	0.06	0.505
40	0.17	0.481
60	0.47	0.485
80	1.00	0.499
100	1.80	0.474
120	2.40	0.499
140	3.50	0.514
160	4.00	0.480
180	4.80	0.502
200	6.30	0.489
220	8.00	0.480
240	4.90	0.499
260	3.00	0.493
280	2.85	0.504
300	2.50	0.497

The superhydrophobic substrate was formed by coating a glass microscope slide (75 x 25 mm) using the soot process previously outlined, followed by the functionalization process. The slide was affixed with standard rubber bands to an acrylic bridge mounted with epoxy across the cone of the speaker. With a 3D-printed PLA spacer measuring 55 mm long, 25 mm wide, and 15 mm tall placed between the slide and the acrylic bridge, the rubber bands were wrapped around all three and tied in a knot. The acrylic bridge was designed approximately 40 mm wide, 12 mm tall, and 170 mm long in order to provide a platform elevated enough with the spacer to view directly from the side for measurement purposes, while being wide enough to accommodate possible future adjustments to the experiment, thin enough to reduce impact on the vibration, and thick enough to not risk fracture in possible future experiments. Due to the durability of the soot coating, the slide was used for the 20 trials at a particular frequency and droplet size, and then changed for another one in order to preempt possible degradation of the slide from droplet impacts, vibration, or contamination. Regardless, there was no visible deterioration upon removal.

The droplets were ejected onto the substrate from a specially-built motorized syringe system in order to maintain consistent ejection rates as well as avoid the premature droplet ejection due to shaking that a handheld system would induce. The syringe system consisted of a 1.0 mL syringe (BRAND) fitted with 25-, 20-, and 14-gauge right-angle needles to produce droplets around 10, 20, and 30  $\mu\text{L}$  respectively. This syringe was press-fit into slots in a 3D-printed base with its plunger affixed in a similar manner to a 3D-printed carriage. Both prints were formed in an extruder-type printer using PLA plastic, with an infill of at least 50% in order to reduce flexing of the components. The carriage rides via linear bearings – press-fit into the printed holes – along guide rails and is driven toward or away from the syringe cylinder by a lead screw (1 mm thread pitch), allowing for filling or ejection of the syringe. A stepper motor (Thomson Industries Inc.,



NEMA 14, 0.88A) attached through a motor driver (Big Easy Driver, Schmalz Haus LLC) to a microcontroller (Arduino Uno) drives the screw for precise movement of the carriage down to 0.0055  $\mu\text{L}/\text{step}$ , for this particular syringe.

The code developed for this microcontroller controls the motor at 1/16th steps (3200 steps/revolution), the finest resolution possible for this motor driver, by pulsing the output of the microcontroller to logic HIGH as briefly as possible and then leaving the output at logic LOW for a calculated duration that equates to a number of steps per second, as input by the user via the buttons and screen (Sainsmart 101-50-104) also connected to the microcontroller. For this room-temperature experimental phase, the speed was set to 1000 steps per second, which equated to an ejection rate of 5.5  $\mu\text{L}/\text{sec}$ , to reduce movement of the droplet during formation as much as reasonably possible and therefore produce more precise impact locations and impact velocities. Further details can be found in the source code in Appendix A.

This syringe system was mounted using a generic laboratory ring stand to release the droplet from 85 mm above the substrate. This particular height was chosen as it would provide the largest impact velocity possible (1.18 m/s) while still fitting inside of our freezer system in the second phase of the experiment, allowing the height to be consistent between the two experiment phases. Having a high impact velocity provides results more relevant to the potential applications of this surface, by emphasizing the dominance of the inertial forces over the surface tension forces which occurs in both high-speed impacts or impacts with larger droplets.

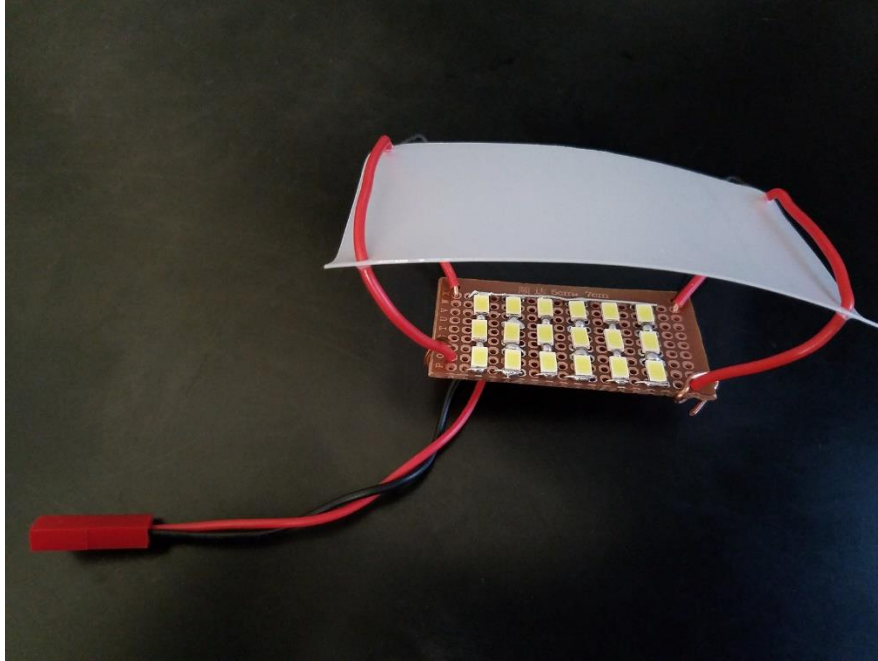


**Fig. 2.6.** The custom-built LED back light.

Motion of the droplet impact was recorded using a Phantom Miro eX2 high speed camera with a Tokina Macro 100 F2.8D lens recording at 5000 fps (256 x 256 pixel resolution), and from these videos, the contact times were observed and recorded. The tripod was positioned such that the lens was slightly elevated from the plane of the substrate so that a clear view of the exact time of the droplet contact could be determined, and 10-20 mm from the edge of the speaker to get as close as possible while also giving a slight buffer of space to prevent contact. Fig. 2.6 shows the custom-built back light that was used to provide a pure white background to the video and to illuminate the droplet clearly. This was fabricated from 50 x 30 mm perfboard with 18 cool-white 5730 SMD LEDs in 6 columns of 3 LEDs in series with a 47-ohm resistor each, powered by the same computer power supply as the speaker. Affixed approximately 20 mm in front of the LEDs using single-core 16 AWG wire was a 100 x 50 mm flat section cut from a milk-carton to act as a diffuser for the LEDs. This back light device was positioned using a lab ring stand to be directly behind the substrate from the camera, at a distance of approximately 25 mm from the edge of the substrate.

### *2.3. Sub-Zero Temperature Test Design*

The freezing-temperature phase of the experiment was designed to resemble conditions of an aircraft wing in flight – repeating droplets impacting a sub-zero-temperature surface and determining the mass of ice accreted in the process. Water at freezing temperatures can maintain a liquid state if there are no nucleation sites. The water suspended in the atmosphere at flight altitudes will often be a supercooled liquid, in some cases at temperatures as low as  $-40\text{ }^{\circ}\text{C}$  [28,29]. The creation of supercooled water is trivial. However, manipulating such a fluid without triggering freezing is quite a sensitive affair. A comprehensive solution must be developed in order to test droplet impacts in such circumstances, and for this reason, our exploratory investigation need not reach such depths. Seeking a simpler solution, the second phase of the investigation will leave the water in a syringe at room-temperature while releasing droplets onto a sub-zero surface. It compares the results of superhydrophobic and hydrophilic surfaces, two different temperature environments, and impact with a static substrate as well as one vibrating at a low (20 Hz) and a high (220 Hz) frequency. The extensive time required for each cycle of cooling and warming limited us to running 3 trials with any given set of parameters, for a total of 36 runs.

Prior to a run, the substrate mass (with superhydrophobic soot coating, when applicable) was measured on a microbalance (Mettler Toledo MS204S) to serve as a calibration value. The substrate was then affixed to the same speaker from the first phase and placed on a tilt-table in a modified freezer, depicted in Fig. 2.7. A custom-built foam door with a shelf inlet was put in place to maintain the boundary of the freezer, and the freezer was turned on and set to the desired temperature ( $-20$  or  $-30\text{ }^{\circ}\text{C}$ ). The freezer was allowed time to reach the target temperature (2.5 and 3.5 hours, respectively) and then given another 2 hours to ensure that the substrate would have time to reach and stabilize at the temperature in addition to the local atmosphere. At this point,

the vibration was initiated, a channel in the shelf of the door was unplugged, and the motorized syringe was put in place above the channel. We released individual droplets of DI-water totaling 3 mL from the syringe through the channel and onto the substrate below. Upon completion of the evacuation, the speaker was disabled, the channel was plugged, and the substrate was left for 15 minutes to allow any liquid water to finish freezing. After this, we removed the substrate and measured its mass with the accreted ice on the microbalance, as well as leaving the freezer open and off in order to defrost it.

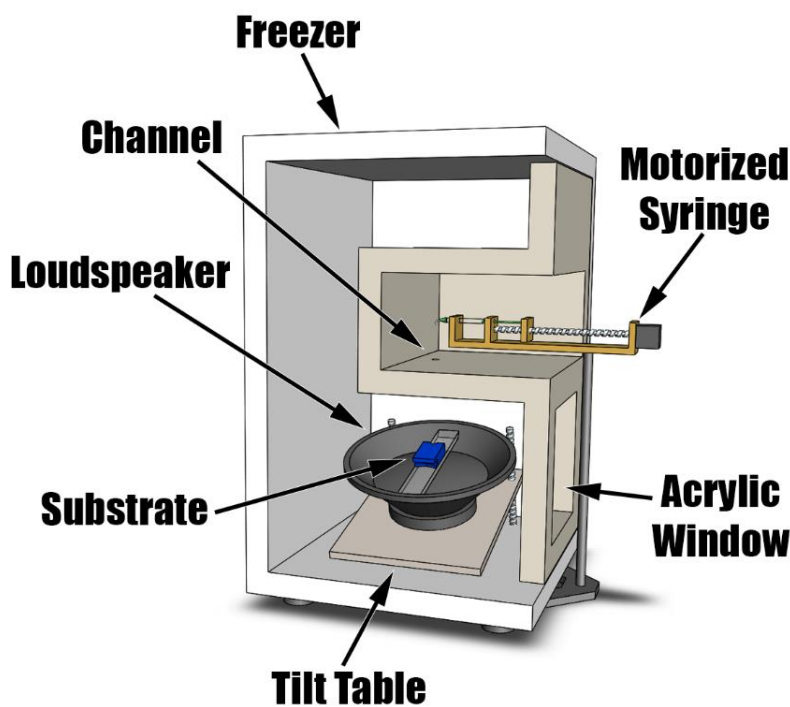


**Fig. 2.7.** Freezer phase experimental setup (cut-away view).

To facilitate the temperature conditions necessary, we started with a freezer (Summit VLT650) which could reach the desired temperatures. This freezer claimed a minimum temperature capability of  $-35\text{ }^{\circ}\text{C}$ , so our lowest temperature was chosen to be  $-30$  to ensure the equipment could consistently reach the target without difficulty. An additional temperature of  $-20\text{ }^{\circ}\text{C}$  was also tested to provide context for the results while still approximating atmospheric temperatures. Due

to calibration errors, we set the control of the freezer to -32 and -21 °C respectively in order to adjust for the offset determined with more accurate thermometers. The air temperature within the freezer was measured with the built in freezer thermometer (separate from the thermostat sensor) and an indoor/outdoor thermometer (Acu-Rite 00611A3), and the temperature of the substrate was measured using a contact-less infrared temperature sensor (Adafruit TMP006) attached to an Arduino Uno microcontroller and LCD (DIYmall 0.96" 128x64 pixel display).

The door of the freezer was removed and replaced with a custom-built alternative made of 50-mm thick low-thermal-conductivity polystyrene foam. The foam was cut to tightly fit the freezer opening, and additional cuts were made to insert a 150 x 150 mm polished acrylic window near the bottom and a shelf-like inlet in the middle. This shelf – approximately 180 mm wide, 85 mm tall, and 230 mm deep – was created to enable the motorized syringe system to be in a room-temperature environment and thus prevent freezing of the syringe while allowing ejected droplets to still fall onto the substrate. It was designed to fit between the shelves in the freezer, which also served as radiators for the coolant system, and still allow the motorized syringe to fit deeply enough to reach the area above the substrate (Fig. 2.8). All sides of the shelf were fabricated from the same polystyrene foam, using duct tape (Gorilla 6035180) to both affix the walls together and to seal the gaps from air flow. At the appropriate location above the substrate, a 20 mm hole was drilled in the bottom wall of the foam shelf to act as the channel through which the droplets could reach the substrate. A spare piece of the foam was cut into a wedge shape to act as a plug for the channel when not in use (Fig. 2.9), so that the freezer remained as isolated as possible.

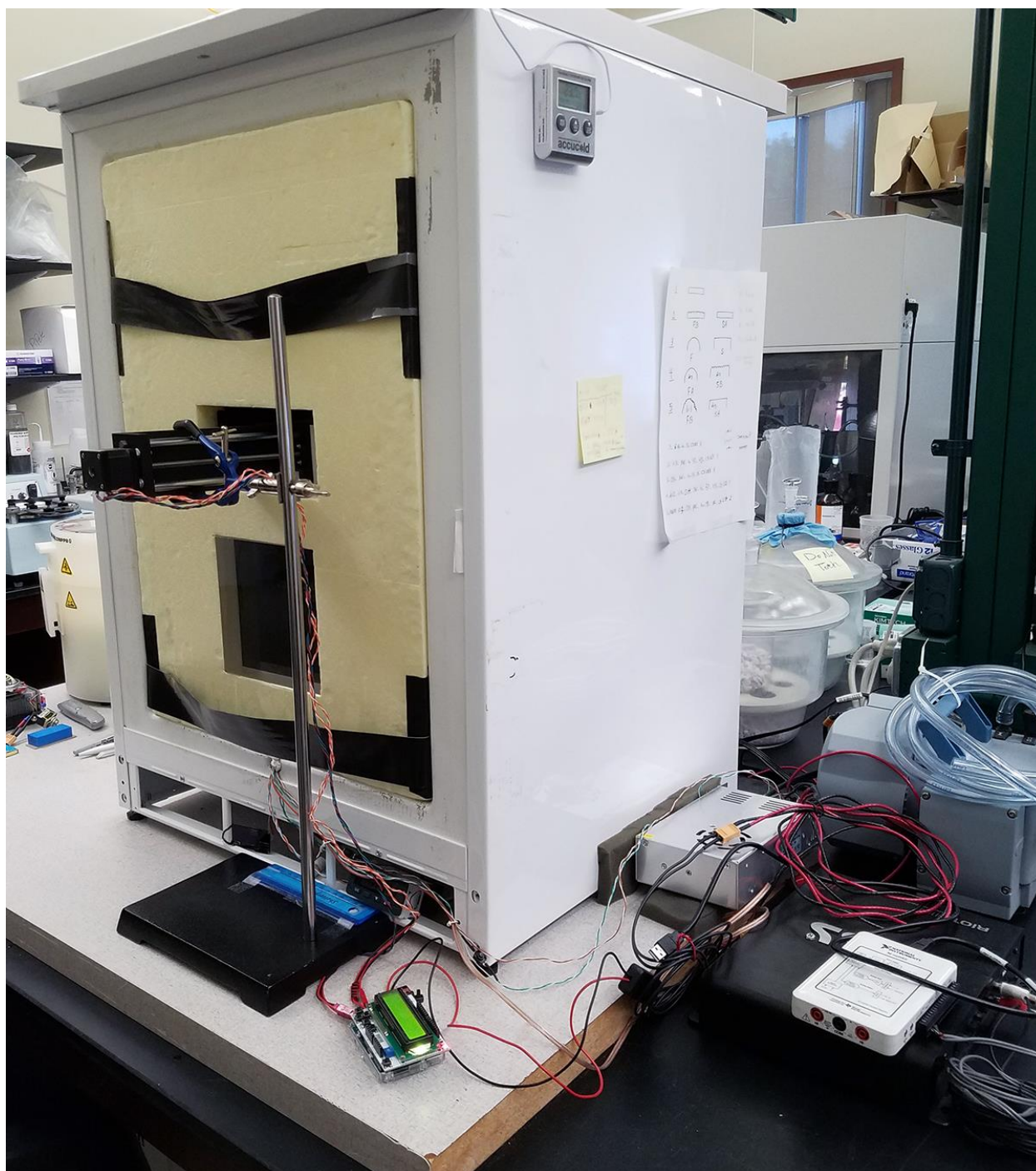


**Fig. 2.8.** The freezer is shown with the door and syringe in place, and the power supply, function generator, and amplifier are shown in the bottom right of the photo.



**Fig. 2.9.** Freezer door shelf with channel and plug.

The speaker, amplifier, and function generator were connected just as in the previous phase of the experiment. However, in this case the amplitude of the function generator was selected to normalize the power being input to the speaker for both frequencies. Now that the initial impact of the droplet is less of a focus, consistent vibration displacements are not necessary, and so total energy added to the system becomes the more critical factor to maintain. Normalizing the power would isolate the effect of frequency from changes in energy to the system. A practical range of amplitudes were tested for both frequencies, measuring the current flowing from the amplifier to the speaker using a multimeter and calculating power using  $P = VI$ , in which  $P$  is the input power to the speaker,  $V$  is the voltage selected at the function generator, and  $I$  is the measured current. Given the limited resolution of the output voltage, selecting a possible power level that occurred in both ranges resulted in a value around 0.0280 W. For a 20 Hz sine wave, this required an amplitude set to 0.15 V, and for a 220 Hz wave, 0.20 V.



Measuring ice accretion is an issue that is time-sensitive for two primary reasons. First, given time in a room-temperature environment inherently leads to melting of the ice, which risks the high mobility of liquid water causing it to roll off the substrate during transportation, altering the measurement. On the other hand, the substrate at such cool temperatures will immediately start forming frost from the condensation of the humid room-temperature air as soon as they come in contact. The mass of frost that would accrete was on the order of 0.1% of the mass of ice from the experiment every few seconds. Thus, this was not a drastic threat to the integrity of the results, but nonetheless required expedient removal of the substrate and transportation to the microbalance for measurement. As such, a model (shown in Fig. 2.10) was created and 3D printed in PLA which could be secured to the acrylic bridge with only two bolts, and could therefore be quickly freed with the removal of only one bolt. The design was printed with 100% infill to ensure a solid material. After printing, the substrate was polished smooth using 600 and then 1200 grit sandpaper (Allied High Tech Products Inc.), cleaned with a detergent, and sonicated in a water-ethanol solution.

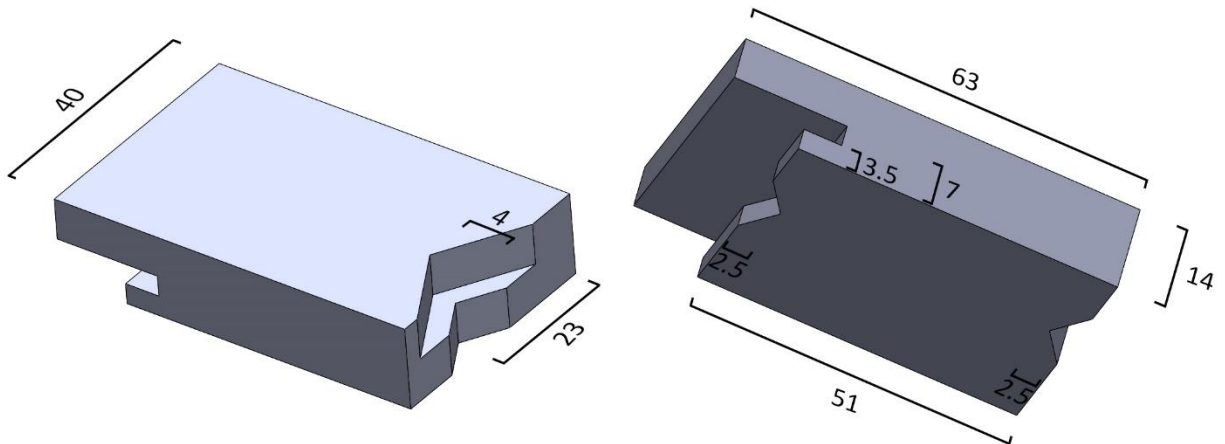


**Fig. 2.10.** Model of the 3D-printed substrate. The flat-head style bolts will rest in the V-shaped notches, with the cantilever preventing water from potentially freezing the substrate to the acrylic bridge.



Some of the substrates printed were used bare, and some were coated with soot and functionalized as in the process explained earlier, resulting in some hydrophilic substrates and some superhydrophobic substrates. In order to preempt deterioration, a coated substrate was used for the entirety of the  $-30^{\circ}$  testing, and then a replacement was used for the  $-20^{\circ}$  testing. Again, the samples showed no visible degradation at the end of their use.

The tilt table used consisted of a 10" strap hinge bolted to the floor of the freezer with rubber tubing cut to length to raise the table approximately 3" off the base of the freezer in order to reach a height that would allow the setup to fit within the freezer. A 6" threaded rod was secured with standard stainless steel nuts to two 4" strap hinges, one bolted to each strap of the larger hinge. This provided control over the angle of the main hinge, which we set to approximately 5 degrees from horizontal using a level (Digi-Pas DWL-80E).

The motorized syringe system was adjusted on the laboratory ring stand to the height that would measure 85 mm above the surface of the substrate. A 10 mL syringe was installed for this phase, giving an accuracy of 0.0556  $\mu\text{L}/\text{step}$ , and fitted with a 20-gauge needle, resulting in droplets around 20  $\mu\text{L}$ . For this phase, we released 3 mL of water at a rate of 27.8  $\mu\text{L}/\text{second}$  (the motor set to 500 steps/second).

## Chapter 3 Results and Discussion

### 3.1. Room Temperature

The droplet impacts at room temperature showed an average decrease in total contact time as frequency increased, depicted in Fig. 3.1. This graph was formulated by plotting the arithmetic mean of the contact times for the 20 repeat trials at each frequency for a given droplet size. The contact time was obtained by reviewing the high-speed video of the event and counting the number of frames of video from when the droplet first makes contact with the substrate to the first moment that the droplet is no longer in contact with the surface at all. Dividing the number of frames by the recording frame rate (5000 fps), we get the duration of contact in seconds.

The rate of the linear line-of-best-fit tended very closely to -1 ms/100 Hz, supported by an  $R^2$  value of 0.8253, indicating a strong likelihood of this correlation. However, the variance increased drastically at all but the lowest frequencies (depicted in Fig 3.1). In some cases, the spread of data at a particular frequency was approximately 60% of the mean at that frequency.

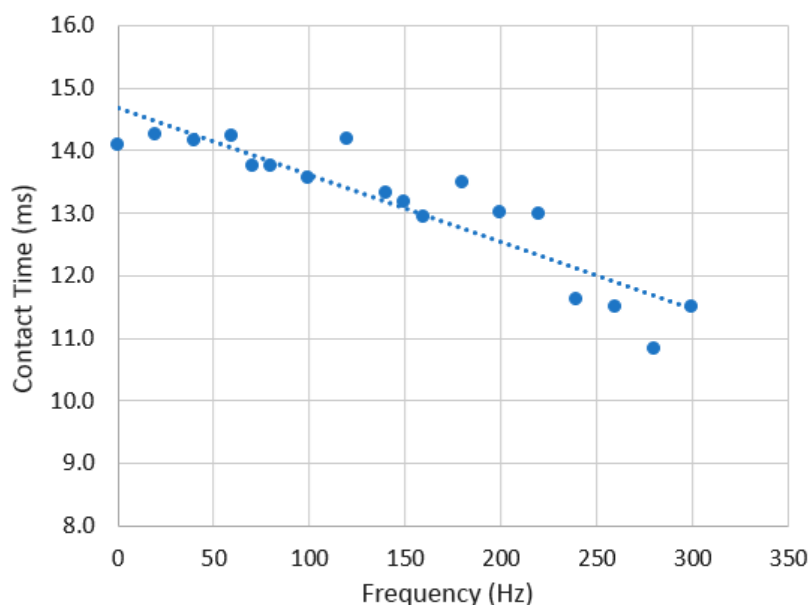


**Fig. 3.1.** The contact time of a 10  $\mu$ L droplet as a function of frequency given constant wave amplitude. The dashed line represents the line of best fit, showing a strong negative correlation ( $R^2 = 0.8253$ ).

The total contact time  $\tau$  of an impact is the sum of the spreading time  $\tau_s$  and the retracting time  $\tau_r$ . At the beginning of impact, the kinetic energy of the droplet is redirected outward, spreading the droplet along the solid surface. At the peak width of the droplet during this contact, the surface tension is overcoming the inertial energy, changing the direction of motion to a horizontal contraction. By finding this maximum width, the spreading contact time can be measured by the quantity of video frames from initial contact to this inflection point. Likewise, the retracting contact time can be measured by the quantity of frames from the inflection point to the first point of no-contact. Figure 3.2 shows the collection of values for total contact time, retracting contact time, and spreading contact time of a 10  $\mu\text{L}$  droplet for each frequency.

As demonstrated by Abolghasemibizaki *et al.*, though the contact time has already been shown to be a function of droplet density  $\rho$ , radius  $R$ , and surface tension  $\gamma$  as  $\tau \propto \sqrt{\rho R^3 / \gamma}$ , manipulating the equations reveals that the retracting time similarly scales with the same three factors [30]. This indicates that the spreading time should remain constant with a given droplet size regardless of the impact velocity, and so the changes in contact time are propagated in the retraction phase [31]. This tended to hold true in our experiments as displayed in Fig. 3.2, with changes in the retracting phase driving the overall contact time variation, designated by the large spread in the retracting phase and the matching patterns in the total contact time data. For a vibrating surface, one might argue that the motion of the surface relative to the falling droplet causes variation in the relative impact velocity. This model dictates that the spreading time should be unaffected, however, indicating that there is another issue at play that is causing this variance.

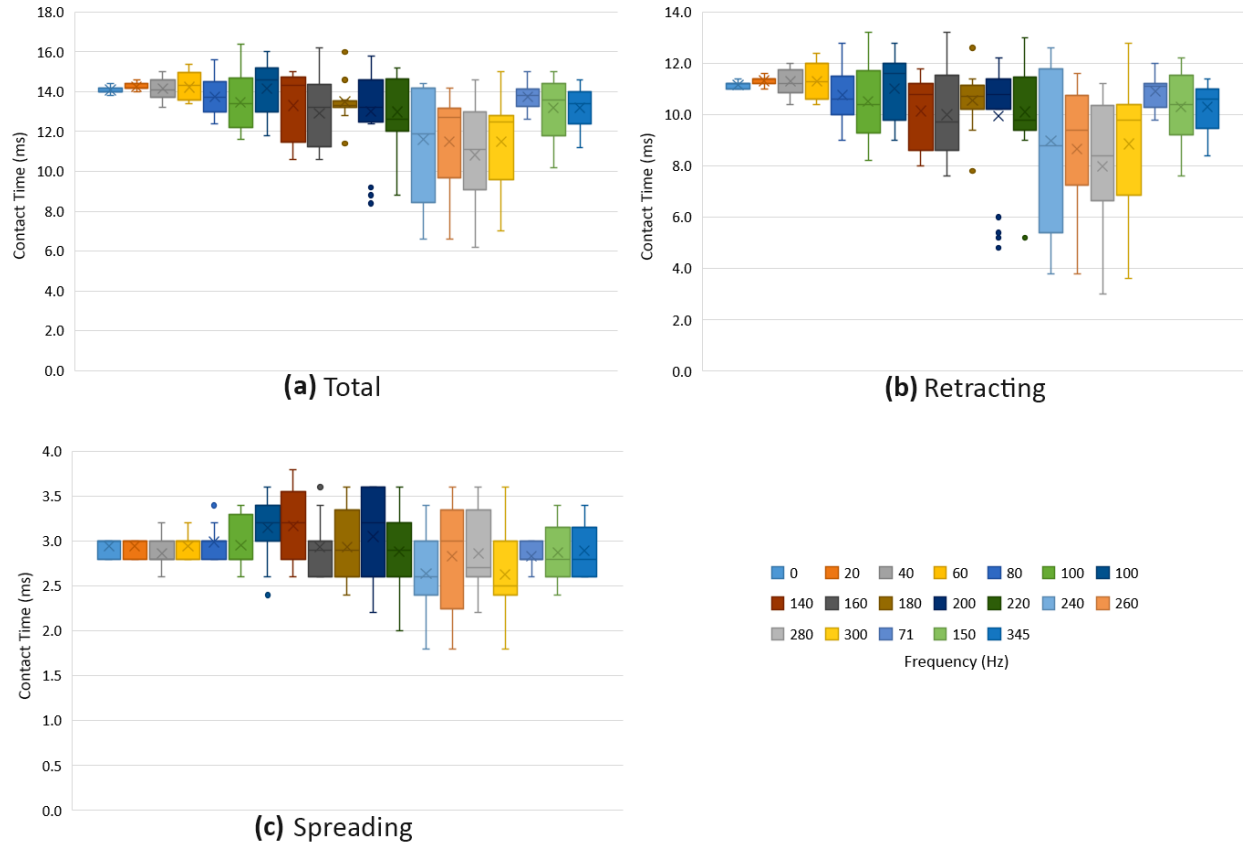


**Fig. 3.2.** The contact times of 10  $\mu\text{L}$  droplets as a function of frequency. (a) The total contact time. (b) The duration of the retracting phase of the impact. (c) The duration of the spreading phase. The effect of the vibration is more pronounced in the spreading phase, though the variance impedes practical assessment.

The trend of the mean contact time, however, seems only applicable with the 10  $\mu\text{L}$  droplets. At 20  $\mu\text{L}$ , the mean contact times varied as frequencies increased (Fig. 3.3a). There was still a tendency toward lower contact times as frequency increased, but this was not as clear as with the 10  $\mu\text{L}$  droplets because the data also seemed to show an oscillation, though more data would be required in order to confirm or refute this. Regardless, it clearly did not follow a simply linear trend like with 10  $\mu\text{L}$  droplets. With 30  $\mu\text{L}$  droplets (Fig. 3.3b), the potential oscillation was less pronounced while the linear correlation was slightly enhanced compared to the data from the 20  $\mu\text{L}$  droplet. Again, this cannot be confirmed so far with the data available, but it is a possible topic for future research.

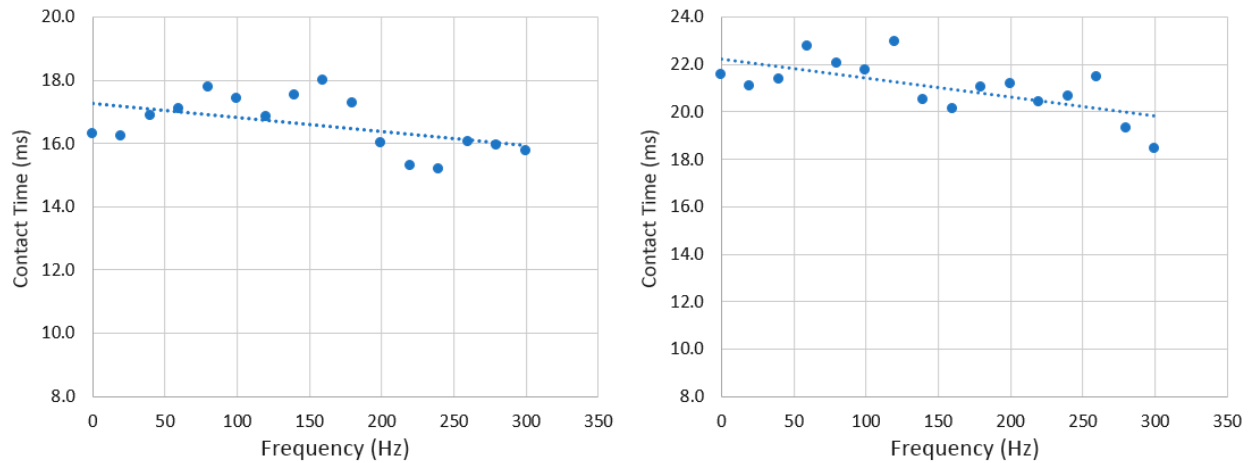


**Fig. 3.3.** The contact times of (a) 20  $\mu\text{L}$  droplets and (b) 30  $\mu\text{L}$  droplets as a function of frequency, with linear trend lines. Polynomial trend lines were a closer fit, though the data was too limited to properly extrapolate their accuracies.

The lower correlation in the larger droplets could be related to splashing, given that the larger droplets would more often break apart, which would affect the total contact time. Though the sinusoidal implications of the plot could indicate a relationship with a resonant frequency of the droplet, which seems more likely given that even the 10  $\mu\text{L}$  droplet contact times showed a hint of oscillation.

This could very well support the main mechanism behind the decreasing mean contact time – early separation of the droplet from the surface due to resonant motion of the droplet. Initial assumptions might be to attribute the changes in contact time, including the variance in both positive and negative directions, to changes in the relative impact velocity of the droplet with the vibrating surface. Richard *et al.* showed that contact time unintuitively is independent of the impact velocity except for very small or large velocities, and instead scales with drop radius [11]. Precision of the motorized syringe contrasted with the scale of the variance further rejects such an attribution.

The contact time of a droplet impact consists of two segments – spreading and retracting. Impacting the surface induces an oscillation in which the droplet spreads laterally and compresses vertically, and then compresses laterally and spreads vertically. In a standard droplet impact, the initial impact creates a large, slow oscillation – one cycle of which is what causes the spreading, the retraction, and ultimately the ejection of the droplet from the surface as the vertical expansion is blocked by the substrate, redirecting the majority of the energy upward and away from the substrate. Vibration of the substrate introduces an additional oscillation in the same way, but these are much smaller and faster such that multiple cycles can occur in the time of one cycle of the larger oscillation. The peaks of the smaller oscillations similarly tend to push the droplet away from the surface, and a strong enough vibration can provide enough force for the droplet to fully detach from the surface. Because the standard in the field of droplet impacts is to consider the contact time ending point when the droplet has first completely detached from any contact with the substrate, even a very brief ejection due to the smaller oscillations can drastically shorten the contact time. The contact time, therefore, doesn't always correlate to the sum of the spreading time and retracting time caused by the larger oscillation, as it would on a static substrate. This phenomenon indicates that the mean contact time will remain near that expected of a static surface unless the input energy is high enough to increase the likelihood that the droplet will fully detach on an earlier cycle. This explains the high variance in the data as input energy increases while also explaining the decreasing mean contact time due to the occasional drastic reduction from a brief detachment.

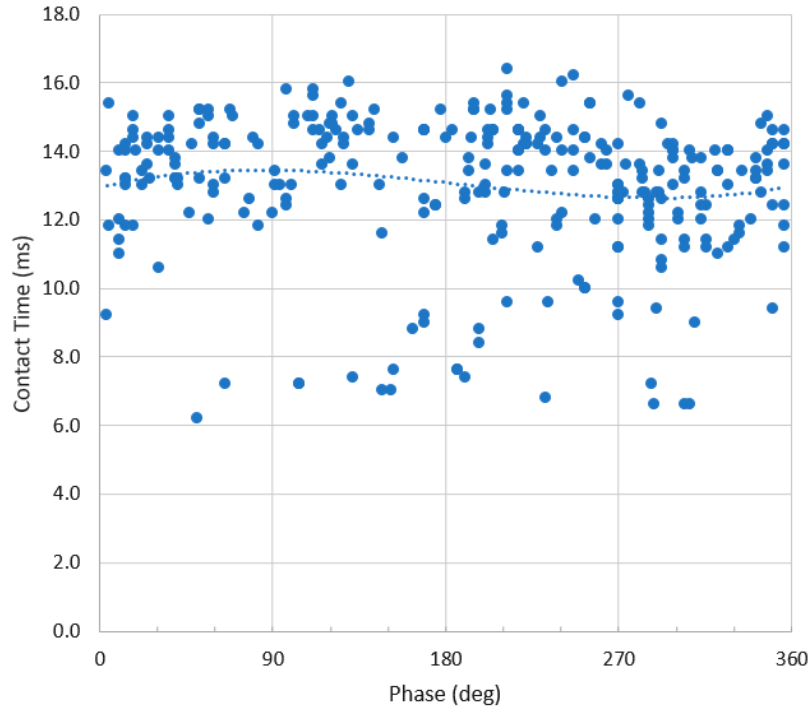


**Fig. 3.4.** The contact times of 10  $\mu\text{L}$  droplets as a function of impact phase. The dashed line represents the polynomial best fit, which correlates with the expected trend well, but correlates very poorly with the experimental data.

Another key parameter, the timing of the impact with relation to the position of the substrate in the sine wave, is known as the phase of the impact. Weisensee *et al.* had concluded that there was a critical phase which would provide the minimum contact time ( $316^\circ$ ), and as the phase deviated in either direction from this ideal, the contact time would increase given other parameters held constant [32]. The droplet impacts in our testing were analyzed for their approximate impact phase ( $\pm 10.8^\circ$  at 300 Hz) by denoting the frame at the peak of the wave when the substrate is highest and the frame at the trough of the wave when the substrate is at its lowest. By determining the ratio of frames between the peak and the initial contact compared to the quantity between then initial contact and the trough, the location along the wave can be determined. The data in Fig. 3.4 indicated that our results concurred with the expected critical phase, though the data varied so widely that the correlation was very weak.

### 3.2. Sub-zero Temperature

The freezing river tests showed similar results in many ways. Fig. 3.5 first shows that the vibration had negligible effect on the hydrophilic substrate at  $-30\text{ }^{\circ}\text{C}$ , where the droplets maintained enough contact to freeze prior to rolling off the edge. This resulted in a large mound of ice containing essentially all of the water ejected. The graph also shows that the coated (superhydrophobic) samples at  $-30\text{ }^{\circ}\text{C}$  retained less water than the uncoated (hydrophilic) samples did at  $-20\text{ }^{\circ}\text{C}$ , demonstrating the efficacy of the coating. All of the trials resulted in accreted ice due to the combination of very low temperatures provoking quicker freezing, a low tilt angle which doesn't encourage droplet acceleration, and imperfections in the surface (including unevenness in the coating or introduction of dirt particles from the air). Though the hope is to develop a method for complete ice prevention, even just improvement over the currently understood limits would be welcome. While the vibrating samples did show changes in accumulated ice, the variance was too great relative to the average change for a reliable trend to be perceived. Static substrates, on the other hand, still demonstrated very low variance.

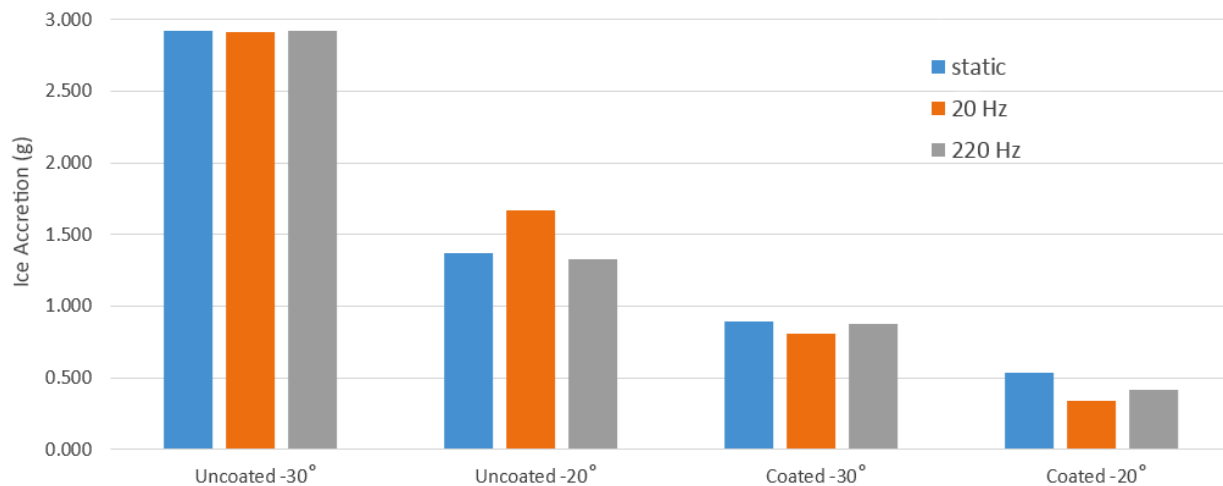


**Fig. 3.5.** The mass of ice accreted on uncoated hydrophilic substrates and coated superhydrophobic substrates, at both  $-20\text{ }^{\circ}\text{C}$  and  $-30\text{ }^{\circ}\text{C}$ . The variation shows that the coating and temperature had significant effects, while the impact of the vibration on the results was unclear.



The large variation in this case could not be explained, at least directly, by droplet oscillations due to impact. Instead, the water remained liquid long enough that it could pool at the bottom edge of the substrate in all cases except the uncoated  $-30^{\circ}$  runs. Isolated droplet fragments and residue would freeze nearly immediately off the main path of the droplets, where they could not be self-cleaned by the larger droplets, however even in the  $-30^{\circ}\text{C}$  trials the pool at the edge of the substrate would not have frozen by the end of ejection. In some cases, vibration would impart enough disturbance to cause the puddle to break free and drain off the edge, while other times the agitation was insufficient and the pool would remain and eventually freeze in place. This pooling occurred especially in the  $-20^{\circ}\text{C}$  trials, where the water would remain in liquid form longer. The pooling would occur multiple times in the course of a 3 mL ejection, and the size of the pool at the conclusion of ejection would determine the resulting mass of ice accreted. If a pool broke over the edge slightly sooner, the final pool might have had slightly more time to grow before the dripping ended, and if the pool took slightly longer, then the final pool might have been slightly smaller.

## Chapter 4 Conclusions

This study shows that, for a droplet with a low enough Weber number to prevent splashing, impacting a vibrating surface parallel to the direction of vibration on average tends to reduce the contact time compared to a similar impact on a static surface, given a constant vibration displacement. For a 10  $\mu\text{L}$  droplet, this decrease occurs at a rate of -1 ms/100 Hz. This is due to occasional premature detachment of droplets causing drastically reduced contact times and pulling the mean contact time down. The trend is also accompanied by occasional increases in contact time when the resonance of the droplet relative to the frequency of vibration delays the rebound mechanism which causes the full ejection of the droplet from the surface. The complex patterns of the resulting data can be attributed to the influences of many parameters beyond what was initially expected in this investigation.

In sub-zero conditions, the effect of substrate vibration on ice accretion was imperceptible when cloaked by much more impactful effects, notably the extreme water-repellency of a superhydrophobic coating even at uncommonly low temperature extremes. This further supports the notion of unforeseen factors that need to be accounted for before accurately estimating a model of the dynamics at play. Regardless, the investigation demonstrated the potential for means of passive reduction of icing, but also for drastically reduced contact times of droplet impacts.

## **Chapter 5 Future Recommendations**

An initial succession to this investigation might start by exploring methods to reduce the variation of the results. In the case of the room-temperature impacts, more precise equipment could solve this, by ensuring that droplets are all exactly the same volume, that the speaker is outputting an accurate and pure sine wave, and recording video with higher frame rate and resolution. The pooling in the freezer hosts the largest potential for improvement. Any method to mitigate this, potentially including changing the geometry of the substrate by rounding the edge, could yield much more accurate results as the all-or-nothing effect would be removed and replaced with a more continuous set of possible values.

A deeper investigation of droplet impacts in sub-zero temperatures could reveal a more reliable understanding of the dynamics at play. Further investigation could compare the room temperature droplet impacts to similar impacts in sub-zero temperatures given a suitably intricate experimental setup capable of overcoming the difficulty in dealing with supercooled water, and would more accurately mirror the real-world conditions that are the foundation of applications for this topic. Though such a study might be mechanically impractical, it would be elucidating to directly compare a room-temperature droplet impact to a supercooled droplet fully contained within a sub-zero environment.

## References

- [1] K.D. Esmeryan, C.E. Castano, M. Abolghasemibizaki, R. Mohammadi, An artful method for in-situ assessment of the anti-biofouling potential of various functional coatings using a quartz crystal microbalance, *Sensors Actuators, B Chem.* 243 (2017) 910–918. doi:10.1016/j.snb.2016.12.073.
- [2] Z. Wang, Y. Su, Q. Li, Y. Liu, Z. She, F. Chen, L. Li, X. Zhang, P. Zhang, Researching a highly anti-corrosion superhydrophobic film fabricated on AZ91D magnesium alloy and its anti-bacteria adhesion effect, *Mater. Charact.* 99 (2015) 200–209. doi:10.1016/j.matchar.2014.12.004.
- [3] E.P. Lozowski, K. Szilder, L. Makkonen, Computer simulation of marine ice accretion, *Philos. Trans. R. Soc. A Math. Phys. Eng. Sci.* 358 (2000) 2811–2845. doi:10.1098/rsta.2000.0687.
- [4] A.P. Orimolade, O.T. Gudmestad, L.E. Wold, Vessel stability in polar low situations, *Ships Offshore Struct.* 12 (2017) S82–S87. doi:10.1080/17445302.2016.1259954.
- [5] O. Parent, A. Ilinca, Anti-icing and de-icing techniques for wind turbines: Critical review, *Cold Reg. Sci. Technol.* 65 (2011) 88–96. doi:10.1016/j.coldregions.2010.01.005.
- [6] L. Makkonen, T. Laakso, M. Marjaniemi, K.J. Finstad, Modelling and prevention of ice accretion on wind turbines, *Wind Eng.* 25 (2001) 3–21. doi:10.1260/0309524011495791.
- [7] M.C. Homola, M.S. Virk, T. Wallenius, P.J. Nicklasson, P.A. Sundsbø, Effect of atmospheric temperature and droplet size variation on ice accretion of wind turbine blades, *J. Wind Eng. Ind. Aerodyn.* 98 (2010) 724–729. doi:10.1016/j.jweia.2010.06.007.
- [8] S. Ramanathan, V. V. Varadan, V.K. Varadan, Deicing of helicopter blades using piezoelectric actuators, *Smart Struct. Mater. 2000 - Smart Electron. MEMS*, March 6, 2000 - March 8, 2000. 3990 (2000) 281–292. doi:10.1117/12.388906.
- [9] J. Palacios, E. Smith, J. Rose, R. Royer, Instantaneous De-Icing of Freezer Ice via Ultrasonic Actuation, *AIAA J.* 49 (2011) 1158–1167. doi:10.2514/1.J050143.
- [10] M. Bragg, T. Hutchison, J. Merret, Effect of ice accretion on aircraft flight dynamics, in: 38th Aerosp. Sci. Meet. Exhib., American Institute of Aeronautics and Astronautics, 2000. doi:10.2514/6.2000-360.
- [11] D. Richard, C. Clanet, D. Quéré, Contact time of a bouncing drop, *Nature.* 417 (2002) 811. doi:10.1038/417811a.

- [12] J.C. Bird, R. Dhiman, H.-M. Kwon, K.K. Varanasi, Reducing the contact time of a bouncing drop., *Nature*. 503 (2013) 385–388. doi:10.1038/nature12740.
- [13] S. Zhang, X. Ouyang, J. Li, S. Gao, S. Han, L. Liu, H. Wei, Underwater drag-reducing effect of superhydrophobic submarine model, *Langmuir*. 31 (2015) 587–593. doi:10.1021/la504451k.
- [14] T. Bharathidasan, S.V. Kumar, M.S. Bobji, R.P.S. Chakradhar, B.J. Basu, Effect of wettability and surface roughness on ice-adhesion strength of hydrophilic, hydrophobic and superhydrophobic surfaces, *Appl. Surf. Sci.* 314 (2014) 241–250. doi:10.1016/j.apsusc.2014.06.101.
- [15] A. Marmur, The lotus effect: Superhydrophobicity and metastability, *Langmuir*. 20 (2004) 3517–3519. doi:10.1021/la036369u.
- [16] R. Furstner, W. Barthlott, C. Neinhuis, P. Walzel, Wetting and self-cleaning properties of artificial superhydrophobic surfaces, *Langmuir*. 21 (2005) 956–961. doi:10.1021/la0401011.
- [17] M. Abolghasemibizaki, C.J. Robertson, C.P. Fergusson, R.L. McMasters, R. Mohammadi, Rolling viscous drops on a non-wettable surface containing both micro- and macro-scale roughness, *Phys. Fluids*. 30 (2018). doi:10.1063/1.5016824.
- [18] L. Cao, A.K. Jones, V.K. Sikka, J. Wu, D. Gao, Anti-Icing superhydrophobic coatings, *Langmuir*. 25 (2009) 12444–12448. doi:10.1021/la902882b.
- [19] N.J. Shirtcliffe, G. McHale, S. Atherton, M.I. Newton, An introduction to superhydrophobicity, *Adv. Colloid Interface Sci.* 161 (2010) 124–138. doi:10.1016/j.cis.2009.11.001.
- [20] M. Abolghasemibizaki, R. Mohammadi, Droplet impact on superhydrophobic surfaces fully decorated with cylindrical macrottextures, *J. Colloid Interface Sci.* 509 (2018) 422–431. doi:10.1016/j.jcis.2017.09.030.
- [21] J. Bico, U. Thiele, D. Quéré, Wetting of textured surfaces, *Colloids Surfaces A Physicochem. Eng. Asp.* 206 (2002) 41–46. doi:10.1016/S0927-7757(02)00061-4.
- [22] E. Bormashenko, R. Pogreb, G. Whyman, M. Erlich, Resonance Cassie-Wenzel wetting transition for horizontally vibrated drops deposited on a rough surface, *Langmuir*. 23 (2007) 12217–12221. doi:10.1021/la7016374.

- [23] C. Tan, Z. Jia, H. Yang, Z. Zhang, Dynamic behavior of a vibrated droplet on a low-temperature micropillared surface, *Appl. Surf. Sci.* 394 (2017) 358–363. doi:10.1016/j.apsusc.2016.10.060.
- [24] K.D. Esmeryan, C.E. Castano, A.H. Bressler, M. Abolghasemibizaki, R. Mohammadi, Rapid synthesis of inherently robust and stable superhydrophobic carbon soot coatings, *Appl. Surf. Sci.* 369 (2016) 341–347. doi:10.1016/j.apsusc.2016.02.089.
- [25] K.D. Esmeryan, C.E. Castano, A.H. Bressler, M. Abolghasemibizaki, C.P. Fergusson, A. Roberts, R. Mohammadi, Kinetically driven graphite-like to diamond-like carbon transformation in low temperature laminar diffusion flames, *Diam. Relat. Mater.* 75 (2017) 58–68. doi:10.1016/j.diamond.2017.01.014.
- [26] K.D. Esmeryan, E.I. Radeva, I.D. Avramov, Durable superhydrophobic carbon soot coatings for sensor applications, *J. Phys. D: Appl. Phys.* 49 (2016) 25309. doi:10.1088/0022-3727/49/2/025309.
- [27] K.D. Esmeryan, A.H. Bressler, C.E. Castano, C.P. Fergusson, R. Mohammadi, Rational strategy for the atmospheric icing prevention based on chemically functionalized carbon soot coatings, *Appl. Surf. Sci.* 390 (2016) 452–460. doi:10.1016/j.apsusc.2016.08.101.
- [28] Y. Hu, S. Rodier, K.M. Xu, W. Sun, J. Huang, B. Lin, P. Zhai, D. Josset, Occurrence, liquid water content, and fraction of supercooled water clouds from combined CALIOP/IIR/MODIS measurements, *J. Geophys. Res. Atmos.* 115 (2010) 1–13. doi:10.1029/2009JD012384.
- [29] R.M. Rauber, A. Tokay, An Explanation for the Existence of Supercooled Water at the Top of Cold Clouds, *J. Atmos. Sci.* 48 (1991) 1005–1023. doi:10.1175/1520-0469(1991)048<1005:AEFTEO>2.0.CO;2.
- [30] M. Abolghasemibizaki, R.L. McMasters, R. Mohammadi, Towards the shortest possible contact time: Droplet impact on cylindrical superhydrophobic surfaces structured with macro-scale features, *J. Colloid Interface Sci.* 521 (2018) 17–23. doi:10.1016/j.jcis.2018.03.005.
- [31] M. Abolghasemibizaki, Liquid Interaction with Non-wettable Surfaces Structured with Macroscopic Ridges, (2018).
- [32] P.B. Weisensee, J. Ma, Y.H. Shin, J. Tian, Y. Chang, W.P. King, N. Miljkovic, Droplet impact on vibrating superhydrophobic surfaces, *Phys. Rev. Fluids.* 2 (2017) 1–14. doi:10.1103/PhysRevFluids.2.103601.

## Appendix A Microcontroller Code

```
#include <EEPROM.h>
#include <LiquidCrystal.h>
LiquidCrystal lcd(8, 9, 4, 5, 6, 7);

//===== ** EXTRA LCD CHARACTERS ** =====

byte upArrow[8] = {
    B11111,
    B11011,
    B10001,
    B01010,
    B11011,
    B11011,
    B11111,
    B11111,
};

byte downArrow[8] = {
    B11111,
    B11111,
    B11011,
    B11011,
    B01010,
    B10001,
    B11011,
    B11111,
};

byte filledRightArrow[8] = {
    B11111,
    B11011,
    B11101,
    B00000,
    B11101,
    B11011,
    B11111,
    B11111,
};

byte filledLeftArrow[8] = {
    B11111,
    B11011,
    B10111,
    B00000,
    B10111,
    B11011,
    B11111,
    B11111,
};

byte quarterBlock[8] = {
    B00000,
```

```

    B00000,
    B00000,
    B00000,
    B00000,
    B00000,
    B11111,
    B11111,
};

byte halfBlock[8] = {
    B00000,
    B00000,
    B00000,
    B00000,
    B11111,
    B11111,
    B11111,
    B11111,
};

byte threeQuarterBlock[8] = {
    B00000,
    B00000,
    B11111,
    B11111,
    B11111,
    B11111,
    B11111,
    B11111,
};

//===== ** VARIABLES **

//===== ** USER DEFINED **

int maximumHalls = 700;
// Safe stopping position (higher is closer)

//      10 ml:   ???

// (LL) 10 ml:  695 (700 works)

//      1 ml:    700

//      0.3 ml:  565?

//===== ** PIN DEFINITIONS **

const int buttonSet = A0;
// Pin for the LCD panel button array

const int limitSwitchPinM = A1;
// Pins for the hall sensors (motor side, syringe side)

```



```

const int hallSensorPinS = A3;

#define stepPin 2
// Pins for the stepper motor driver
#define directionPin 3
#define MS1 A2
// Enable/disable microstepping
#define MS2 11
//
#define MS3 12
//
#define enablePin 13

//===== ** STATES **

int buttonState = 1024;
// Default value for untouched button array is 1024

bool buttonSelect = LOW;
// Current state of each button
bool buttonLeft = LOW;
bool buttonDown = LOW;
bool buttonUp = LOW;
bool buttonRight = LOW;

bool lastButtonSelect = LOW;
// For detecting state changes of buttons
bool lastButtonLeft = LOW;
bool lastButtonDown = LOW;
bool lastButtonUp = LOW;
bool lastButtonRight = LOW;

bool cursorOn = false;
// Toggle variable for cursor display

//===== ** MENU **

int activeMenu = 1;
// Selected position in the menu array
// 0:Volume
// 1:Rotation
// 2:Direction
// 3:Speed
// 4:Calibrate
// 5:Sensors
// 6:SetMin (unused)
int menuLength = 6;
// Length of menu array, used for looping through the menu options
bool subMenu = false;
// Whether the LCD is on the main menu or a submenu
int volMultiplier = 1;
// multiplier for cursor position
int rotMultiplier = 1;
// multiplier for cursor position

```

```

float volIncrement = 0.01;
// Amount to increase/decrease volume (to be ejected/filled) with each button
press
long rotIncrement = 1;
// Amount to increase/decrease rotations (to be ejected/filled) with each
button press

//===== ** SETTINGS **

bool syrDirection = HIGH;
// HIGH - eject fluid; LOW - intake fluid
float syrVolume = 10.00;
// uL of fluid to eject or intake at main menu
long syrRotations = 54000;
// Number of rotations to eject or intake at main menu
float syrSpeed = 50;
// rate of fluid ejection or intake

int addr0 = 0;
// Addresses in EEPROM that stores [calibrationValue]
int addr1 = 1;
unsigned int calibrationValue = 6400;
// uL of fluid ejected per revolution

int addrSENS = 3;
// Address in the EEPROM that stores the sensor override

//===== ** MOTOR **

bool limitSwitchM = false;
// Limit switch (against the motor mount) un-pressed
int hallMaxTravels = maximumHalls;
// Hall sensor reading at maximum travel (against the syringe mount)

int revsToMax = 400;
// Max rotations before overextending plunger
int revsToMin = 0;
// Min rotations before hitting syringe mount
bool travelError = false;
// State of error

//===== ** TIMERS **

const unsigned long debounce = 300;
// ms of debounce for activating the buttons
unsigned long lastDebounceTime = 0;
bool longDebounce = false;
// Enable longer debounce limit
bool shortDebounce = false;
// Enable shorter debounce limit

```

```

const unsigned long cursorRate = 500;
// ms between cursor blink state changes
unsigned long lastCursor = 0;
// Time of last cursor blink state change

//===== ** SETUP **

void setup() {

    lcd.createChar(0, upArrow);
    // Initialize custom characters for the LCD
    lcd.createChar(1, downArrow);
    lcd.createChar(2, filledRightArrow);
    lcd.createChar(3, filledLeftArrow);
    // lcd.createChar(4, quarterBlock);
    // lcd.createChar(5, halfBlock);
    // lcd.createChar(6, threeQuarterBlock);

    lcd.begin(16, 2);
    // Initialize the display as 16x2 characters
    lcd.setCursor(0,0);

    // Serial.begin(115200);

    pinMode(buttonSet, INPUT);
    // Pin for LCD button array

    pinMode(stepPin, OUTPUT);
    // Pins for motor driver
    pinMode(directionPin, OUTPUT);
    pinMode(MS1, OUTPUT);
    pinMode(MS2, OUTPUT);
    pinMode(MS3, OUTPUT);
    pinMode(enablePin, OUTPUT);

    pinMode(limitSwitchPinM, INPUT);
    pinMode(hallSensorPinS, INPUT);

    resetStepperPins();
    // Set step, direction, microstep and enable pins to default states

    animationRestart();

    byte eep0 = EEPROM.read(addr0);
    byte eep1 = EEPROM.read(addr1);
    calibrationValue = multiplicationCombine(eep0, eep1);
    // Serial.print("Calibration: ");
    // Serial.println(calibrationValue);

    bool sensorOverride = EEPROM.read(addrSENS);
    // TRUE - permanently ignore hall sensors, FALSE - stop motor at overtravel

```

```

    if (sensorOverride == true) {
        lcd.clear();
        hallMaxTravelS = 2000;
    // Hall sensor reading at maximum travel (against the syringe mount)
        lcd.clear();
        lcd.setCursor(0,0);
    // Display intructions
        lcd.print("    WARNING:    ");
        lcd.setCursor(0,1);
        lcd.print("sensors disabled");
        delay(3000);
        lcd.clear();
    }

}

//===== ** MAIN LOOP **

void loop() {

    /*
    while (Serial.available() > 0) {
    // Read the serial monitor and test the motor with the values
        String incomingByte = Serial.readString();
        int blah = incomingByte.toInt();
        syrSpeed = blah;
        Serial.println(syrSpeed % 400);
    }
    */

    //===== ** POLLING **

    pollButtons();
    // Function to check the button array for presses

    //===== ** DISP - SIDE BUTTONS **

        lcd.setCursor(0,0);
        lcd.write(byte(3));
    // Left arrow
        lcd.setCursor(1,0);
        lcd.print((char)0xFF);
    // Filled box
        lcd.setCursor(2,0);
        lcd.print((char)0xFF);
    // Filled box
        lcd.setCursor(13,0);
        lcd.print((char)0xFF);
    // Filled box
        lcd.setCursor(14,0);
        lcd.print((char)0xFF);
    // Filled box
        lcd.setCursor(15,0);

```

```

    lcd.write(byte(2));
// Right arrow

    lcd.setCursor(3,0);
    lcd.print(" ");
    lcd.setCursor(12,0);
    lcd.print(" ");
    lcd.setCursor(3,1);
    lcd.print(" ");
    lcd.setCursor(12,1);
    lcd.print(" ");

//===== ** DISP - MAIN MENU **

    if (subMenu == false) {

        lcd.setCursor(4,0);
        switch (activeMenu) {
// Display the top center for the selected menu item
        case 0:
            if (syrDirection == HIGH)    {lcd.print(" EJECT  ");}
            else if (syrDirection == LOW) {lcd.print(" FILL  ");}
            break;
        case 1:
            if (syrDirection == HIGH)    {lcd.print(" EJECT  ");}
            else if (syrDirection == LOW) {lcd.print(" FILL  ");}
            break;
        case 2:
            lcd.print(" ");
            lcd.write(byte(0));
// Up arrow
            lcd.print("DIR:  ");
            break;
        case 3:
            lcd.print(" ");
            lcd.write(byte(0));
// Up arrow
            lcd.print("SPEED:");
            break;
        case 4:
            lcd.print(" CAL.VOL");
            break;
        case 5:
            if (hallMaxTravels == maximumHalls) {
                lcd.print(" DISABLE");
            }
            else {
                lcd.print(" ENABLE ");
            }
            break;
        case 6:
            lcd.print(" SET MIN");
            break;
        default:
            break;
    }

```

```

    }

    lcd.setCursor(0,1);
    lcd.print("PRV");
    lcd.setCursor(13,1);
    lcd.print("NXT");

    lcd.setCursor(4,1);
    switch (activeMenu) {
// Display the bottom center for the selected menu item
    case 0:
        lcd.print(" volume ");
        break;
    case 1:
        lcd.print(" rotat. ");
        break;
    case 2:
// Syringe direction (eject vs. fill)
        lcd.print(" ");
        lcd.write(byte(1));
// Down arrow
        if (syrDirection == HIGH) {lcd.print("eject  ");}
        else if (syrDirection == LOW) {lcd.print("fill  ");}
        break;
    case 3:
// Speed of fill/ejection
        lcd.print(" ");
        lcd.write(byte(1));
        if (syrSpeed < 1000) {lcd.print(" ");}
        if (syrSpeed < 100) {lcd.print(" ");}
        if (syrSpeed < 10) {lcd.print(" ");}
        if (syrSpeed < 1) {lcd.print(" ");}
        lcd.print(syrSpeed*10,0);
        lcd.print(" ");
        break;
    case 4:
        lcd.print("          ");
        break;
    case 5:
        lcd.print(" SENSORS");
        break;
    case 6:
        lcd.print("          ");
        break;
    default:
        break;
    }
}

//===== ** DISP - SUB-MENU **

    if (subMenu == true) {
// If sub-menu is active....

```

```

        switch (activeMenu) {
// Display the center information
        case 0:
            lcd.setCursor(4,0);
            lcd.print(" Volume:");
            if (buttonUp == HIGH && lastButtonUp == LOW) {
// Reset cursor timing on UP button press to make it clear that the cursor
has moved
                cursorOn = false;
                lastCursor = millis();
            }
            if (buttonDown == HIGH && lastButtonDown == LOW) {
// Reset cursor timing on DOWN button press to make it clear that the cursor
has moved
                cursorOn = false;
                lastCursor = millis();
            }
            if ((millis() - lastCursor) > cursorRate/2) {
// If it has been more than [cursorRate] ms since the cursor was last
toggled....
                if (cursorOn == true) {
// Toggle the cursor display....
                    lcd.setCursor(9-volMultiplier,1);
                    if (volMultiplier >= 3) {lcd.setCursor(9-volMultiplier-1,1);}
                    lcd.print(" ");
// By temporarily blanking out the selected digit
                }
                else {
// Otherwise, print leading zeroes and the current value of rotations (to be
executed)
                    lcd.setCursor(4,1);
                    if (syrVolume < 9.99) {lcd.print("0");}
                    lcd.print(syrVolume,2);
                    lcd.print(" ");
                    lcd.print((char)0xE4);
// "micro" symbol
                    lcd.print("L");
                }
                cursorOn = !cursorOn;
// Toggle the state of the cursor
                lastCursor = millis();
// Reset the timer for the last cursor toggle
            }
            break;
        case 1:
            lcd.setCursor(4,0);
            lcd.print(" Steps: ");
            if (buttonUp == HIGH && lastButtonUp == LOW) {
// Reset cursor timing on UP button press to make it clear that the cursor
has moved
                cursorOn = false;
                lastCursor = millis();
            }
            if (buttonDown == HIGH && lastButtonDown == LOW) {
// Reset cursor timing on DOWN button press to make it clear that the cursor
has moved
                cursorOn = false;

```

```

        lastCursor = millis();
    }
    if ((millis() - lastCursor) > cursorRate/2) {
// If it has been more than [cursorRate] ms since the cursor was last
toggled....
        if (cursorOn == true) {
// Toggle the cursor display....
            lcd.setCursor(11-rotMultiplier,1);
            lcd.print(" ");
// By temporarily blanking out the selected digit
        }
        else {
// Otherwise, print leading zeroes and the current value of rotations (to be
executed)
            lcd.setCursor(4,1);
            lcd.print(" ");
            if (syrRotations < 100000.0) {lcd.print("0");}
            if (syrRotations < 10000.0) {lcd.print("0");}
            if (syrRotations < 1000.0) {lcd.print("0");}
            if (syrRotations < 100.0) {lcd.print("0");}
            if (syrRotations < 10.0) {lcd.print("0");}
            lcd.print(syrRotations);
        }
        cursorOn = !cursorOn;
// Toggle the state of the cursor
        lastCursor = millis();
// Reset the timer for the last cursor toggle
    }
    break;
case 2:
    // VOID
    break;
case 3:
    lcd.setCursor(1,1);
    lcd.print((char)0x7F);
// "/" symbol

    lcd.setCursor(7,1);
    lcd.print(syrSpeed);
    lcd.setCursor(11,1);
    lcd.print(" m/s      ");
    break;
case 4:
    // VOID
    break;
case 5:
    // VOID
    break;
case 6:
    // VOID
    break;
default:
    break;
}

lcd.setCursor(0,1);

```



```

        switch (activeMenu) {
// Display the action for the LEFT button
        case 0:
            lcd.print("DGT");
            break;
        case 1:
            lcd.print("DGT");
            break;
        case 2:
            // VOID
            break;
        case 3:
            lcd.setCursor(1,1);
//            lcd.print((char)0x7F);
// "/" symbol

            lcd.setCursor(7,1);
            lcd.print(syrSpeed);
            lcd.setCursor(11,1);
            lcd.print(" m/s      ");
            break;
        case 4:
            // VOID
            break;
        case 5:
            // VOID
            break;
        case 6:
            // VOID
            break;
        default:
            break;
        }

        lcd.setCursor(13,1);
        switch (activeMenu) {
// Display the action for the RIGHT button
        case 0:
            if (syrDirection == HIGH) {lcd.print("EJC");}
            else if (syrDirection == LOW) {lcd.print("FIL");}
            break;
        case 1:
            if (syrDirection == HIGH) {lcd.print("EJC");}
            else if (syrDirection == LOW) {lcd.print("FIL");}
            break;
        case 2:
            // VOID
            break;
        case 3:
            lcd.setCursor(14,1);
            lcd.print((char)0x7E);
            break;
        case 4:
            // VOID
            break;
        case 5:

```

```

        // VOID
        break;
    case 6:
        // VOID
        break;
    default:
        break;
    }
}

//===== ** BUTTON ACTIONS - MAIN MENU **

if (subMenu == false) {

    if (buttonRight == HIGH && lastButtonRight == LOW) {
        activeMenu++; // Left/Right buttons change active
menu
        if (activeMenu == 0) {activeMenu = 1;}
        if (activeMenu == 4) {activeMenu = 5;}
    }
    if (activeMenu > menuLength-1) {
        activeMenu = 1;
// Menu loops after the last menu item
        shortDebounce = false;
// Return debounce limit to normal
    }

    if (buttonLeft == HIGH && lastButtonLeft == LOW) {
        activeMenu--;
        if (activeMenu == 4) {activeMenu = 3;}
    }
    if (activeMenu < 1) {
        activeMenu = menuLength-1;
// Menu loops before the first menu item
        shortDebounce = false;
// Return debounce limit to normal
    }

    if (buttonUp == HIGH && lastButtonUp == LOW) {
// UP button actions
        switch (activeMenu) {
            case 0:
                break;
            case 1:
                break;
            case 2:
                syrDirection = !syrDirection;
                break;
            case 3:
                shortDebounce = true;
                if (syrSpeed < 1) {syrSpeed = syrSpeed + 0.1;}
                else if (syrSpeed >= 1 && syrSpeed < 10) {syrSpeed = syrSpeed + 1;}

```

```

        else if (syrSpeed >= 10 && syrSpeed < 100) {syrSpeed = syrSpeed +
10;}        // Increase speed of fill/eject by 10 units
        else if (syrSpeed >= 100 && syrSpeed < 1600) {syrSpeed = syrSpeed *
2;}        //
        else {syrSpeed = 1600;}
// Set max speed to 1600
        break;
        case 4:
        break;
        case 5:
        break;
        case 6:
        break;
        default:
        break;
    }
}

    if (buttonDown == HIGH && lastButtonDown == LOW) {
// DOWN button actions
        switch (activeMenu) {
            case 0:
            break;
            case 1:
            break;
            case 2:
            syrDirection = !syrDirection;
            break;
            case 3:
            shortDebounce = true;
            if (syrSpeed > 100) {syrSpeed = syrSpeed / 2;}
            else if (syrSpeed > 10 && syrSpeed <= 100) {syrSpeed = syrSpeed -
10;}
            else if (syrSpeed > 1 && syrSpeed <= 10) {syrSpeed = syrSpeed - 1;}
            else if (syrSpeed > 0.1 && syrSpeed <= 1) {syrSpeed = syrSpeed -
0.1;}
            else {syrSpeed = 0;}
// Set min speed to 0
            break;
            case 4:
            break;
            case 5:
            break;
            case 6:
            break;
            default:
            break;
        }
    }

    if (buttonSelect == HIGH && lastButtonSelect == LOW) {
// SELECT button actions
        switch (activeMenu) {
            case 0:
            subMenu = true;
            lcd.setCursor(4,1);
            if (syrVolume <= 9.99) {lcd.print("0");}

```

```

        lcd.print(syrVolume,2);
        lcd.print(" ");
        lcd.print((char)0xE4);
// "micro" symbol
        lcd.print("L");
        break;
    case 1:
        subMenu = true;
        lcd.setCursor(4,1);
        lcd.print(" ");
        if (syrRotations < 100000.0) {lcd.print("0");}
        if (syrRotations < 10000.0) {lcd.print("0");}
        if (syrRotations < 1000.0) {lcd.print("0");}
        if (syrRotations < 100.0) {lcd.print("0");}
        if (syrRotations < 10.0) {lcd.print("0");}
        lcd.print(syrRotations);
        break;
    case 2:
        break;
    case 3:
//        subMenu = true;
        break;
    case 4:
        calibrateVolumeFunction();
// This function is the clibration procedure for the syringe calculations
        break;
    case 5:
        lcd.clear();
        areYouSure();
        break;
    case 6:
//        revsToMin = currentPos;
        break;
    default:
        break;
    }
}

}

```

```

//===== ** BUTTON ACTIONS - SUB-MENU **

    else if (subMenu == true) {

        if (buttonRight == HIGH && lastButtonRight == LOW) {
// RIGHT button actions
            switch (activeMenu) {
                case 0:
                    if (syrSpeed > 0) {moveMotor(syrSpeed, syrVolume, true);}
                    break;
                case 1:
                    if (syrSpeed > 0) {moveMotor(syrSpeed, syrRotations, false);}
                    break;
                case 2:
                    break;
            }
        }
    }

```

```

        case 3:
            break;
        case 4:
            break;
        case 5:
            break;
        case 6:
            break;
        default:
            break;
    }
}

    if (buttonLeft == HIGH && lastButtonLeft == LOW) {
// LEFT button actions
    switch (activeMenu) {
        case 0:
            volMultiplier++;
            volMultiplier = constrain(volMultiplier, 1, 5);
            if (volMultiplier > 4) {
                volMultiplier = 1;
            }
            break;
        case 1:
            rotMultiplier++;
            rotMultiplier = constrain(rotMultiplier, 1, 7);
            if (rotMultiplier > 6) {
                rotMultiplier = 1;
            }
            break;
        case 2:
            // VOID
            break;
        case 3:
            subMenu = false;
            break;
        case 4:
            // VOID
            break;
        case 5:
            // VOID
            break;
        case 6:
            // VOID
            break;
        default:
            break;
    }
}

    if (buttonUp == HIGH && lastButtonUp == LOW) {
// UP button actions
    switch (activeMenu) {
        case 0:
            volIncrement = 0.01;
            for (int mult = 1; mult < volMultiplier; mult++) {
                volIncrement = volIncrement * 10;
            }
        case 1:
            rotIncrement = 0.01;
            for (int mult = 1; mult < rotMultiplier; mult++) {
                rotIncrement = rotIncrement * 10;
            }
        case 2:
            // VOID
            break;
        case 3:
            subMenu = true;
            break;
        case 4:
            // VOID
            break;
        case 5:
            // VOID
            break;
        case 6:
            // VOID
            break;
        default:
            break;
    }
}

```

```

        }
        syrVolume = syrVolume + volIncrement;
// Increment the number of steps to turn
        if (syrVolume > 99.99) {syrVolume = 99.99;}
// Do not exceed 99.99 uL
        lcd.setCursor(4,1);
        if (syrVolume <= 9.99) {lcd.print("0");}
        lcd.print(syrVolume,2);
        break;
    case 1:
        rotIncrement = 1;
        for (int mult = 1; mult < rotMultiplier; mult++) {
            rotIncrement = rotIncrement * 10;
        }
        syrRotations = syrRotations + rotIncrement;
// Increment the number of steps to turn
        if (syrRotations > 320000) {syrRotations = 320000;}
// Do not exceed 10 revolutions
        lcd.setCursor(4,1);
        lcd.print(" ");
        if (syrRotations < 100000.0) {lcd.print("0");}
        if (syrRotations < 10000.0) {lcd.print("0");}
        if (syrRotations < 1000.0) {lcd.print("0");}
        if (syrRotations < 100.0) {lcd.print("0");}
        if (syrRotations < 10.0) {lcd.print("0");}
        lcd.print(syrRotations);
        break;
    case 2:
        // VOID
        break;
    case 3:
        subMenu = false;
        break;
    case 4:
        // VOID
        break;
    case 5:
        // VOID
        break;
    case 6:
        // VOID
        break;
    default:
        break;
    }
}

if (buttonDown == HIGH && lastButtonDown == LOW) {
// DOWN button actions
    switch (activeMenu) {
        case 0:
            volIncrement = 0.01;
            for (int mult = 1; mult < volMultiplier; mult++) {
                volIncrement = volIncrement * 10;
            }
            syrVolume = syrVolume - volIncrement;
// Increment the number of steps to turn

```

```

        if (syrVolume <= 0.00) {syrVolume = 0.00;}
// Do not exceed 0 uL
    lcd.setCursor(4,1);
    if (syrVolume <= 9.99) {lcd.print("0");}
    lcd.print(syrVolume,2);
    break;
case 1:
    rotIncrement = 1;
    for (int mult = 1; mult < rotMultiplier; mult++) {
        rotIncrement = rotIncrement * 10;
    }
    syrRotations = syrRotations - rotIncrement;
// Increment the number of steps to turn
    if (syrRotations <= 0) {syrRotations = 0;}
// Do not exceed 0 revolutions
    lcd.setCursor(4,1);
    lcd.print(" ");
    if (syrRotations < 100000.0) {lcd.print("0");}
    if (syrRotations < 10000.0) {lcd.print("0");}
    if (syrRotations < 1000.0) {lcd.print("0");}
    if (syrRotations < 100.0) {lcd.print("0");}
    if (syrRotations < 10.0) {lcd.print("0");}
    lcd.print(syrRotations);
    break;
case 2:
    // VOID
    break;
case 3:
    subMenu = false;
    break;
case 4:
    // VOID
    break;
case 5:
    // VOID
    break;
case 6:
    // VOID
    break;
default:
    break;
}
}

if (buttonSelect == HIGH && lastButtonSelect == LOW) {
// SELECT button actions
switch (activeMenu) {
case 0:
    subMenu = false;
    break;
case 1:
    subMenu = false;
    break;
case 2:
    // VOID
    break;
case 3:

```

```

        subMenu = false;
        break;
    case 4:
        // VOID
        break;
    case 5:
        // VOID
        break;
    case 6:
        // VOID
        break;
    default:
        break;
    }
}

}

//===== ** LAST BUTTON STATE **

    lastButtonState();
// Function to remember the last button state (for activation only on rising
edge)

}

//===== ** FUNCTIONS **

//===== ** RESET MOTOR **

void resetStepperPins()
{
    digitalWrite(stepPin, LOW);
    digitalWrite(directionPin, LOW);
    digitalWrite(MS1, LOW);
    digitalWrite(MS2, LOW);
    digitalWrite(MS3, LOW);
    digitalWrite(enablePin, HIGH);
}

//===== ** POLL BUTTONS **

void pollButtons() {
    buttonState = analogRead(buttonSet);
// Read button array value

    unsigned long debounceLimit;
    if (longDebounce == true) {debounceLimit = debounce*2;}
    else {debounceLimit = debounce;}
    if (shortDebounce == true) {debounceLimit = debounce/1;}
    else {debounceLimit = debounce;}

    // UNPRESSED BUTTONS

```



```

    if ((millis() - lastDebounceTime) > 50 && buttonState >= 1000) {
// Buttons are all connected via resistor network to pin A0
    buttonSelect = LOW;
// Set all the virtual buttons as "unpressed"
    buttonLeft   = LOW;
    buttonDown   = LOW;
    buttonUp     = LOW;
    buttonRight  = LOW;
    }

// PRESSED BUTTONS
if ((millis() - lastDebounceTime) > debounceLimit) {

    if (buttonState < 715) {
        buttonSelect = HIGH;
        buttonLeft   = LOW;
        buttonDown   = LOW;
        buttonUp     = LOW;
        buttonRight  = LOW;
        lastDebounceTime = millis();
    }

    else if (buttonState >= 715 && buttonState < 835) {
        buttonSelect = LOW;
        buttonLeft   = LOW;
        buttonDown   = LOW;
        buttonUp     = LOW;
        buttonRight  = HIGH;
        lastDebounceTime = millis();
    }

    else if (buttonState >= 835 && buttonState < 880) {
        buttonSelect = LOW;
        buttonLeft   = HIGH;
        buttonDown   = LOW;
        buttonUp     = LOW;
        buttonRight  = LOW;
        lastDebounceTime = millis();
    }

    else if (buttonState >= 880 && buttonState < 915) {
        buttonSelect = LOW;
        buttonLeft   = LOW;
        buttonDown   = HIGH;
        buttonUp     = LOW;
        buttonRight  = LOW;
        lastDebounceTime = millis();
    }

    else if (buttonState >= 915 && buttonState < 1000) {
        buttonSelect = LOW;
        buttonLeft   = LOW;
        buttonDown   = LOW;
        buttonUp     = HIGH;
        buttonRight  = LOW;
        lastDebounceTime = millis();
    }
}

```

```

    }

}

//===== ** LAST BUTTON STATE **

void lastButtonState() {

    if (buttonState < 715) {lastButtonSelect = HIGH;}

    else if (buttonState >= 715 && buttonState < 835) {lastButtonRight = HIGH;}

    else if (buttonState >= 835 && buttonState < 880) {lastButtonLeft = HIGH;}

    else if (buttonState >= 880 && buttonState < 915) {lastButtonDown = HIGH;}

    else if (buttonState >= 915 && buttonState < 1000) {lastButtonUp = HIGH;}

    else {
        lastButtonSelect = LOW;
        lastButtonLeft = LOW;
        lastButtonDown = LOW;
        lastButtonUp = LOW;
        lastButtonRight = LOW;
    }

    delay(1);

}

//===== ** MOVE MOTOR **

void moveMotor(float stepperSpeed, float distGoal, bool calculation) {

    unsigned long distTraveled = 0;
    unsigned long lastMoveTime = 0;

    // calculation: TRUE if distGoal is in uL, FALSE if distGoal is in
    rotations
    if (calculation == true) {
        distGoal = distGoal*calibrationValue/10;
    // Calibrate rotations needed for input distance
    }

    digitalWrite(enablePin, LOW);
    // Pull enable pin low to set FETs active and allow motor control
    stepperSpeed = constrain(stepperSpeed, 0, 1600);
    // Constrain the stepper speed so that delay between steps is long enough

    if (stepperSpeed <= 100) {

```

```

    digitalWrite(MS1, HIGH);
// Set microstep logic (1/16 step)
    digitalWrite(MS2, HIGH);
    digitalWrite(MS3, HIGH);
    stepperSpeed = 100000/stepperSpeed;
    distGoal = distGoal/1;
}

else if (stepperSpeed > 100 && stepperSpeed <= 200) {
    digitalWrite(MS1, HIGH);
// Set microstep logic (1/8 step)
    digitalWrite(MS2, HIGH);
    digitalWrite(MS3, LOW);
    stepperSpeed = map(stepperSpeed, 101, 200, 2000, 1000);
    distGoal = distGoal/2;
}
else if (stepperSpeed > 200 && stepperSpeed <= 400) {
    digitalWrite(MS1, LOW);
// Set microstep logic (1/4 step)
    digitalWrite(MS2, HIGH);
    digitalWrite(MS3, LOW);
    stepperSpeed = map(stepperSpeed, 201, 400, 2000, 1000);
    distGoal = distGoal/4;
}
else if (stepperSpeed > 400 && stepperSpeed <= 800) {
    digitalWrite(MS1, HIGH);
// Set microstep logic (1/2 step)
    digitalWrite(MS2, LOW);
    digitalWrite(MS3, LOW);
    stepperSpeed = map(stepperSpeed, 401, 800, 2000, 1000);
    distGoal = distGoal/8;
}

else if (stepperSpeed > 800) {
    digitalWrite(MS1, LOW);
// Set microstep logic (Full step)
    digitalWrite(MS2, LOW);
    digitalWrite(MS3, LOW);
    stepperSpeed = map(stepperSpeed, 801, 1600, 2000, 1000);
    distGoal = distGoal/16;
}

bool moveDirection = syrDirection;
if (activeMenu == 4) {
// Set direction to EJECT when calibrating syringe
    moveDirection = HIGH;
}
if (moveDirection == HIGH) {
// Set the direction for the stepper (HIGH - eject fluid; LOW - intake fluid)
    digitalWrite(directionPin, LOW);
}
else if (moveDirection == LOW) {
    digitalWrite(directionPin, HIGH);
}
}

```

```

    lcd.clear();
// Update the LCD
    lcd.setCursor(0,0);
    lcd.print("Moving...");

    unsigned long startTime = millis();
    while (distTraveled < abs(distGoal)) {
// Until the stepper reaches the desired distance....

        if (hallMaxTravels == 2000) {limitSwitchM = false;}
        else {limitSwitchM = digitalRead(limitSwitchPinM);}

        if ((micros() - lastMoveTime) > stepperSpeed) {
// Step the stepper every time it has been [stepperSpeed] microseconds

            if (moveDirection == LOW && limitSwitchM == false) {
                digitalWrite(stepPin, HIGH);
// Trigger one step
                digitalWrite(stepPin, LOW);
// Pull step pin low so it can be triggered again
                distTraveled++;
// Record the distance traveled
                lastMoveTime = micros();
// Mark the last step time
            }
            else if (moveDirection == HIGH && analogRead(hallSensorPinS) <=
hallMaxTravels) {
                digitalWrite(stepPin, HIGH);
// Trigger one step
                digitalWrite(stepPin, LOW);
// Pull step pin low so it can be triggered again
                distTraveled++;
// Record the distance traveled
                lastMoveTime = micros();
// Mark the last step time
            }
        }

        if (moveDirection == LOW && limitSwitchM == true) {
            lcd.clear();
            lcd.setCursor(0,0);
            lcd.print("Motor error:");
            lcd.setCursor(0,1);
            lcd.print("Max travel (M)");
            resetStepperPins();
            travelError = true;
            while (1) {
                lastButtonState();
                pollButtons();
            }
        }
    }
}

```

```

        if (buttonSelect == HIGH && lastButtonSelect == LOW) {break;}
// Only continue once SELECT has been pressed
    }
    break;
}
else if (moveDirection == HIGH && analogRead(hallSensorPinS) >
hallMaxTravels) {
    lcd.clear();
    lcd.setCursor(0,0);
    lcd.print("Motor error:");
    lcd.setCursor(0,1);
    lcd.print("Max travel (S)");
    resetStepperPins();
    travelError = true;
    while (1) {
        lastButtonState();
        pollButtons();
        if (buttonSelect == HIGH && lastButtonSelect == LOW) {break;}
// Only continue once SELECT has been pressed
    }
    break;
}

}

// Serial.print(millis() - startTime);
// Serial.println(" ms");

    lcd.clear();
    resetStepperPins();

}

//===== ** ARE YOU SURE??? **

void areYouSure() {

    bool sensCode1 = false;
    bool sensCode2 = false;
    bool sensCode3 = false;
    bool sensCode4 = false;

    if (hallMaxTravels == maximumHalls) {

        while (1) {
            lastButtonState();
            pollButtons();
            lcd.setCursor(0,0);
// Display intructions
            lcd.print("Are you sure?");
            lcd.setCursor(0,1);
            lcd.print("~ press [select]");

```

```

        if (buttonSelect == HIGH && lastButtonSelect == LOW) {lcd.clear();
break;}          // Only continue once SELECT has been pressed
        else if (buttonRight == HIGH && lastButtonRight == LOW) {
// Secret code to permanently disable sensors
            sensCode1 = true;
            lcd.clear();
            break;
        }
        else if (buttonLeft == HIGH && lastButtonLeft == LOW
            || buttonUp == HIGH && lastButtonUp == LOW
            || buttonDown == HIGH && lastButtonDown == LOW) {
            return;
        }
    }

    while (1) {
        lastButtonState();
        pollButtons();
        lcd.setCursor(0,0);
// Display intructions
        lcd.print("Void warranty??");
        lcd.setCursor(0,1);
        lcd.print("~ press [select]");
        if (buttonSelect == HIGH && lastButtonSelect == LOW) {lcd.clear();
break;}          // Only continue once SELECT has been pressed
        else if (buttonRight == HIGH && lastButtonRight == LOW) {
// Secret code to permanently disable sensors
            sensCode2 = true;
            lcd.clear();
            break;
        }
        else if (buttonLeft == HIGH && lastButtonLeft == LOW
            || buttonUp == HIGH && lastButtonUp == LOW
            || buttonDown == HIGH && lastButtonDown == LOW) {
            return;
        }
    }

    while (1) {
        lastButtonState();
        pollButtons();
        lcd.setCursor(0,0);
// Display intructions
        lcd.print("No plz don't.");
        lcd.setCursor(0,1);
        lcd.print("~ press [right]");
        if (buttonRight == HIGH && lastButtonRight == LOW) {lcd.clear();
break;}          // Only continue once RIGHT has been pressed
        else if (buttonSelect == HIGH && lastButtonSelect == LOW) {
// Secret code to permanently disable sensors
            sensCode3 = true;
            lcd.clear();
            break;
        }
        else if (buttonLeft == HIGH && lastButtonLeft == LOW
            || buttonUp == HIGH && lastButtonUp == LOW
            || buttonDown == HIGH && lastButtonDown == LOW) {

```

```

        return;
    }
}

while (1) {
    lastButtonState();
    pollButtons();
    lcd.setCursor(0,0);
// Display intructions
    lcd.print("You will break!");
    lcd.setCursor(0,1);
    lcd.print("~ press [left]");
    if (buttonLeft == HIGH && lastButtonLeft == LOW) {
// Only continue once LEFT has been pressed
        lcd.clear();
        hallMaxTravels = 2000;
// Hall sensor reading at maximum travel (against the syringe mount)
        animationConfirm();
        lcd.setCursor(0,0);
// Display confirmation
        lcd.print("End sensors");
        lcd.setCursor(0,1);
        lcd.print("disabled");
        delay(1000);
        lcd.clear();
        break;
    }
    else if (buttonUp == HIGH && lastButtonUp == LOW) {
// Secret code to permanently disable sensors
        sensCode4 = true;
        lcd.clear();
        break;
    }
    else if (buttonSelect == HIGH && lastButtonSelect == LOW
        || buttonRight == HIGH && lastButtonRight == LOW
        || buttonDown == HIGH && lastButtonDown == LOW) {
        return;
    }
}

if (sensCode1 == true
    && sensCode2 == true
    && sensCode3 == true
    && sensCode4 == true) {
    EEPROM.write(addrSENS, true);
    hallMaxTravels = 2000;
// Hall sensor reading at maximum travel (against the syringe mount)
    animationConfirm();
    lcd.setCursor(0,0);
// Display intructions
    lcd.print("End sensors");
    lcd.setCursor(0,1);
    lcd.print("PERMANENTLY OFF");
    delay(2000);
    lcd.clear();
}

```

```

    }

    else {
        hallMaxTravelS = maximumHallS;
        sensCode1 = false;
        sensCode2 = false;
        sensCode3 = false;
        sensCode4 = false;
        EEPROM.write(addrSENS, false);
        animationConfirm();
        lcd.setCursor(0,0);
// Display intructions
        lcd.print("End sensors");
        lcd.setCursor(0,1);
        lcd.print("re-enabled");
        delay(1000);
        lcd.clear();
    }
}

//===== ** BYTE TO INT **

unsigned int multiplicationCombine(unsigned int x_high, unsigned int x_low) {
    int combined;
    combined = x_high;
    combined = combined*256;
    combined |= x_low;
    return combined;
}

//===== ** RESTART ANIMATION **

void animationRestart() {

    lcd.clear();

    for (int x=0; x<=15; x++) {
        lcd.setCursor(x,0);
        lcd.print((char)0xFF);
// Filled box
        lcd.setCursor(15-x,1);
        lcd.print((char)0xFF);
// Filled box
        delay(20);
    }

    for (int x=0; x<=15; x++) {
        lcd.setCursor(x,0);
        lcd.print(" ");
        lcd.setCursor(15-x,1);
        lcd.print(" ");
        delay(20);
    }
}

```



```

    delay(100);

    lcd.clear();
}

//===== ** ANIMATION **

void animationConfirm() {

    lcd.clear();

    for (int x=0; x<=15; x++) {
        lcd.setCursor(x,0);
        lcd.print((char)0xFF);
// Filled box
        lcd.setCursor(x,1);
        lcd.print((char)0xFF);
// Filled box
        delay(20);
    }

    delay(200);

    lcd.clear();
}

```

## Appendix B Publications

K.D. Esmerlyan, C.E. Castano, A.H. Bressler, **C.P. Fergusson**, R. Mohammadi, Single-step flame synthesis of carbon nanoparticles with tunable structure and chemical reactivity, *RSC Adv.* 6 (2016) 61620–61629. doi:10.1039/C6RA06436A.

K.D. Esmerlyan, A.H. Bressler, C.E. Castano, **C.P. Fergusson**, R. Mohammadi, Rational strategy for the atmospheric icing prevention based on chemically functionalized carbon soot coatings, *Appl. Surf. Sci.* 390 (2016) 452–460. doi:10.1016/j.apsusc.2016.08.101.

K.D. Esmerlyan, C.E. Castano, A.H. Bressler, M. Abolghasemibizaki, **C.P. Fergusson**, A. Roberts, R. Mohammadi, Kinetically driven graphite-like to diamond-like carbon transformation in low temperature laminar diffusion flames, *Diam. Relat. Mater.* 75 (2017) 58–68. doi:10.1016/j.diamond.2017.01.014.

M. Abolghasemibizaki, C.J. Robertson, **C.P. Fergusson**, R.L. McMasters, R. Mohammadi, Rolling viscous drops on a non-wettable surface containing both micro- and macro-scale roughness, *Phys. Fluids.* 30 (2018). doi:10.1063/1.5016824.

M. Abolghasemibizaki, **C. Fergusson**, R.L. McMasters, R. Mohammadi, Parameter Estimation Involving Droplets on Flat and Cylindrical Non-wettable Surfaces, (2018).

Cite this: *RSC Adv.*, 2016, 6, 61620

# Single-step flame synthesis of carbon nanoparticles with tunable structure and chemical reactivity†

Karekin D. Esmeryan,<sup>ab</sup> Carlos E. Castano,<sup>ac</sup> Ashton H. Bressler,<sup>a</sup> Christian P. Fergusson<sup>a</sup> and Reza Mohammadi<sup>\*a</sup>

A novel method for the flame synthesis of carbon nanoparticles with controllable fraction of amorphous, graphitic-like and diamond-like phases is reported. The structure of nanoparticles was tailored using a conical chimney with an adjustable air-inlet opening. The opening was used to manipulate the combustion of an inflamed wick soaked in rapeseed oil, establishing three distinct combustion regimes at fully-open, half-open and fully-closed opening. Each regime led to the formation of carbon coatings with diverse structure and chemical reactivity through a facile, single-step process. In particular, the fully-closed opening suppressed most of the inlet air, causing an increased fuel/oxygen ratio and decreased flame temperature. In turn, the nucleation rate of soot nanoparticles was enhanced, triggering the precipitation of some of them as diamond-like carbon (DLC). Surface characterization analyses using Raman spectroscopy, X-ray photoelectron spectroscopy and transmission electron spectroscopy confirmed this hypothesis, indicating a short-range ordered nanocrystalline structure and  $\sim 80\%$   $sp^3$  bonds in the coatings deposited at fully-closed opening. Furthermore, three groups of 5 MHz Quartz Crystal Microbalances (QCMs) coated with soot and DLC, corresponding to each of the three combustion regimes, showed different frequency responses to aqueous ethanol and isopropanol solutions in the concentration range of 0–12.5 wt%. The DLC coated QCMs exhibited relatively constant frequency shift of  $\sim 2250$  Hz regardless of the chemical, while the response of soot coated counterparts was influenced by the quantity of heteroatoms in the film. Our method can be applied in chemical sensing for the development of piezoresonance liquid sensors with tunable sensitivity.

Received 10th March 2016

Accepted 19th June 2016

DOI: 10.1039/c6ra06436a

www.rsc.org/advances

## 1. Introduction

Carbon is one of the most remarkable chemical elements, as it is capable of forming a variety of chemical bonds with itself and/or atoms of other elements.<sup>1</sup> Its physicochemical characteristics depend on the structural configuration of the atomic bonds ( $sp^1$ ,  $sp^2$  or  $sp^3$ ) and due to these natural peculiarities, carbon can be found in different forms such as diamond, graphite, fullerenes and amorphous carbon.<sup>2,3</sup> The latter is a metastable phase considered as a mixture of highly disordered carbon atoms with different fractions of  $sp^3$ ,  $sp^2$  and even  $sp^1$  bonding.<sup>1</sup> A major advantage of the amorphous carbon is the ability to exhibit different physicochemical properties by altering the ratio of  $sp^2/sp^3$  bonds and the quantity of heteroatoms<sup>2</sup> (e.g. oxygen). For instance, amorphous carbon films that exhibit a short-range ordered

nanocrystalline structure and significant  $sp^3$  content, known also as diamond-like carbon (DLC), are characterized with enhanced density, wear resistance, chemical inertness and optical transparency.<sup>4–8</sup> On the other hand, the increased amount of  $sp^2$  bonds can transform the coating into a graphite-like carbon with high porosity, leading to a large specific surface area and improved chemical reactivity.<sup>9–11</sup> Therefore, the amorphous carbon coatings have strong potential for a wide range of practical applications, including electrochemical energy storage,<sup>12</sup> active catalysts for the hydrolysis of cellulose,<sup>13</sup> chemical sensors,<sup>14,15</sup> photovoltaic solar cells<sup>16</sup> or artificial knee-hip bioimplants.<sup>17,18</sup>

For each particular application, the content of  $sp^2$  and  $sp^3$  bonds in the coating along with the quantity of heteroatoms can be adjusted to provide the desirable physicochemical characteristics.<sup>2</sup> The best way of implementing this concept is through direct activation,<sup>19</sup> carbonization of crosslinked polymers,<sup>20</sup> chemical vapor deposition,<sup>21</sup> pulsed laser deposition,<sup>22</sup> ion beam/magnetron sputtering<sup>23,24</sup> or glow discharge RF plasma treatment.<sup>25</sup> These techniques are efficient and accurate; however, each of them has specific disadvantages in terms of the deposition rate, film's quality and uniformity, as well as the necessity of expensive equipment (lasers, plasma reactors, chemical chambers, etc.). Furthermore, most of the aforementioned procedures require

<sup>a</sup>Department of Mechanical and Nuclear Engineering, Virginia Commonwealth University, Richmond, VA, 23284, USA. E-mail: rmohammadi@vcu.edu

<sup>b</sup>Georgi Nadjakov Institute of Solid State Physics, 72, Tzarigradsko Chaussee Blvd., 1784 Sofia, Bulgaria

<sup>c</sup>Nanomaterials Core Characterization Facility, Department of Chemical and Life Science Engineering, Virginia Commonwealth University, Richmond, VA, 23284, USA

† Electronic supplementary information (ESI) available. See DOI: 10.1039/c6ra06436a

precise control of the experimental conditions such as vacuum and pressure, which determines the need for specially-designed hermetically sealed chambers. In contrast, the deposition of amorphous carbon films through combustion flame synthesis at atmospheric pressure is a method of fascinating simplicity.<sup>26–35</sup> The flame ensures a chemically reactive environment capable of generating carbon nanostructures in a short and continuous single-step process.<sup>36</sup> Moreover, it has been demonstrated that candle flame consists of four major forms of carbon (diamond, graphite, fullerenes, amorphous carbon), which can be successfully identified using anodic aluminum oxide collectors.<sup>30</sup> Unfortunately, this approach has not yet been extensively used for industrial purposes, because of a few limiting factors. Firstly, to achieve desirable physicochemical properties of the flame-deposited carbon coatings, additional catalysts or chemical reagents may be required, which complicates the process.<sup>34,37–39</sup> Secondly, up to now, the formation of amorphous DLC from various flame configurations and fuel types has been observed only at high substrate temperatures (above 400 °C), which in turn can limit the applicability of the method to materials with low thermal stability.<sup>27,28,32,40</sup>

Here, we present an efficient single-step flame method for the deposition of carbon coatings, whose physicochemical characteristics can be easily manipulated using a conical chimney with an adjustable air-inlet opening. In this study, carbon nanostructures with superhydrophobic or diamond-like properties are derived during the incomplete combustion of rapeseed oil. This is achieved through a precise control of the amount of oxygen involved in the combustion, and subsequently the temperature of the flame, by changing the size of the opening. The major advantage of our approach is the opportunity to tune *in situ* the fraction of amorphous, graphitic-like and diamond-like phases, allowing for the deposition of carbon coatings with substantially different structure and chemical reactivity. Moreover, the proposed method is catalyst-free and does not require high substrate temperatures (see Section 3.1), which is of crucial importance for its wide practical applicability.

## 2. Experimental procedure

### 2.1. Synthesis of the carbon nanoparticles and experimental details

A custom-designed aluminum chimney with an adjustable air-inlet opening, illustrated in Fig. 1, was mounted over an inflamed paper wick soaked in rapeseed oil. The size of the opening was controlled through a circular cover with a diameter of  $d = 6$  cm, which was wrapped around the chimney. This cover was used to tune the inlet oxygen flowing through the narrow  $1.5 \times 2.5$  cm opening, available at the bottom of the chimney. Altering the position of the cover towards the opening allowed *in situ* manipulation of the combustion process and subsequent synthesis of carbon nanoparticles with different fraction of amorphous, graphitic-like or diamond-like phases.

Based on the experimental setup, three distinct combustion regimes were established when the opening was fully-open ( $1.5 \times 2.5$  cm), half-open ( $0.75 \times 2.5$  cm) and fully-closed. The latter cancelled most of the oxygen flow, but since the chimney was not

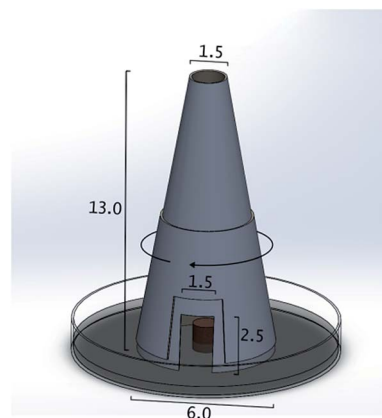


Fig. 1 Schematic representation of the conical chimney with adjustable opening used to synthesize the carbon nanoparticles. The units are given in centimeters.

completely sealed (upon closure, a small  $\sim 0.5$  cm gap remains between the cover and chimney's bottom); the combustion remained continuous, as there was enough oxygen to make the process self-sustaining. After ignition of the fuel (rapeseed oil), square shaped  $2.5 \times 2.5$  cm microscope glass slides (Fisher Scientific, USA), as well as gold electrode quartz crystal microbalances (QCMs) with a fundamental frequency of  $\sim 5$  MHz (SRS, USA) were exposed over the chimney's tip at each regime of combustion, which caused deposition of carbon coatings with various physicochemical characteristics. The film deposition was carried out at burner-to-substrate distance of 7 cm with time duration ranging within 20–60 s, similarly as in our previous work.<sup>35</sup> The flame and substrate temperatures were determined using a TP3001 digital thermometer and Kintrex IRT0421 infrared thermal sensor, respectively. For that purpose, the probe of digital thermometer was placed in the flame, keeping similar distance from the burner (the chimney) such as during the film deposition. The flame temperature was recorded after reaching stable temperature reading, which was obtained for  $\sim 60$  s. In addition, the substrate temperature at each combustion regime was measured through the infrared thermometer coincidentally with the deposition process.

### 2.2. Surface characterization

After the synthesis of particles and subsequent fabrication of the coatings, their morphology, structure, roughness and chemical composition were investigated using scanning electron microscopy (SEM), X-ray diffraction (XRD), atomic force microscopy (AFM), Raman spectroscopy, X-ray photoelectron spectroscopy (XPS) and transmission electron microscopy (TEM). The SEM experiments were performed using a Hitachi SU-70 Field Emission Scanning Electron Microscope and images were taken at low and high magnifications up to 150k. The XRD measurements were carried out with a Panalytical X'Pert Pro diffractometer operating in Bragg–Brentano mode. An incident X-ray beam was generated with Cu K $\alpha$  radiation ( $\lambda = 1.54$  Å) and the samples were scanned from  $5^\circ$  to  $60^\circ$  of  $2\theta$ , at  $0.03^\circ$  scan step size,  $2^\circ$  anti-scatter slit,  $1^\circ$  fixed divergence slit and 15 mm mask. AFM images were taken in

tapping mode in an area of  $1 \times 1 \mu\text{m}$  at a rate of 0.4 Hz with Bruker BioScope Catalyst. Raman spectra of the coatings, deposited at the three distinct regimes, were recorded from 500 to  $2500 \text{ cm}^{-1}$  with an acquisition time of 300 s in a Horiba LabRam HR Evolution Confocal Raman spectrometer, using a 20 mW/532 nm He-Ne laser excitation system. TEM was implemented by a Zeiss Libra 120 system operating at 120 kV with a point to point resolution of 0.34 nm. The high-resolution XPS data were collected with a Thermo Fisher ESCALAB 250 X-ray photoelectron spectrometer at a step of 0.1 eV.

### 2.3. Determination of the physical properties of carbon coatings and their thickness

The electrical resistivity ( $\sigma$ ), apparent density ( $\rho$ ), surface wettability and the thickness of as prepared coatings were determined in several experiments. Four point probe analysis was used for quantitative evaluation of the electrical resistivity of the carbon coatings.<sup>41</sup> For this purpose, an auto-mechanical stage with four equally spaced tungsten metal tips was moved in upward and downward direction. Simultaneously, a high impedance current source was used to supply current through the outer two metal tips, while a voltmeter was measuring the voltage across the two inner probes. The apparent density was defined as a ratio of the mass of the coatings, deposited on  $2.5 \times 2.5 \text{ cm}$  glass slides, towards their volume (thickness). The latter was measured using an optical microscope Nikon eclipse LV100, equipped with a motorized stage ProScan II capable of providing precise focus control by moving the Z-axis in steps as small as 20 nm. Finally, the wettability of the samples was determined through static contact angle (SCA) and contact

angle hysteresis (CAH) measurements for droplets of de-ionized water using a Drop Shape Analyzer (DSA 25E, Krüss Germany).

### 2.4. Proof-of-concept experiments

The hypothesis that the physicochemical performance of carbon coatings, including their chemical reactivity, depends on the ratio of  $\text{sp}^2/\text{sp}^3$  bonds and the quantity of heteroatoms<sup>2</sup> was verified experimentally with nine QCM based chemical sensors. Initially, the QCMs with gold electrode structure, 1 inch diameter and a fundamental frequency of  $\sim 5 \text{ MHz}$  were separated in three groups of three sensors. The first group devices was coated with carbon nanostructures through combustion flame synthesis at fully-open, the second at half-open and the third at fully-closed opening, respectively (see Section 2.1). For each combustion regime, the deposition time was appropriately selected in order to ensure as reproducible as possible film thicknesses from device to device. Subsequently, the QCMs were mounted one at a time in a quartz crystal holder connected to a sensor oscillator SRS25, used to ensure continuous crystal oscillations, and a QCM200 digital controller with a built-in frequency counter. The chemical reactivity of the coatings was investigated by measuring the frequency response of each individual sensor in air and after covering the sensing surface with organic solvents such as ethanol and isopropanol (99%, Sigma-Aldrich). These chemicals were dissolved in de-ionized water, leading to aqueous solutions in the concentration range of 0–12.5 wt%. By analyzing the differences in the frequency response between each group of sensors, it was possible to assess whether the reduction of oxygen affects the chemical reactivity of the coatings. The experiments were performed at constant room temperature in an open lab; therefore,

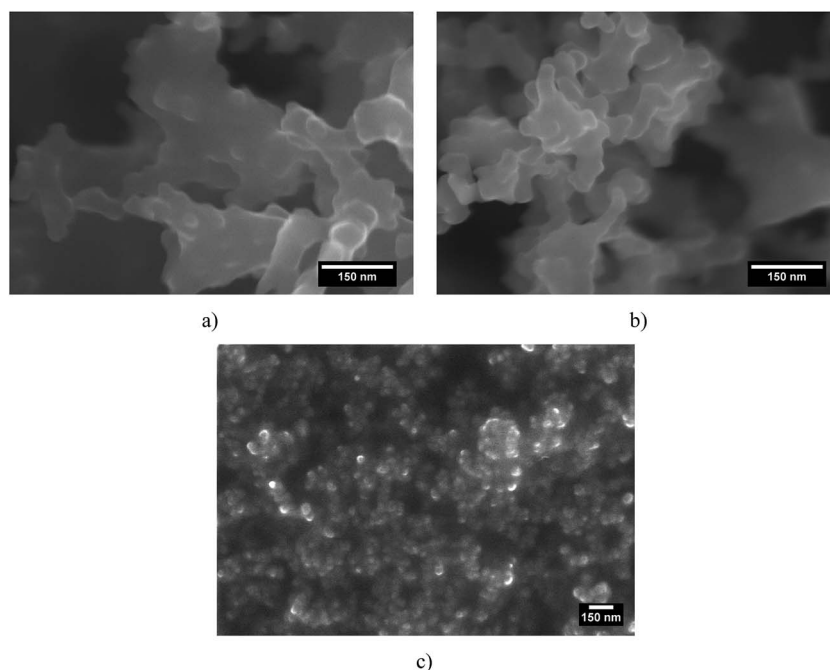


Fig. 2 SEM images of carbon coatings deposited at combustion regime with (a) fully-open, (b) half-open and (c) fully-closed opening.

any possibility for thermally-induced frequency shifts was avoided.<sup>42</sup>

### 3. Results and discussion

#### 3.1. Morphological and structural analysis

Fig. 2 compares the structural and morphological peculiarities of the coatings deposited at three distinct regimes of combustion. The SEM images show that the first two regimes trigger the formation of elongated carbon nanoparticles assembled as islands, separated by micro- and nanoscale pores. Moreover, these particles are disordered, tightly bonded and fused, which corresponds to inherently robust and durable amorphous carbon soot with superhydrophobic properties.<sup>35</sup> In contrast, the image in Fig. 2c reveals a significantly different orientation, shape and size of the particles. They occur as grain clusters with an approximate size of 200 nm. A similar surface profile has previously been observed for diamond-like carbon (DLC), fabricated using ion beam<sup>6</sup> and RF plasma deposition,<sup>43</sup> although the graininess achieved with these methods is much more pronounced. The comparative analysis of our SEM results with those reported for ion beam<sup>6</sup> and RF plasma deposition<sup>43</sup> suggests that at the regime of fully-closed opening (Fig. 2c) the uncombusted polyaromatic hydrocarbons may have precipitated as amorphous DLC films. This hypothesis is supported by our XRD measurements (see the ESI†), which indicate a mainly amorphous structure of the fabricated coatings.

Since such a structural transition has not previously been reported and the reaction mechanism of soot formation in

flames is not completely elucidated,<sup>44,45</sup> it is extremely difficult to provide an exact and comprehensive scientific interpretation of our observations. However, a fairly reasonable explanation of the soot-DLC transformation may come up from the detailed kinetic modeling of soot aggregate formation in laminar pre-mixed flames.<sup>46</sup> According to this model, the soot particle morphology is strongly influenced by the interplay between soot's nucleation, aggregation and initial surface growth that depend on the equivalence fuel/oxygen ratio. In the nucleation region of the flame, the freshly nucleated particles collide, which leads to the formation of fractal aggregates. As the nucleation rate diminishes (at low equivalent ratios *i.e.* large air fraction) and the surface growth becomes prominent, the aggregated particles acquire a spherical shape.<sup>46</sup> In contrast, upon enhanced nucleation at relatively constant surface growth rate, the morphology of the clusters formed through collisions of the incipient particles is significantly altered. As a result, the degree of particles' overlap increases vastly, possibly inducing structural changes in the soot. Such a phenomenon is associated with the increased equivalence fuel/oxygen ratio (reduced oxygen content), which increases the fraction of uncombusted polyaromatic hydrocarbons and triggers more intensive nucleation.<sup>46</sup> In our approach, we manipulate the inlet oxygen flow, and thus the reaction temperature, by changing the size of the opening. At fully-open opening, the substrate temperature after 60 s exposure to the flame at burner-to-substrate distance of 7 cm is  $\sim 160^\circ\text{C}$  and decreases up to  $\sim 60^\circ\text{C}$  upon closing the opening (keeping the same exposure time and distance). Simultaneously, by passing from the first to third

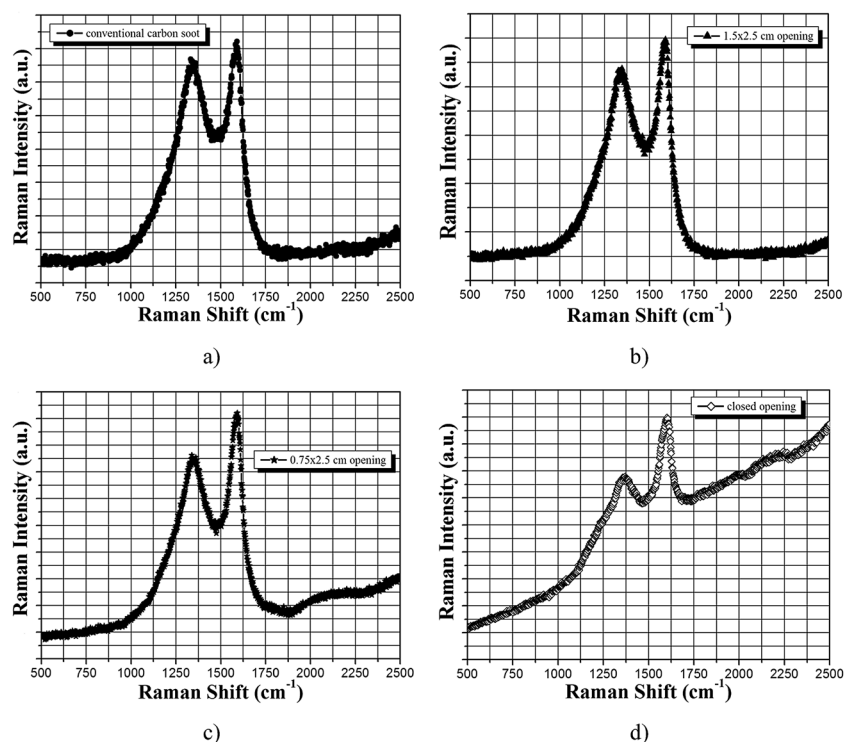


Fig. 3 Raman spectra of (a) conventional carbon soot (deposited without chimney) and after modification with chimney at (b) fully-open, (c) half-open and (d) fully-closed opening.



combustion regime the flame temperature decreases from  $\sim 275$  °C to  $\sim 200$  °C, respectively. This observation correlates well with the kinetic model of soot formation<sup>46</sup> and the fundamentals of combustion,<sup>47</sup> as the reduced oxygen content will result in an increased fuel/oxygen ratio and decreased heat production in the subsequent exothermic chemical reaction. Based on the above considerations, it is likely that at fully-closed opening the nucleation rate in the fume enhances, promoting the morphological changes in the soot *i.e.* its transformation to amorphous DLC.

### 3.2. Chemical state analyses

The SEM imaging was followed by Raman spectroscopy and XPS analyses, summarized in Fig. 3 and 4.

Carbon soot fabricated by the conventional (with no chimney) method has been included too in order to assess how each combustion regime (see Section 2.1) affects the chemical bonds in the coatings. According to Fig. 3, the Raman spectrum of amorphous carbon consists of two distinct bands. The first one at  $1596\text{ cm}^{-1}$  corresponds to an ideal graphitic lattice vibration mode and is denoted as G-band, while the second one, situated at around  $1360\text{ cm}^{-1}$ , is associated with the  $A_{1g}$  symmetry mode of disordered graphitic lattice located at the edges of the graphene layer and is called D-band.<sup>34,48</sup> Qualitative

characterization of the  $sp^2/sp^3$  fraction in the coatings can be implemented by analyzing the intensity changes of G- and D-peaks. As seen in Fig. 3a, the conventional carbon soot is characterized with almost equal intensity of both peaks and the  $I_D/I_G$  ratio is 0.94. This result correlates well with previously reported  $I_D/I_G$  values for amorphous black carbon.<sup>34,48,49</sup> The chimney modification leads to a gradual reduction of the D-peak's intensity, which is an indication of carbon coatings with an increased  $sp^3$  content.<sup>43</sup> Moreover, at fully-closed opening (Fig. 3d), the  $I_D/I_G$  ratio is 0.81, corresponding to a coating with  $\sim 14\%$  less defects compared to the conventional carbon soot. Fig. 4 represents the high-resolution XPS to the C1s for the coatings synthesized at fully-open, half-open and fully-closed opening of the chimney. The deconvolution of the C1s regions is achieved with several peaks corresponding to  $sp^2$  hybrid form of carbon at  $284.8 \pm 0.4\text{ eV}$ ,  $sp^3$  hybridized carbon at  $285 \pm 0.1\text{ eV}$ , hydroxyl groups (C–O) at  $286.5 \pm 0.6\text{ eV}$ , carbonyl groups (C=O) at  $288.9 \pm 0.5\text{ eV}$  and  $\pi-\pi^*$  satellite group at  $291 \pm 2\text{ eV}$ . Upon reducing the chimney's opening and its subsequent closure, the  $sp^2/sp^3$  ratio in the coatings is altered significantly; from 1.27 at fully-open to 0.048 at fully-closed opening, corresponding to coatings with  $\sim 80\%$   $sp^3$  content. Moreover, the nanostructures deposited at the third regime do not contain  $\pi-\pi^*$  satellite peak associated with an electronic structure rearrangement of transition between the  $\pi$  bonding and  $\pi^*$

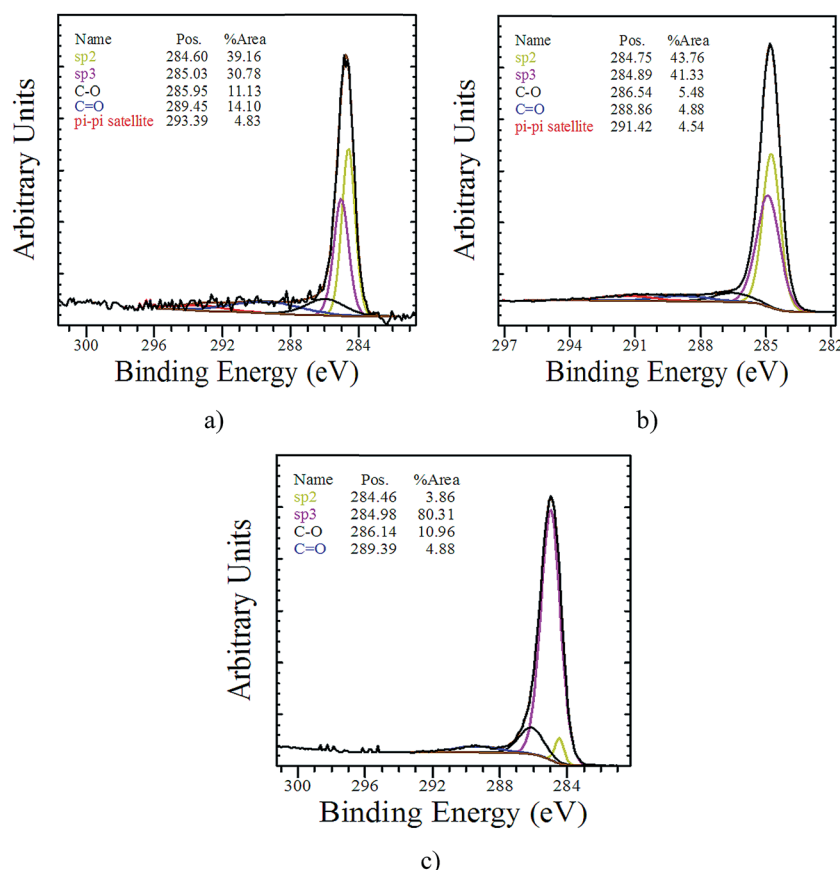


Fig. 4 C 1s photoelectron core level of carbon coatings deposited after modification with chimney at (a) fully-open, (b) half-open and (c) fully-closed opening.

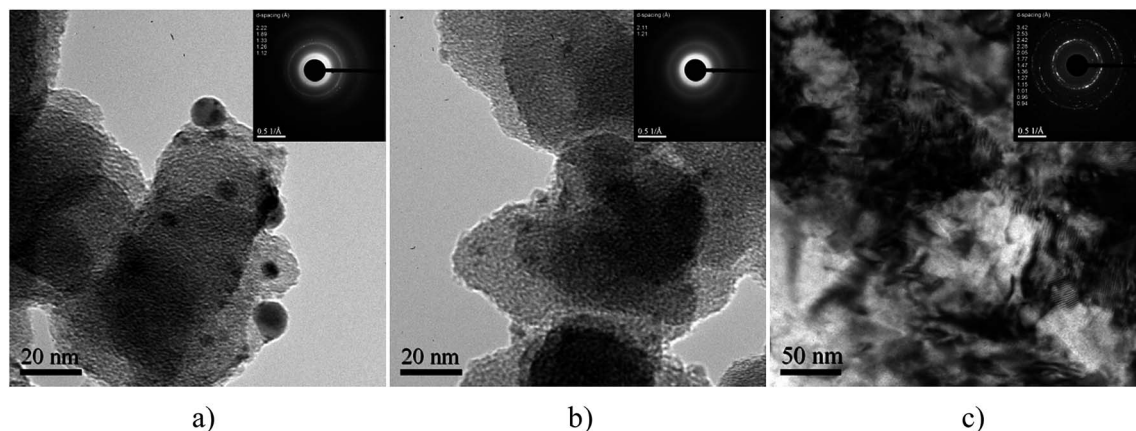


Fig. 5 HRTEM and SAD images of (a) conventional carbon soot (deposited without chimney) and after modification with chimney at (b) fully-open and (c) fully-closed opening.

antibonding states. Also, Fig. 4c shows a more symmetric shape of the C 1s compared to Fig. 4a and b, which is an additional implication that the electronic structure does not suffer rearrangement effects from  $sp^2$  hybridized bonds. Furthermore, the oxygenated functional groups in the layers increase by a factor of 2 when switching from half-open to fully-closed opening. These observations are in good agreement with the scan survey of the coatings (see the ESI†).

Finally, the as prepared carbon coatings were examined through high-resolution transmission electron microscopy (HRTEM) and selected area electron diffraction (SAD), shown in Fig. 5.

The TEM images in Fig. 5 represent the morphological features of the coatings obtained with and without chimney. The conventional soot (without chimney) is characterized with a spherical-like morphology and some lattice fringes could be identified for the larger spheres ( $>20$  nm). In addition, the  $d$ -spacing is not homogeneous along the structures, suggesting a short-range order. Smaller spheres do not present any order, indicating mostly amorphous phase. Also, the SAD pattern showed in Fig. 5a exhibits a few continuous rings and some diffused halos on the sample, which are consistent with the HRTEM image. Similarly, after modification with chimney at fully-open air-inlet opening, an onion-like shape of the particles is observed for most of the areas in the soot and the SAD pattern shows mainly two diffused halos corresponding to a short-range order (Fig. 5b). In this case, the two rings can be assigned to graphitic-like nanostructures.

In contrast, the TEM image in Fig. 5c illustrates more crystalline structure of the coating deposited at fully-closed air-inlet opening. Denser structures with large nanocrystals embedded in an amorphous phase are observed. This morphology differs from the sphere-like and the rings in the SAD pattern are well defined. The atomic  $d$ -spacings in the coating, synthesized at fully-closed opening, can be matched to both graphitic-like and diamond-like structures with less amorphous phase in overall. A summary of these measurements along with the STD  $d$ -spacing for diamond and graphite is presented in Table 1. Although graphitic-like structures are still present, the

appearance of more  $sp^3$  carbon bonds (see Fig. 4c) along with the evidence of nanocrystalline diamond formation (see Table 1) imply that the regime of fully-closed opening tends to form diamond-like carbon (DLC) structures.

### 3.3. Physical properties of the carbon coatings

After full characterization of the carbon nanostructures, their electrical resistivity ( $\sigma$ ), apparent density ( $\rho$ ), surface wettability and thickness were defined experimentally. The coatings synthesized at fully-closed opening showed an electrical resistivity of  $\sigma = 3.6 \times 10^5 \Omega \text{ cm}$ , which is two orders of magnitude higher compared to the values for the conventional soot ( $\sigma = 1\text{--}1.2 \times 10^3$ ). Furthermore, the apparent density of the latter is calculated to be  $\rho \sim 0.04 \text{ g cm}^{-3}$ , similar to the data reported for superamphiphobic layers based on carbon soot.<sup>50</sup> In

Table 1 Comparison between the  $d$ -spacing ( $\text{\AA}$ ) calculated from SAD patterns for conventional soot and after modification with chimney at fully-open and fully-closed opening, and STD  $d$ -spacings for diamond and graphite

$d$ -Spacing measured ( $\text{\AA}$ )			$d$ -Spacing for some C allotropes	
Conventional carbon soot	Fully-open opening	Fully-closed opening	Diamond	Graphite
		3.42		3.4
		2.53		
		2.42		
2.22		2.28		
	2.11	2.05	2.06	2.04
1.89		1.77		1.7
		1.47		
1.33		1.36		
1.26		1.27	1.26	
1.12	1.21	1.15		1.2
		1.01	1.07	
		0.96	0.98	
		0.94		



comparison, the short-range ordered DLC nanostructures possess density of  $\sim 0.59 \text{ g cm}^{-3}$ , indicating decreased porosity. Moreover, the third regime promotes hydrophilic behavior of the coatings determined by low SCA and high CAH of  $70^\circ$  and  $20^\circ$ , respectively. In contrast, the soot exhibits super-hydrophobicity with SCA and CAH being  $155^\circ$  and  $0.5^\circ$ , respectively. These values are another evidence for the observed soot-to-DLC transformation, since the  $\text{sp}^3$ -hybridized diamond-like carbon is hydrophilic in nature due to its high surface energy dominated by the covalent character of the  $\text{sp}^3$  bonds.<sup>51</sup> In addition, all carbon coatings demonstrate linear relationship of their thickness towards the deposition time (see the ESI†). The DLC nanostructures have small thickness of  $\sim 10 \text{ }\mu\text{m}$ , while the carbon soot coatings are characterized with much larger thickness of  $\sim 75\text{--}125 \text{ }\mu\text{m}$  depending on the combustion regime (fully-open or half-open opening). This is attributed to the major differences in the film deposition rate by switching from 1<sup>st</sup> to 3<sup>rd</sup> combustion regime. At fully-open opening, the deposition rate is  $\sim 1.5 \text{ }\mu\text{m s}^{-1}$  and increases up to  $2 \text{ }\mu\text{m s}^{-1}$  at the second regime, which accounts for the reduced oxygen content that degrades the efficiency of combustion and produces more soot.<sup>47</sup> On the other hand, at fully-closed opening the deposition rate is only about  $0.25 \text{ }\mu\text{m s}^{-1}$ , meaning that at this stage the combustion process is significantly altered, as it is confirmed by the surface characterization analyses.

### 3.4. Chemical reactivity assessment

The chemical reactivity of the carbon coatings was assessed through the changes in sensor response of three QCM groups, prior to and after immersion in aqueous ethanol and isopropanol solutions. The choice of these chemicals is related to their practical relevance and harmful impact on the human health when ingested above a certain concentration.<sup>52</sup> Also, both compounds possess similar density, viscosity and surface tension; therefore, the expected differences in the sensor signal from group to group would be ascribed to the quantity of heteroatoms in the film rather than the physical properties of the liquids. Last but not least, as it is pointed in Section 2.4, the carbon nanostructures were deposited in a way ensuring approximately equal film thickness from device to device; thus minimizing the possibility for thickness (mass loading) induced

sensitivity deviations that may compromise the validity of the comparisons.<sup>53,54</sup> For the first two regimes, the film thickness is  $\sim 40 \pm 3 \text{ }\mu\text{m}$ , while at fully-closed opening it is around  $10 \pm 1 \text{ }\mu\text{m}$ . These values along with the density of carbon materials gave relatively similar mass loading expressed through frequency downshifts within  $700\text{--}870 \text{ Hz}$ . Based on the above considerations, the chemical reactivity of the conventional carbon soot is not considered in the research, since this material is inherently brittle and needs additional stabilization using various stabilizers.<sup>35</sup> Thus, the overall massloading on the sensor surface, caused by the stabilizers, would change the QCM's sensitivity, which would compromise the comparative analysis.<sup>54</sup>

Fig. 6 displays the liquid phase frequency response of each QCM group towards aqueous ethanol and isopropanol solutions in the concentration range of  $0\text{--}12.5 \text{ wt}\%$ . The first major distinction in the chemical reactivity of the samples is identified upon immersion in de-ionized water ( $0 \text{ wt}\%$ ). As seen, the QCMs coated with carbon soot (fully-open and half-open opening) decrease their resonance frequency with  $\Delta f \sim 150\text{--}250 \text{ Hz}$ , corresponding to three to five times lower frequency shift in comparison with the theoretical model for an uncoated QCM.<sup>55</sup> On the other hand, the dynamic resistance of these sensors (not shown here) remains relatively constant. Such resonance behavior is attributed to a phenomenon called “decoupling of the liquid phase sensor response”. This effect occurs due to the strong reflection boundary at the solid–air interface, arisen from the “air plastron” of the super-hydrophobic carbon soot, leading to lower amount of energy interacting with the liquid.<sup>56</sup>

Moreover, as evident from Fig. 6, the quantity of heteroatoms in the soot coatings is crucial for their chemical reactivity. The nanostructures fabricated at the first combustion regime have twice more polar functional groups (C–OH) compared to those at the second regime (see Fig. 4). Thus, the first group QCMs exhibits higher sensor response to de-ionized water, as more oxygen atoms available on the sensing surface, more hydrogen bonds would be formed (see Fig. 6a and b). Such a process will increase the overall mass loading on the surface, which will result in additional frequency downshift, according to the Sauerbrey equation.<sup>57</sup> In addition, the sensors coated with DLC

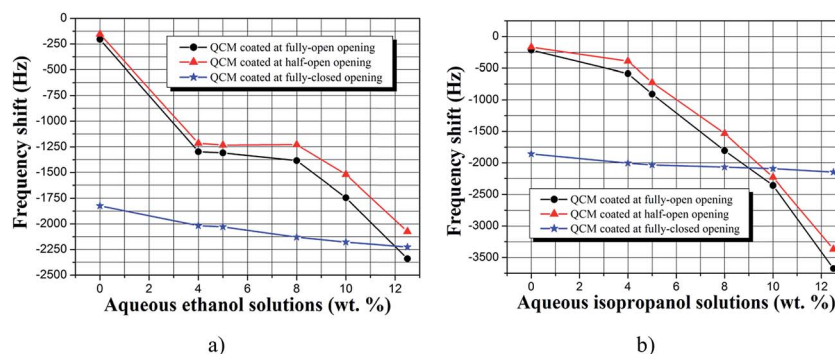


Fig. 6 Frequency response of each sensor group to aqueous solutions of (a) ethanol and (b) isopropanol in the concentration range of  $0\text{--}12.5 \text{ wt}\%$ .

Table 2 Sensitivity and detection limit of each QCM group towards aqueous ethanol and isopropanol solutions

QCM group	Target analyte	$\Delta C$ (mg mL <sup>-1</sup> )	$\Delta f$ (Hz)	$\Delta f/\Delta C$ (Hz mg <sup>-1</sup> mL <sup>-1</sup> )	Detection limit (mg mL <sup>-1</sup> s <sup>-1</sup> )
1	Ethanol	121	2135	17.6	0.85
2		121	1920	15.9	0.94
3		121	401	3.3	4.5
1	Isopropanol	121	3462	28.6	0.52
2		121	3201	26.5	0.57
3		121	292	2.4	6.25

decrease their resonance frequency with more than 1800 Hz after immersion in de-ionized water. This observation correlates well with the increased amount of oxygenated functional groups in the DLC nanostructures. As shown by the XPS analysis, the C–O content in the coatings increases by a factor of two upon passing from half-open to fully-closed opening of the chimney.

The second difference in the chemical performance of the coatings is expressed through the overall resonance behavior of the sensors. For instance, the soot coated QCMs (the first two regimes) demonstrate a non-linear frequency shift when the ethanol concentration increases from 0 to 12.5 wt%. Moreover, there is a large 1.3 kHz step change at 4 wt% followed by a relatively constant sensor signal up to 8 wt%. In comparison, the step change to isopropanol is only 400 Hz and further increase in its concentration causes a proportional quasilinear frequency response. Last but not least, regardless of the chosen chemical, the coatings synthesized at half-open opening exhibit weaker chemical reactivity compared to those deposited at fully-open opening. These results imply that the main chemical reaction is of oxygen–hydrogen type; therefore the coatings with less heteroatoms (oxygen) induce lower sensor signal. Also, isopropanol has more hydrogen molecules compared to ethanol, leading to higher sensitivity of the QCM. As seen, the coatings deposited at the first combustion regime exhibit  $\sim 1.6$  times higher sensitivity to isopropanol in comparison with that to ethanol ( $\Delta f_{\text{C}_3\text{H}_8\text{O}} \sim 2350$  Hz while  $\Delta f_{\text{C}_3\text{H}_7\text{O}} \sim 3750$  Hz). Similar trend is observed for the layers precipitated at the second regime (see Fig. 6). Furthermore, the concentration of 12.5 wt% appears to be a threshold, at which the soot loses superhydrophobicity and the resonance frequency does not recover its initial value (baseline). This effect is associated with a wetting state transition from the suspended Cassie–Baxter to the “sticky” Wenzel state due to a chemical and structural modification of the surface caused by ethanol and isopropanol<sup>58</sup> (see also the ESI†). However, the carbon soot could restore its water repellency by additional hydrophobic chemical treatment, which makes this material appropriate for multiple usages in QCM based gas or liquid sensors.<sup>14,15,58</sup>

In complete contrast, the DLC coated QCMs recover their resonance frequency with negligible deviations from the baseline within  $\pm 1$  Hz and demonstrate relatively constant sensitivity regardless of the chosen chemical. Such behavior is expected since the DLC coatings are chemically inert, meaning that their surface structure remains unaltered upon contact

with 12.5 wt% of ethanol or isopropanol. Moreover, this material is smooth on a nanometric scale, which reduces the number of active adsorption sites interacting with the liquid. The root mean square roughness ( $R_{\text{rms}}$ ) estimated through AFM is  $R_{\text{rms}} = 37$  nm, indicating  $\sim 3$ – $3.5$  times smoother surface profile compared to the carbon soot<sup>14,15,35</sup> (see the ESI†). Although DLC is characterized with an increased quantity of oxygenated functional groups, the total number of active sites is reduced. Therefore, the quantity of hydrogen molecules interacting with the layer would be the same despite of the molecular weight of the chemicals (ethanol or isopropanol).

For the sake of completeness, we determined the detection limit of the sensors and the results are summarized in Table 2.

The sensitivity is defined as the frequency change  $\Delta f$  towards the target analyte concentration change  $\Delta C$  and along with the sensor's short-term stability determines its detection limit.<sup>59</sup> In this study, during the liquid-phase measurements, the resonance frequency was stabilized within  $\pm 1$ – $5$  Hz s<sup>-1</sup>. Therefore, the noise level was estimated at its maximum of  $\pm 5$  Hz s<sup>-1</sup>, while the signal-to-noise ratio was 3 : 1. Since the capacity of the quartz crystal holder is approximately 1 mL, 12.5 wt% of ethanol and isopropanol are corresponding to  $\sim 121$  mg mL<sup>-1</sup>. As evident from Table 2, the soot coated 5 MHz QCMs yield detection limit to ethanol up to 850  $\mu\text{g mL}^{-1}$ , which is  $\sim 2$  times higher resolution in comparison to their uncoated QCM counterparts.<sup>58</sup> Although our sensors do not provide resolution of ng mL<sup>-1</sup> or pg mL<sup>-1</sup>, further optimization of the signal-to-noise ratio would provide lower detection limit.<sup>59</sup>

## 4. Conclusions

In this paper, we described a novel and efficient single-step flame method for deposition of carbon coatings with substantially different physical and chemical characteristics. This was achieved using a conical chimney with an adjustable air-inlet opening, mounted over an ignited wick immersed in rapeseed oil. The opening was used for *in situ* manipulation of the combustion process and subsequent fabrication of nanostructures with different content of amorphous, graphitic-like and diamond-like phases. The SEM and TEM analyses revealed the formation of coatings with distinct morphology; from tightly connected and fused nanoparticles, to grain clusters with approximate size of 200 nm and short-ordered nanocrystalline diamond structure. Such a structural diversity was associated with soot-to-DLC transformation triggered by the

increase of the equivalence fuel/oxygen ratio. In addition, the Raman Spectroscopy and XPS showed that the DLC coatings are characterized with low D-band intensity and  $\sim 80\%$  of  $sp^3$  bonds. Furthermore, these layers were found to possess hydrophilicity, whereas their soot counterparts exhibited superhydrophobicity with SCA and CAH being  $155^\circ$  and  $0.5^\circ$ , respectively. Also, the coatings deposited at fully-closed opening were thinner, denser and less conductive compared to the soot. Finally, major differences in the chemical reactivity of as prepared nanostructures were observed by analyzing the frequency response of three groups of 5 MHz QCMs, upon immersion in aqueous ethanol and isopropanol solutions. The frequency shift of the soot coated sensors was strongly influenced by the presence of polar C–OH groups, as well as the molecular weight of the chemicals. In contrast, the DLC coated QCMs exhibited relatively constant sensor signal regardless of the analyte, which was attributed to their smooth surface and reduced amount of active adsorption sites. Our investigations are prerequisite for rapid and inexpensive fabrication of carbon coatings with custom physicochemical properties.

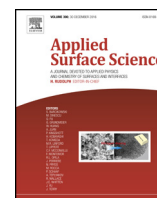
## Acknowledgements

The authors wish to gratefully acknowledge the research group of Prof. Hadis Morkoc at the VCU Department of Electrical and Computer Engineering for implementing the four point probe analysis. Services in support of the project were provided by the VCU Massey Cancer Center, supported in part with funding from NIH-NCI P30CA016059. Also, the startup support from Virginia Commonwealth University under grant 137422 is greatly acknowledged.

## References

- 1 D. R. McKenzie, *Rep. Prog. Phys.*, 1996, **59**, 1611–1664.
- 2 J. A. Menendez-Diaz and I. Martin-Gullon, *Activated carbon surfaces in environmental remediation*, ed. T. J. Bandoz, Elsevier, 2006, pp. 1–48, ch. 1.
- 3 J. C. Anqus and C. C. Hayman, *Science*, 1988, **241**, 913–921.
- 4 M. Chhowalla, J. Robertson, C. W. Chen, S. R. P. Silva, C. A. Davis, G. A. J. Amaratunga and W. I. Milne, *J. Appl. Phys.*, 1997, **81**, 139–145.
- 5 J. Robertson, *Mater. Sci. Eng., R*, 2002, **37**, 129–281.
- 6 P. K. Chu and L. Li, *Mater. Chem. Phys.*, 2006, **96**, 253–277.
- 7 C. R. Lin, H. M. Chang and C. K. Chang, *Int. J. Photoenergy*, 2013, **2013**, 612163.
- 8 N. Dwivedi, S. Kumar, J. D. Carey, R. K. Tripathi, H. K. Malik and M. K. Dalai, *ACS Appl. Mater. Interfaces*, 2013, **5**, 2725–2732.
- 9 D. Liu, P. Yuan, D. Tan, H. Liu, M. Fan, A. Yuan, J. Zhu and H. He, *Langmuir*, 2010, **26**, 18624–18627.
- 10 F. Xu, Z. Tang, S. Huang, L. Chen, Y. Liang, W. Mai, H. Zhong, R. Fu and D. Wu, *Nat. Commun.*, 2015, **6**, 7221.
- 11 J. Huang, J. Wang, C. Wang, H. Zhang, C. Lu and J. Wang, *Chem. Mater.*, 2015, **27**, 2107–2113.
- 12 D. S. Su and R. Schlogl, *ChemSusChem*, 2010, **3**, 136–168.
- 13 S. Suganuma, K. Nakajima, M. Kitano, D. Yamaguchi, H. Kato, S. Hayashi and M. Hara, *J. Am. Chem. Soc.*, 2008, **130**, 12787–12793.
- 14 K. D. Esmeryan, T. A. Yordanov, L. G. Vergov, Z. G. Raicheva and E. I. Radeva, *IEEE Sens. J.*, 2015, **15**, 6318–6325.
- 15 K. D. Esmeryan, V. Georgieva, L. Vergov and J. Lazarov, *Bulg. Chem. Commun.*, 2015, **47**, 1039–1044.
- 16 H. Zhu, J. Wei, K. Wang and D. Wu, *Sol. Energy Mater. Sol. Cells*, 2009, **93**, 1461–1470.
- 17 R. Hauert, K. Thorwarth and G. Thorwarth, *Surf. Coat. Technol.*, 2013, **223**, 119–130.
- 18 C. A. Love, R. B. Cook, T. J. Harvey, P. A. Dearnley and R. J. K. Wood, *Tribol. Int.*, 2013, **63**, 141–150.
- 19 L. Wei, M. Sevilla, A. B. Fuertes, R. Mokaya and G. Yushin, *Adv. Funct. Mater.*, 2012, **22**, 827–834.
- 20 Z. H. Li, D. C. Wu, Y. R. Liang and R. W. Fu, *J. Am. Chem. Soc.*, 2014, **136**, 4805–4808.
- 21 M. Bojiang and Y. Qingxian, *Appl. Surf. Sci.*, 2012, **258**, 4750–4755.
- 22 G. Matenoglou, G. A. Evangelakis, C. Kosmidis, S. Foulis, D. Papadimitriou and P. Patsalas, *Appl. Surf. Sci.*, 2007, **253**, 8155–8159.
- 23 A. Ibenskas, A. Galdikas, S. Meskinis, M. Andrulevicius and S. Tamulevicius, *Diamond Relat. Mater.*, 2011, **20**, 693–702.
- 24 O. Durand-Drouhin, M. Benlahsen, M. Clin and R. Bouzerar, *Appl. Surf. Sci.*, 2004, **223**, 269–274.
- 25 K. D. Esmeryan, E. I. Radeva and I. D. Avramov, *J. Phys. D: Appl. Phys.*, 2016, **49**, 025309.
- 26 W. A. Carrington, L. M. Hanssen, K. A. Snail, D. B. Oakes and J. E. Butler, *Metall. Trans. A*, 1989, **20**, 1282–1284.
- 27 L. M. Hanssen, K. A. Snail, W. A. Carrington, J. E. Butler, S. Kellogg and D. B. Oakes, *Thin Solid Films*, 1991, **196**, 271–281.
- 28 I. Doi, M. S. Haga and Y. E. Nagai, *Diamond Relat. Mater.*, 1999, **8**, 1682–1685.
- 29 M. Qu, J. He and B. Cao, *Appl. Surf. Sci.*, 2010, **257**, 6–9.
- 30 Z. Su, W. Zhou and Y. Zhang, *Chem. Commun.*, 2011, **47**, 4700–4702.
- 31 X. Deng, L. Mammen, H. J. Butt and D. Volmer, *Science*, 2012, **335**, 67–70.
- 32 H. M. Zhu, S. M. Lei and T. C. Kuang, *Adv. Mater. Res.*, 2013, **750–752**, 2100–2103.
- 33 K. Seo, M. Kim and D. H. Kim, *Carbon*, 2014, **68**, 583–596.
- 34 B. N. Sahoo and B. Kandasubramanian, *RSC Adv.*, 2014, **4**, 11331–11342.
- 35 K. D. Esmeryan, C. E. Castano, A. H. Bressler, M. Abolghasemibizaki and R. Mohammadi, *Appl. Surf. Sci.*, 2016, **369**, 341–347.
- 36 W. M. Merchan, A. V. Saveliev, L. Kennedy and W. C. Jimenez, *Prog. Energy Combust. Sci.*, 2010, **36**, 696–727.
- 37 K. Saito, A. S. Gordon, F. A. Williams and W. F. A. Stickle, *Combust. Sci. Technol.*, 1991, **80**, 103–119.
- 38 R. L. Vander Wal, L. J. Hall and G. M. Berger, *J. Phys. Chem. B*, 2002, **106**, 13122–13132.
- 39 R. L. Vander Wal, *Combust. Flame*, 2002, **130**, 37–47.
- 40 H. Zhu, T. Kuang, B. Zhu, S. Lei, Z. Liu and S. P. Ringer, *Nanoscale Res. Lett.*, 2011, **6**, 331.

- 41 A. P. Schuetze, W. Lewis, C. Brown and W. J. Geerts, *Am. J. Phys.*, 2004, **72**, 149–153.
- 42 K. D. Esmeryan, I. D. Avramov and E. I. Radeva, *Sens. Actuators, B*, 2015, **216**, 240–246.
- 43 V. S. Yadav, D. K. Sahu, M. Singh and K. Kumar, *Proc.–World Congr. Eng. Comput. Sci.*, 2009, **1**, 78–81.
- 44 O. I. Smith, *Prog. Energy Combust. Sci.*, 1981, **7**, 275–291.
- 45 M. Frenklach, *Phys. Chem. Chem. Phys.*, 2002, **4**, 2028–2037.
- 46 M. Balthasar and M. Frenklach, *Combust. Flame*, 2005, **140**, 130–145.
- 47 S. P. Burke and T. E. W. Schumann, *Ind. Eng. Chem.*, 1928, **20**, 998–1004.
- 48 A. Sadezky, H. Muckenhuber, H. Grothe, R. Niessner and U. Pöschl, *Carbon*, 2005, **43**, 1731–1742.
- 49 Y. Gao, Y. S. Zhou, W. Xiong, M. Wang, L. Fan, H. Rabiee-Golgir, L. Jiang, W. Hou, X. Huang, L. Jiang, J. F. Silvain and Y. F. Lu, *ACS Appl. Mater. Interfaces*, 2014, **6**, 5924–5929.
- 50 M. Paven, P. Papadopoulos, L. Mammen, X. Deng, H. Sachdev, D. Vollmer and H. J. Butt, *Pure Appl. Chem.*, 2014, **86**, 87–96.
- 51 Y. Zhou, X. Song, E. Li, G. Li, S. Zhao and H. Yan, *Appl. Surf. Sci.*, 2006, **253**, 2690–2694.
- 52 D. Jammalamadaka and S. Raissi, *Am. J. Med. Sci.*, 2010, **339**, 276–281.
- 53 D. S. Ballantine Jr, S. J. Martin, A. J. Ricco, G. C. Frye, H. Wohltjen, R. M. White and E. T. Zellers, *Acoustic wave sensors: theory, design and physico-chemical applications*, Elsevier, 1st edn, 1997, pp. 222–230, ch. 5.
- 54 G. McHale, M. I. Newton and F. Martin, *J. Appl. Phys.*, 2003, **93**, 675–690.
- 55 K. K. Kanazawa and J. G. Gordon, *Anal. Chem.*, 1985, **57**, 1770–1772.
- 56 G. McHale, P. Roach, C. R. Evans, N. J. Shirtcliffe, S. J. Elliott and M. I. Newton, *Proc. IEEE Freq. Control Symp.*, 2008, 698–704.
- 57 Z. G. Sauerbrey, *Physics*, 1959, **155**, 206–222.
- 58 K. D. Esmeryan, G. McHale, C. L. Trabi, N. R. Geraldi and M. I. Newton, *J. Phys. D: Appl. Phys.*, 2013, **46**, 345307.
- 59 L. R. Pardo, J. F. Rodriguez, C. Gabrielli, H. Perrot and R. Brendel, *IEEE Sens. J.*, 2005, **5**, 1251–1257.



# Rational strategy for the atmospheric icing prevention based on chemically functionalized carbon soot coatings

Karekin D. Esmeryan<sup>a,b</sup>, Ashton H. Bressler<sup>a</sup>, Carlos E. Castano<sup>a,c</sup>, Christian P. Fergusson<sup>a</sup>, Reza Mohammadi<sup>a,\*</sup>

<sup>a</sup> Department of Mechanical and Nuclear Engineering, Virginia Commonwealth University, Richmond, VA, 23284, USA

<sup>b</sup> Georgi Nadjakov Institute of Solid State Physics, 72, Tzarigradsko Chaussee Blvd., 1784 Sofia, Bulgaria

<sup>c</sup> Nanomaterials Core Characterization Facility, Department of Chemical and Life Science Engineering, Virginia Commonwealth University, Richmond, VA, 23284, USA

## ARTICLE INFO

### Article history:

Received 16 June 2016

Received in revised form 12 August 2016

Accepted 20 August 2016

Available online 28 August 2016

### Keywords:

Anti-icing

Carbon soot

Freezing time

Icephobicity

Impact dynamics

Superhydrophobicity

## ABSTRACT

Although the superhydrophobic surfaces are preferable for passive anti-icing systems, as they provide water shedding before initiation of ice nucleation, their practical usage is still under debate. This is so, as the superhydrophobic materials are not necessarily icephobic and most of the synthesis techniques are characterized with low fabrication scalability. Here, we describe a rational strategy for the atmospheric icing prevention, based on chemically functionalized carbon soot, suitable for large-scale fabrication of superhydrophobic coatings that exhibit and retain icephobicity in harsh operational conditions. This is achieved through a secondary treatment with ethanol and aqueous fluorocarbon solution, which improves the coating's mechanical strength without altering its water repellency. Subsequent experimental analyses on the impact dynamics of icy water droplets on soot coated aluminum and steel sheets show that these surfaces remain icephobic in condensate environments and substrate temperatures down to  $-35^{\circ}\text{C}$ . Furthermore, the soot's icephobicity and non-wettability are retained in multiple icing/de-icing cycles and upon compressed air scavenging, spinning and water jetting with impact velocity of  $\sim 25\text{ m/s}$ . Finally, on frosted soot surfaces, the droplets freeze in a spherical shape and are entirely detached by adding small amount of thermal energy, indicating lower ice adhesion compared to the uncoated metal substrates.

© 2016 Elsevier B.V. All rights reserved.

## 1. Introduction

The atmospheric icing is a natural phenomenon that occurs when supercooled water droplets in the atmosphere freeze upon impact on solid objects [1]. Supercooling is a process of lowering the temperature of a liquid below its freezing point, without triggering a phase transition to a solid [2]. Normally, the water freezes around  $0^{\circ}\text{C}$ , but in certain circumstances (high purity or lack of nucleation sites) it could be supercooled down to its homogeneous nucleation temperature ( $-48.3^{\circ}\text{C}$ ) [3]. In turn, the supercooled water droplets could freeze almost instantly (units of seconds) upon contact with a solid surface, which may lead to catastrophic socioeconomic consequences. For instance, even a thin ice layer is sufficient to destroy the high-voltage power lines or telecommunication networks, leaving hundreds of households with no electricity and

telecommunications [4]. Furthermore, the ice accretion on the wings, propellers and rotor blades of the aircrafts can cause a loss of aerodynamics [5] or excessive vibrations due to imbalanced rotors [6] that sometimes lead to fatal accidents [7,8]. In addition, the icing of cold-region wind turbines degrades their operation efficiency and may reduce the energy production and lifetime of the turbine [9,10].

The most common strategies for icing protection include electro-thermal and mechanical systems, which use electric current or mechanical vibrations to suspend the accumulated ice [11]. However, the electro-thermal approach covers only the leading edge of the wing or rotor blade and requires materials with high thermal conductivity [11]. In turn, such systems are prone to “runback ice” formation and along with their bulkiness and cyclic operation (to reduce the power consumption) are economically inexpedient [11]. Furthermore, the efficient operation of mechanical systems is restricted by the elastic, dielectric or piezoelectric losses in the actuator, which reduces the overall mechanical stress applied to overcome the ice adhesion forces [12,13]. On

\* Corresponding author.

E-mail address: [rmohammadi@vcu.edu](mailto:rmohammadi@vcu.edu) (R. Mohammadi).



the other hand, the usage of chemical reagents for icing mitigation or prevention has the advantage of being passive (no external power required) and therefore, a low weight and reliable technique. Various chemicals are incorporated into coatings with an aim to dissolve the incipient ice, but some of them can corrode the protected surface and need to be monitored and replaced frequently [14].

Alternatively, the interest in superhydrophobic materials as passive anti-icing systems has rapidly increased over the past decade [15–18]. The concept of icephobicity of the superhydrophobic surfaces relies on their extreme non-wettability upon contact with water, as well as the ability to promote rebound of the impacting liquid droplets [19]. It has been argued that the impingement of water droplets on superhydrophobic surfaces leads to a transfer between the kinetic and surface energy of the liquid and subsequent droplet rebound [20]. As a result, the solid-liquid contact time decreases down to a few milliseconds, hence, the exchanged thermal energy is insufficient to trigger nucleation and the water is shed-off before freezing. Moreover, the suspended Cassie-Baxter state of the superhydrophobic materials minimizes the solid-liquid contact area, thereby reduces the heat transfer rate and the icing probability, which is a function of the surface area and wettability [21–23]. Furthermore, even if nucleation occurs, the air trapped at the solid-liquid interface reduces the actual ice-coated surface area and disrupts the bonding by creating stress concentrations [16]. Thus, the ice adhesion forces are significantly weakened, which decreases up to 80% the amount of energy required to keep the protected surface free of ice [19].

Although superhydrophobic surfaces (coatings) are very promising for passive icing protection, their applicability is yet under debate, because of several important technological factors. Firstly, by definition the terms “superhydrophobicity” and “icephobicity” are different, and as stated elsewhere not every superhydrophobic surface (coating) can exhibit icephobicity [24,25]. The reason is that the critical size of the particles that makeup the surface is in different length scales for superhydrophobicity and icephobicity [24]. For instance, ice does not form on surfaces coated with organosilane-modified silica particles with diameters between 20 and 50 nm; however, the icing probability increases remarkably when the particle diameter is larger than 50 nm [24]. Despite that, the same surfaces support superhydrophobicity in the entire range of particle sizes. Also, the water and ice adhere differently to the substrate, as the force needed to detach a water droplet depends on the contact angle hysteresis, while the force required to detach a piece of ice depends on the receding contact angle and the initial size of interfacial cracks [25]. Secondly, the humid environments introduce a major challenge to the usage of superhydrophobic surfaces, as the water vapor may condense both on top and between the surface asperities, causing frost formation and freezing of the impacting water droplets [1,26]. Thirdly, some superhydrophobic surfaces cannot withstand harsh operational conditions (heavy rains, gusty winds, sand particles, thermal drifts, multiple icing/de-icing cycles, etc.) and their icephobicity is degraded after a few experimental tests [27,28]. Finally, even if the above mentioned shortcomings are circumvented, most of the available synthesis techniques are characterized with low fabrication scalability (e.g. efficiency only at small scales, high cost, etc.) [28]. The latter is of crucial importance for the industrial applicability of the icephobic/superhydrophobic materials and as mentioned elsewhere, the problem of fabrication scalability and the good degree of robustness have received less attention in the literature to date, and they need to become a research priority [28]. There are some investigations in regard to the mechanical durability of the superhydrophobic coatings [29,30], but most of the approaches do not comply with the requirement for high fabrication scalability.

Therefore, the emphasis of this paper is on the anti-icing performance of chemically functionalized carbon soot coatings that are

suitable for large-scale fabrication of durable icephobic surfaces. Inspired from our recent technology for synthesis of inherently robust soot coatings [31] and the possibility to reinstate their water repellency through a secondary treatment with fluorocarbon solution [32], we demonstrate that after functionalization with ethanol and fluorocarbon the mechanical strength and surface adhesion of the soot are significantly improved. Thus, the major advantage of the as prepared coatings is related with their ability to exhibit icephobicity in multiple icing/de-icing cycles in cold humid environments. In addition, the soot coated surfaces are capable of retaining their non-wetting properties upon simulation of harsh operational conditions such as gusty winds, heavy rains or high rotational velocities. Herein, the proposed technique is characterized with high fabrication scalability, as it is time-efficient (icephobic coatings can be fabricated within a few minutes), inexpensive (compared to most of the available methods), suitable for large-scale objects and highly reproducible.

## 2. Methods

### 2.1. Chemical functionalization of the carbon soot coatings

The model substrates were prepared by cutting 3 mm thick sheets of aluminum (6061) and steel (1018) alloys (McMaster-Carr) into  $25 \times 25$  mm squares. All samples were cleaned with acetone (99%, Sigma-Aldrich) and coated with carbon soot by exposing them for 20 s over a black fume released from a conical chimney, used to manipulate the combustion process of rapeseed oil [31]. Afterwards, each sample was gently immersed in ethanol (99%, Sigma-Aldrich) for 5 s and dried for 2 min at  $100^\circ\text{C}$  using a hot plate. Subsequently, the substrates were treated with fluorocarbon solution (Grangers Performance Proofer, UK) designed for water-proof breathable fabrics. The chemical emulsion, which is mainly composed of a block copolymer of perfluorocarbon and polyvinylalcohol [33], was diluted in de-ionized water by a factor of 7 and the samples were immersed in it for 10 min at room temperature. Finally, each substrate was dried for 3 min at  $100^\circ\text{C}$  in order to remove the excessive chemical residues.

### 2.2. Surface characterization and wettability

The morphology and surface roughness of the soot coated substrates prior to and after chemical functionalization were examined using scanning electron microscopy (SEM) and atomic force microscopy (AFM). The SEM experiments were performed using a Hitachi SU-70 Field Emission Scanning Electron Microscope and images were taken with magnifications up to 50k, while the AFM images were obtained in tapping mode with Bruker BioScope Catalyst for an area of  $1 \times 1 \mu\text{m}$  at a rate of 0.4 Hz. The chemical composition of the coatings was investigated qualitatively by energy dispersive spectroscopy (EDS) at 15 KeV using an EDAX detector with an active area of  $10 \text{ mm}^2$ . The surface wettability of the samples was determined through static contact angle (SCA) and contact angle hysteresis (CAH) measurements for  $3 \mu\text{l}$  droplets of de-ionized water by using a Drop Shape Analyzer (DSA 25E, Krüss Germany).

### 2.3. Icing experiments

The system for these experiments was based on a Summit VLT650 Laboratory Upright Freezer, depicted in Fig. 1. The door of the freezer was replaced with 50 mm thick polystyrene foam, in the middle of which a  $150 \times 300$  mm window of polished acrylic plate was installed. A wood platform, used as a sample holder, was placed inside the freezer and its tilt angle was manipulated through an MG 995 servo motor. This process was controlled with  $\pm 0.2^\circ$  accuracy

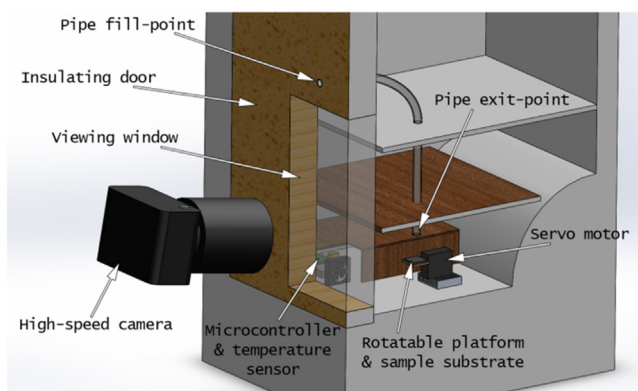


Fig. 1. Scheme of the experimental setup.

by an Arduino Micro Controller linked to a laptop. In addition, a second controller was used to measure the temperature levels, which were displayed on a 40 mm screen. All electronic components were powered by a modular 450 W computer power supply.

Initially, uncoated, as well as soot coated aluminum and steel sheets were mounted one at a time on the holder and positioned at fixed tilt angles ( $\theta = 0, 10, 30$  and  $50^\circ$ ). Subsequently, 200  $\mu\text{l}$  of icy water ( $\sim 0^\circ\text{C}$ ) were dropped on the samples through a plastic capillary tube and the incoming water flow was controlled using a rubber dust blower (known also as air ball). In fact, depending on the applied mechanical force, the air ball was capable of creating water droplets with relatively equal size and impact velocity. Therefore, icy water droplets with various diameters in the range of 1–8 mm were formed at the tip of the tube and impinged on the sample's surface from a fixed distance of 70 mm. The tests were done at impact velocities within 1–5 m/s, corresponding to droplet dynamics at Weber and Reynolds numbers of  $We \sim 14$ –897 and  $Re \sim 560$ –10717, respectively. The maximum values of  $We$  and  $Re$  were calculated at impact velocity of 3.42 m/s and droplet diameter of 5.6 mm, since this was the optimal/highest experimentally

observed combination of both parameters. For each set of tilt angles, the substrate temperature ( $T_{sub}$ ) was varied in the range of  $-25^\circ\text{C}$  to  $-35^\circ\text{C}$  with a step of  $5^\circ\text{C}$ . This thermal range was chosen based on the average air temperatures for altitudes, at which an aircraft could encounter icing clouds and also due to the cooling threshold of the freezer ( $-37^\circ\text{C}$ ). Furthermore, these temperatures are very common in some regions on the earth, which may compromise the performance of cold-region wind turbines. In addition, the relative humidity in the chamber was measured by a DHT 22 humidity sensor and kept close to saturation ( $\sim 100\%$ ) through a tank full with de-ionized water. During the experiments, the impact dynamics of the droplets, as they impinge on the target substrate, was captured by means of a Phantom Miro eX2 high speed camera with a resolution up to 7400 frames/s. The retraction velocity ( $V_{ret}$ ), solid-liquid contact time ( $t_{sl}$ ) and the subsequent freezing time ( $t_{freez}$ ), if ice nucleation occurs, were determined via PCC 2.5 (Phantom Camera Control) commercial computer software.

### 3. Results and discussion

#### 3.1. Morphology and surface adhesion of the carbon soot coatings prior to and after chemical functionalization

Although the surfaces made of carbon soot exhibit extreme water repellency, their anti-icing properties have not been studied yet, as the bonds between the individual nanoparticles are weak, leading to inherent brittleness of the non-modified material and inability of the chimney-modified soot to retain its non-wettability upon harsh operational conditions [31,34,35]. To address these limitation, we have developed a method for chemical functionalization of the soot that enhances its robustness and surface adhesion under harsh operational conditions. Fig. 2 reveals the structure and morphology of the carbon soot, deposited on aluminum (Al) and steel substrates using the chimney method [31], before and after treatment with ethanol and aqueous fluorocarbon solution. It seems that regardless of the chemical functionalization, the soot's amorphous structure composed of tightly bonded and elongated nanoparticles

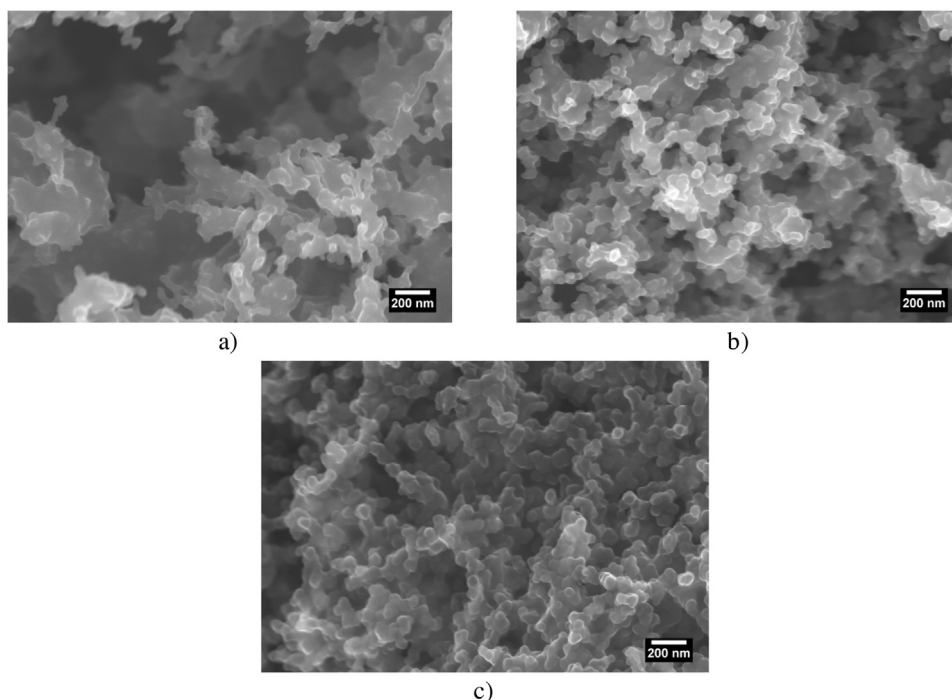


Fig. 2. Scanning electron micrographs of the structure and morphology of the chimney modified carbon soot a) prior to and after treatment with b) ethanol and c) aqueous fluorocarbon solution.

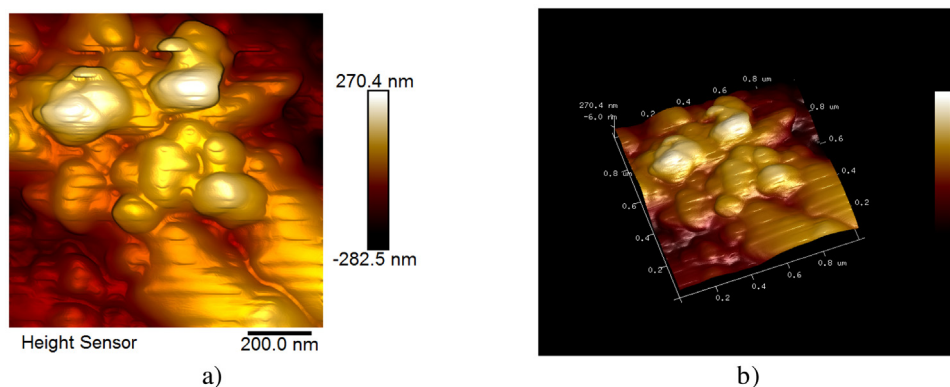


Fig. 3. a) 2-D and b) 3-D AFM images of carbon soot treated with ethanol.

with an average size of  $\sim 60$  nm remains unaltered. Prior to ethanol treatment, the soot coating is extremely water repellent with SCA and CAH being  $\sim 155^\circ$  and  $1^\circ$ , respectively.

However, as seen in Fig. 2b), upon immersion in ethanol, the overall area of micro- and nanoscale cavities decreases significantly. Furthermore, at this stage the surface is characterized with a high SCA of  $155^\circ \pm 2^\circ$ , accompanied by dramatically increased CAH of  $15^\circ \pm 3^\circ$ . These results clearly indicate Cassie-Baxter to Wenzel state transition, where the water droplets still may acquire a spherical shape, but are immobilized and unable to roll-off [32]. To correlate the observed wetting transition with possible changes in the surface topography, we examined the ethanol treated coating by atomic force microscopy, the results of which are shown in Fig. 3. The average root mean square roughness ( $R_{rms}$ ) of the chimney modified soot is around 100 nm [31], while after immersion in ethanol the it decreases to about 80 nm, meaning that the peak features become more rounded, as suggested in ref. [32].

The reduced surface roughness and porosity of the soot imply that the ethanol reacts with the oxygen sites still present in the soot, promoting partial breaking of the existing bonds and leading to denser and well adhered structures. Although the physicochemical nature of these interactions is poorly addressed in the literature, we assume that the enhanced adhesion of the soot could be a consequence of the increased amount of  $sp^3$  bonds in the coating, due to the specific deposition process [31], that along with the reduced porosity strengthen the links between the nanoparticles. In addition, the ethanol increases the total fraction of solid in contact with the water, which accounts for the increased CAH. Subsequent treatment of the surface with fluorocarbon recovers the mobility of water droplets and the CAH decreases to  $0.8^\circ \pm 0.3^\circ$ . Such a phenomenon is associated with the formation of a thin ( $\sim$ nm) hydrophobic layer on top of the soot, as indicated by the presence of  $\sim 4$  at.% fluorine on the surface, depicted in Fig. 4.

A comparison between Fig. 2b) and c) shows that the fluorine-based treatment does not significantly alter the surface topography and only a slight ( $<5$  nm) increase in the particle size is observed. This suggests the formation of a very conformal fluorine-based coating with a thickness of a few nanometers that along with the ( $R_{rms}$ ) of  $\sim 80$  nm reinstates its water repellency. Similar observation has been reported for SU-8 photoresist based patterns immersed in aqueous fluorocarbon solutions [36]. To verify the enhanced surface adhesion of the functionalized soot, and hence its potential to withstand harsh operational conditions, the coatings' integrity and wettability were tested after compressed air scavenging with an air velocity of  $\sim 340$  m/s and spinning at rotational velocities up to 10 000 rpm. In both cases, the coating kept its integrity and superhydrophobic behavior (supporting Figs. S1, S2 and videos S1, S2). The surface adhesion of non-functionalized and

fluorocarbon-modified soot coatings (lack of ethanol) was examined as well, with an aim to clarify whether the ethanol promotes the enhanced adhesion and robustness of the soot. The coatings with no alcohol treatment were easily peeled-off during the air scavenging; thus, indicating that the improved adhesion can be mainly associated with the impact of ethanol (supporting videos S3 and S4). The above experimental observations suggest that the chemically functionalized soot would be capable of withstanding gusty winds and high rotational velocities if intended to serve as protective coating for cold-region wind turbines.

### 3.2. Anti-icing performance of the functionalized soot coatings

After fabrication and functionalization, the anti-icing properties of as prepared soot coated Al and steel substrates were studied in detail. Uncoated Al and steel counterparts were used as a reference in order to assess the differences in droplet dynamics when the surface wettability changes from hydrophilic to superhydrophobic. The impact behavior of icy water droplets was investigated for different Weber and Reynolds numbers at sub-zero substrate temperatures ( $T_{sub}$ ) and  $\sim 100\%$  RH (see Methods for more information). As demonstrated in Fig. 5, for the uncoated sheets, the retraction after spreading is negligible and the maximum spreading diameter of the droplet ( $d_{spread}$ ) is approximately equal to the maximum retraction diameter ( $d_{ret}$ ) regardless of the substrate's tilt angle. This is expected since the hydrophilic substrates, such as Al or steel, ensure large surface area in contact with the liquid. Hence, the viscous forces and the friction at the solid-liquid contact area cause significant energy dissipation that reduces the remaining energy for recoil and the impinged water droplets freeze almost instantly [37].

Fig. 6 shows the relation between the freezing time of icy water droplets and the substrate temperature of uncoated Al and steel wafers.

As seen, the gradual reduction in the substrate temperature accelerates the nucleation and the freezing time ( $t_{freez}$ ) decreases exponentially regardless of the chosen substrate. However, at  $-35^\circ\text{C}$ , the water droplets on bare Al wafer undergo crystal nucleation for  $\sim 0.15$  s, while on the steel they nucleate within  $\sim 1.1$  s, which shows that ( $t_{freez}$ ) depends also on the thermal conductivity of the material. Similar trend of the droplets' freezing time is observed for the entire range of temperatures ( $-25^\circ\text{C}$  to  $-35^\circ\text{C}$ ), which is in good agreement with the classical nucleation theory [38]. In addition, the retraction velocity ( $V_{ret}$ ), determined through the time difference between the maximum spreading and retraction of the water droplet, decreases by reducing the substrate temperature. For an uncoated Al,  $V_{ret} \sim 0.073$ – $0.037$  m/s at  $-25^\circ\text{C}$  and  $-35^\circ\text{C}$ , respectively, while for the steel counterparts is  $\sim 0.16$ –



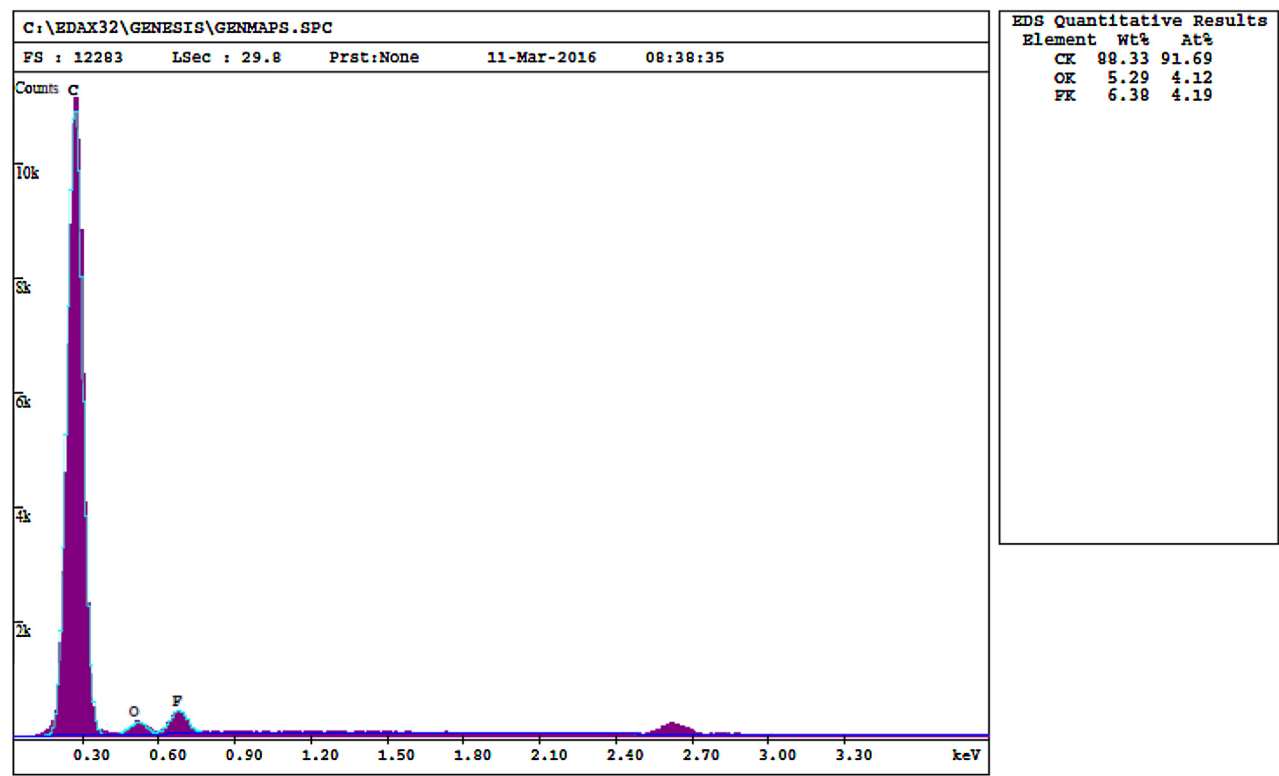


Fig. 4. Chemical composition of the functionalized soot based on EDS measurements.

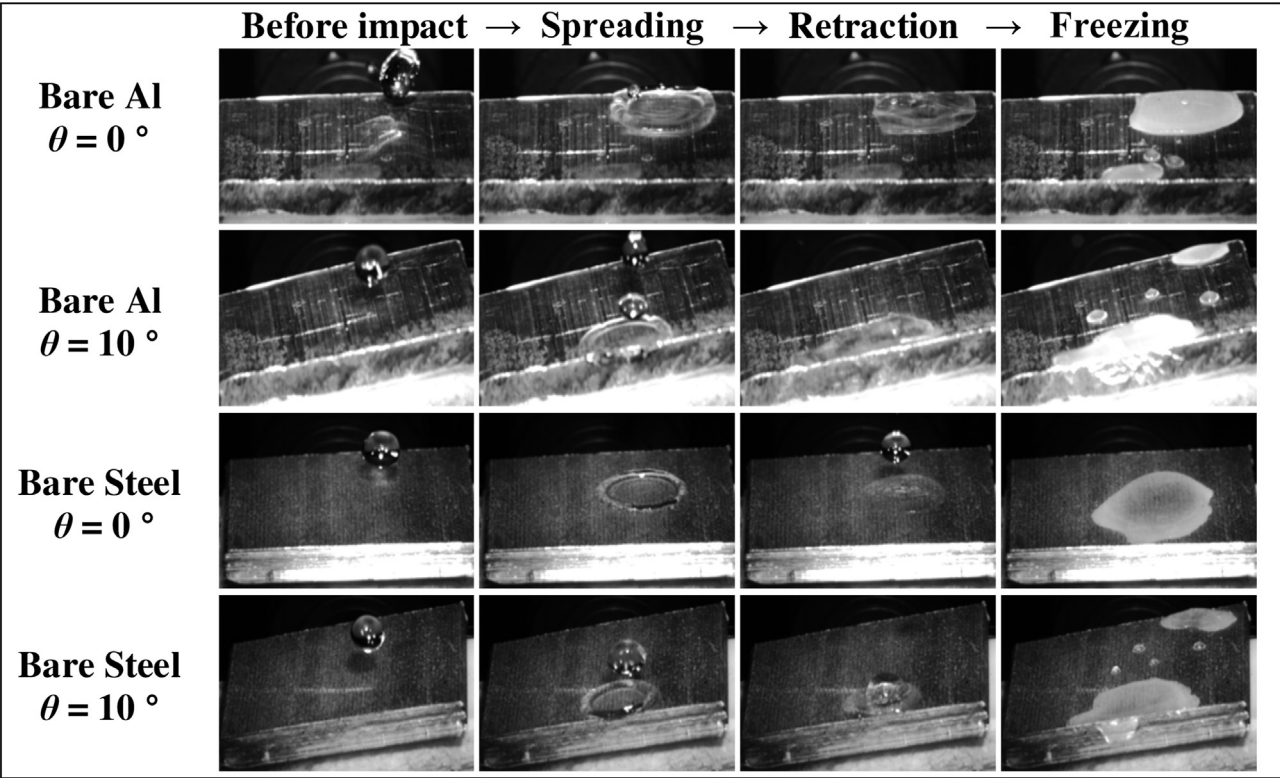
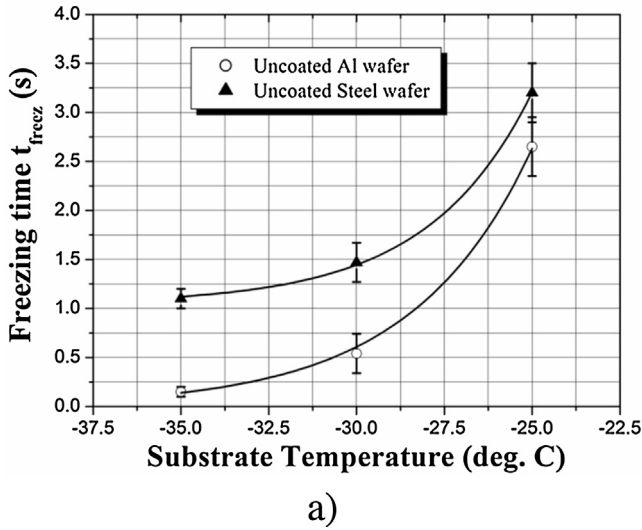


Fig. 5. Impact dynamics of icy water droplets impinging on horizontal and 10° tilted bare Al and steel substrates from a 70 mm height at  $T_{sub} = -35^\circ\text{C}$  and RH ~100%. The images are taken at 500  $\mu\text{s}$  frame time and  $We \sim 16\text{--}80$ ,  $Re \sim 698\text{--}2636$ .

0.055 m/s in the same thermal range. This effect is attributed to the increased losses of kinetic energy, resulting from the increased viscous shear and dissipation at the three-phase contact line [14].

In contrast, the droplet dynamics on soot coated super-hydrophobic surfaces changes drastically. Complete retraction ( $d_{ret} = 0$ ) followed by droplet rebound and/or splashing occurs in



**Fig. 6.** Freezing time of icy water droplets as a function of the substrate temperature. The data plots are an average value of four independent measurements at tilt angles in the range of 0–50°. The solid lines represent the best fit curves of the experimental data.

the entire range of temperatures independent on the tilt angle of the substrate, as illustrated in Fig. 7. This complicated dynamic behavior of the droplets is guided by the competition between their inertial and capillary forces [39]. For the calculated Weber and Reynolds numbers ranging within  $We \sim 14$ –27 and  $Re \sim 560$ –1120, respectively, the droplets retract under the action of capillary forces, which tend to minimize the contact with the surface [39,40]. Since on superhydrophobic surfaces, in particular soot coated ones, the droplets behave as if on a frictionless surface [14]; their kinetic energy at impact is transformed into a surface energy, causing sub-

sequent bounce-off [20]. As a result, the solid-liquid contact time is reduced to a few milliseconds ( $t_{sl} = 3$ –20 ms) and for the chosen range of substrate temperatures, the droplets shed-off before nucleation takes place.

Beyond the above mentioned values of  $We$  and  $Re$ , the initial kinetic energy is enough to overcome the capillary forces, which are unable to keep the integrity of the liquid on the surface and droplet splashing occurs. During the retraction phase, the droplets disintegrate into smaller satellites that jetting out from the outermost perimeter [39]. Despite that, the impacted surfaces remain completely free of ice in the entire range of substrate temperatures, demonstrating clearly the anti-icing properties of the chemically functionalized carbon soot coatings. Moreover, the soot retains ice-phobicity during the entire stage of icing experiments (12 cycles for Al and steel), confirming its strong potential for utilization in passive anti-icing systems.

### 3.3. Verification of the icing experiments with the kinetic model for three-dimensional heterogeneous nucleation

The remarkable icephobic behavior of the functionalized soot coatings can be explained through the kinetic model for three-dimensional heterogeneous nucleation used to explain the effect of the critical particle size of various composites on their icephobic properties [24,41]. According to this model, the kinetics of homogeneous nucleation is described by the nucleation rate ( $J$ ), defined as the number of nuclei created per unit volume for a specific time ( $t$ ). This rate ( $J$ ) depends on the thermodynamic free energy barrier ( $\Delta G_n^{homo}$ ) and when the ice embryo formation occurs on solid surface i.e. heterogeneous nucleation, the energy barrier is reduced by a factor ( $f$ ) ranging from 1 to 0:

$$\Delta G_n = \Delta G_n^{homo} f(m, x) \quad (1),$$

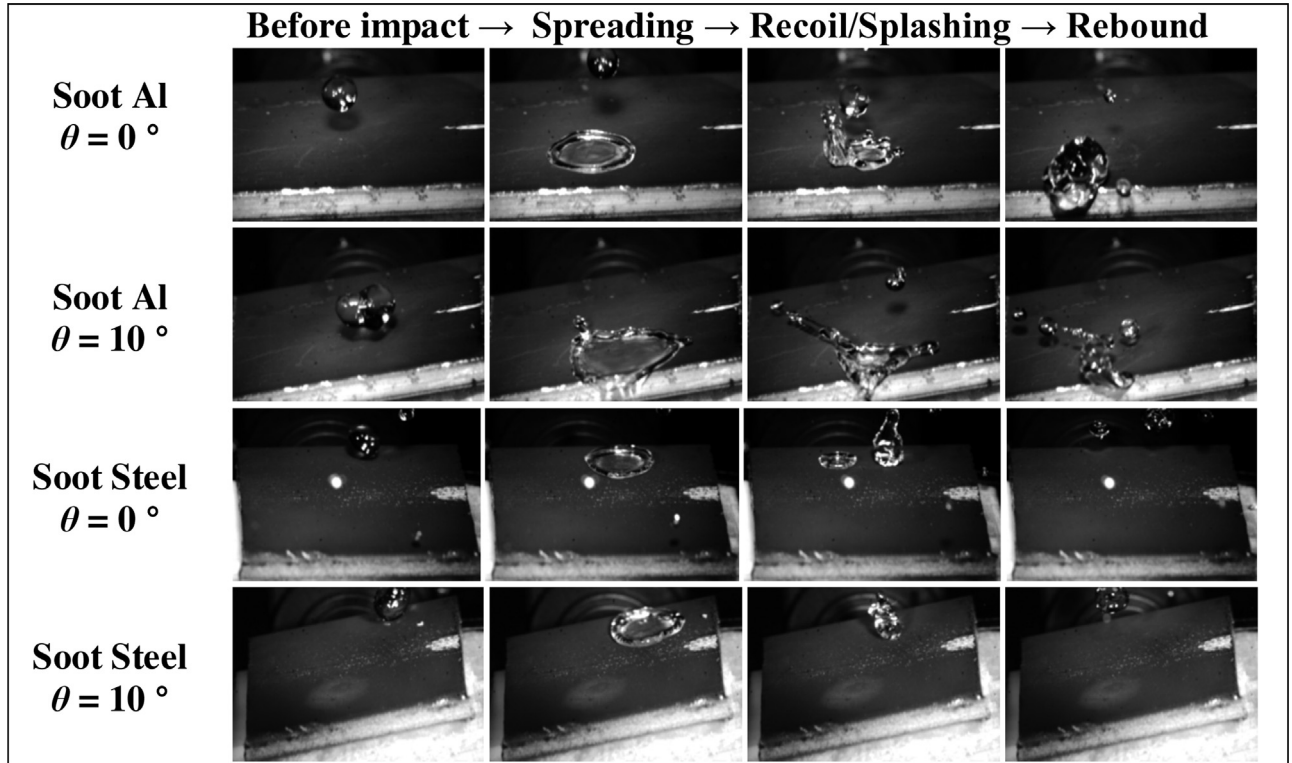


**Fig. 7.** Impact dynamics of icy water droplets impinging on horizontal and 10° tilted soot coated Al and steel substrates from a 70 mm height at  $T_{\text{sub}} = -30^\circ\text{C}$  and  $RH \sim 100\%$ . The images are taken at 500  $\mu\text{s}$  frame time and  $We \sim 14$ –213,  $Re \sim 560$ –5404.

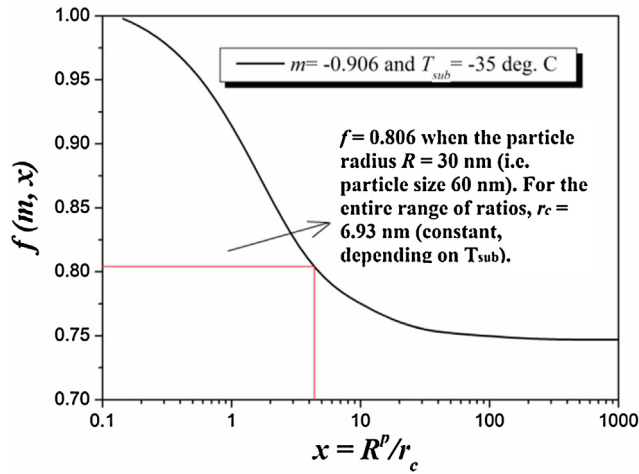


**Fig. 8.** Alteration of the reduction factor ( $f$ ) as a function of the relative particle size ( $x$ ) at  $T_{sub} = -35^\circ\text{C}$  and  $\theta = 155^\circ$  ( $m = -0.906$ ).

where

$$f(m, x) = \frac{1}{2} + \frac{1}{2} \left( \frac{1 - mx}{w} \right)^3 + \frac{1}{2} x^3 \left[ 2 - 3 \left( \frac{x - m}{w} \right) + \left( \frac{x - m}{w} \right)^3 \right] + \frac{3}{2} mx^2 \left( \frac{x - m}{w} - 1 \right) \quad (2)$$

In Eq. (2), the parameters ( $m$ ), ( $x$ ) and ( $w$ ) are used to account the influence of the surface properties on the reduction factor ( $f$ ):

$$m = \cos\theta = \left( \frac{\gamma_{sv} - \gamma_{sl}}{\gamma_{lv}} \right) \quad (3)$$

$$x = \frac{R^p}{r_c} \quad (4)$$

$$w = \sqrt{(1 + x^2 - 2xm)} \quad (5)$$

Eq. (3) expresses the equilibrium contact angle  $\theta$ , providing  $-1 \leq m \leq 1$ , which determines the wettability of the solid surface. On the other hand, ( $x$ ) is a dimensionless parameter that presents the ratio of the radius of a spherical solid particle ( $R^p$ ), around which the ice embryo forms, towards those of the critical ice embryo ( $r_c$ ) (the minimum size that an incipient ice crystal needs to acquire to trigger freezing [25]). The latter is obtained as a function of the water-ice interfacial tension ( $\gamma$ ), water molar volume ( $v$ ), water heat capacity ( $C_p$ ), ice melting temperature ( $T_m$ ) and the substrate temperature ( $T_{sub}$ ), as shown by Cao et al. [24]. Adapting their approach to our experimental conditions ( $T_{sub} = -35^\circ\text{C}$ ),  $r_c$  was calculated to be 6.93 nm.

Fig. 8 represents the calculated alteration of the reduction factor ( $f$ ) as a function of ( $x$ ) at particular substrate temperature ( $T_{sub}$ ) and water contact angle ( $\theta$  is expressed through  $m$ ), similarly as in Refs. [24,28,41].

The exponential decay of ( $f$ ) indicates that the free energy barrier for heterogeneous nucleation ( $\Delta G_n$ ) decreases when the relative particle size ( $x$ ) increases. At the upper extreme value of  $f=1$ ,  $\Delta G_n$  equals  $\Delta G_n^{homo}$  and the nucleation rate ( $J$ ) is low, while at  $f=0$  the energy barrier vanishes and nucleation should occur instantly (see Eq. (1)). In our case, the average size of the functionalized soot particles is  $\sim 60$  nm, which corresponds to  $f=0.806$ . Therefore, at substrate temperatures of  $-35^\circ\text{C}$ , the reduction in the nucleation barrier with less than 20% and the decreased solid-liquid contact time  $t_{sl} = 3\text{--}20$  ms are insufficient to initiate ice nucleation. These observations are in good agreement with the experimental results

reported from Cao et al., where it is shown that the icing probability is relatively low at particles' size up to  $\sim 100$  nm [24].

### 3.4. Control experiments

Considering the possible practical applicability of our coatings, further experiments simulating harsh operational conditions were performed. Since the cold-region wind turbines are designed to operate continuously, the daily thermal drifts may cause condensation of water vapor on the substrate and subsequent loss of icephobicity [1,26]. Fig. S3 in the supporting information represents the impact dynamics of icy water droplets on horizontal soot coated Al sheet placed in a condensate environment (RH  $\sim 100\%$ ), when the ambient temperature is gradually decreased over time from  $+21^\circ\text{C}$  to  $-35^\circ\text{C}$  with a cooling rate of  $\sim 10^\circ\text{C/h}$ . Even in such an extreme case, where the ambient temperature changes drastically within a few hours, the functionalized carbon soot prevents the ice formation. The spreading and recoiling regimes take place within  $\sim 14$  ms, which inhibits the ice nucleation. Interestingly, the bouncing ability of the impinging droplets is lowered and they coalesce into bigger water droplet, which then shed-off the surface by sliding instead of rebounding. This observation might be ascribed to the mass of the liquid and the low impact velocity of 1 m/s, which can reduce the restitution coefficient of the droplet and suppress its bouncing [20]. However it may also be attributed to the frost formation on the surface, triggered by the condensation of water vapor upon reduction of the substrate temperature. The frost forms inevitably on any surface, whose temperature is below the dew point [42]; however, at 100% relative humidity the ambient temperature and dew point temperature match. Since we gradually decreased the ambient temperature when the air was saturated with water vapor, it was expected that the vapor may condense on the substrate. Indeed, the inner walls, as well as the shelves of the icing chamber were covered with frost, while on eye inspection the soot seemed to be unaffected and the icy droplets were successfully suspended after impact. One possible explanation is that the air has been cooled down faster than the superhydrophobic surface, which prevents the condensation of water vapor on the soot. However, the heat capacity of the Al alloy (6061) is higher than that of air ( $C_{vair} = 0.716$  kJ/kgK;  $C_{vAl6061} = 0.896$  kJ/kgK at  $T = 300$  K), implying that the Al substrate will decrease its temperature with a higher rate than the air. Another reason could be related with the low conduction of heat through the air, which in turn would increase the time needed for cooling of the soot coated Al sheet. However, such a hypothesis seems unlikely, since if this was true, then the inner walls and shelves of the chamber would also be free of frost. Apparently, that is not the case and the frosted shelves and inner walls of the chamber suggest that the metal surfaces, perhaps the soot coated Al substrate as well, have been cooled below the dew point temperature. Thus, in such a medium, the water vapor preferentially condensate on the hydrophilic (the shelves and walls) surfaces rather than the superhydrophobic ones (the soot coated Al), since the nucleation free energy barrier decreases significantly by switching the surface wettability from superhydrophobic to hydrophilic [2]. In fact, it has quantitatively been demonstrated that a soot coated quartz substrate adsorbs  $\sim 7$  times lower amount of water vapor compared to its uncoated counterpart [43]. Up to now, there is no unambiguous explanation of the soot's water vapor repellency; therefore, we can only speculate for the inhibited frost formation, assuming that the soot's immiscibility in water and its nanoscale surface topography are the primary reasons for that phenomenon [2,44]. Other scenario may consider the formation of spherical condensates on the superhydrophobic surface that are capable of spontaneous jumping off before initiation of freezing, as reported by Boreyko et al. for different chemical micropatterns [16,42].



Finally, we investigated the icephobicity of the functionalized coating upon frosting (large and instant thermal drifts causing condensation), as well as its mechanical durability under water jetting with velocity of  $\sim 25$  m/s. Soot coated steel substrate ( $25 \times 25$  mm), cooled down in the icing chamber to  $-30^\circ\text{C}$ , was exposed to room temperature water vapor for 30 s ( $T \sim 22^\circ\text{C}$ ) and then again mounted in the test chamber. Although such an instant thermal drift (change in the ambient temperature from  $-30^\circ\text{C}$  to  $+22^\circ\text{C}$  within seconds) is not common in “real-world” conditions, it is an excellent benchmark for evaluation of the materials’ icephobicity upon frosting [1,16,42]. After exposure to room temperature, the entire soot surface covered with frost instantly and afterwards the icephobicity of the sample was tested again. Expectedly, the impinging water droplets turned into ice; however, they froze in a spherical shape. This might be caused by the air trapped within the surface protrusions, which reduces the actual solid-liquid surface area, allowing retention of the suspended Cassie-Baxter state even upon nucleation [14,15,42]. Furthermore, small amount of thermal energy and slight tilting of the sample ( $T_{\text{sub}} = \sim -10^\circ\text{C}$ ,  $\theta \sim 30^\circ$ ) were enough to promote sliding of the entire piece of ice (Fig. S4 in the supporting information). The  $T_{\text{sub}}$ , at which sliding occurred, was measured with a Kintrex IRT0421 infrared thermal sensor, whose measurement accuracy was verified by determining the ambient and human body temperatures. In both cases the measurement accuracy was within  $\pm 1^\circ\text{C}$ . The ice was removed without any loss of integrity, while on bare Al or steel substrates it detached after complete melting. This implies low ice adhesion on the functionalized soot due to stress concentrations arisen from the air gaps in the coating and the reduced solid-liquid contact area, which further disrupt the ice bonds [11,16]. As a secondary effect, after the ice removal and subsequent increase in the substrate temperature above  $0^\circ\text{C}$ , the frost was transformed into small spherical liquid droplets that then slid-off the surface. The dynamic removal of the melted frost may be a consequence of spontaneous dewetting followed by gravitational mobilization, as firstly shown by Boreyko et al. [45]. The authors explain this dynamic defrosting by the energetically driven minimization of the liquid’s surface energy, which is physically enabled by the suspended Cassie-Baxter state of the surface [45]. Later, the soot coated steel substrate was heated up to room temperature and exposed for 5 s under water jetting with velocity of  $\sim 25$  m/s. Even after such a reckless treatment, the central part of the surface remained hydrophobic, while the edges were still water repellent (supporting video S5). Moreover, a secondary treatment with fluorocarbon solution recovered the superhydrophobicity of more than 80% of the surface area, revealing that the chemical functionalization can substantially lengthen the lifetime of the coating (supporting video S6). For the sake of completeness, we investigated the durability of non-functionalized and fluorocarbon-modified soot samples (no ethanol treatment) under the same water jet (supporting videos S7, S8). After termination of the experiments, both types of coatings were completely destroyed and the surfaces exhibited hydrophilicity. Based on these comparative results, we presume that the functionalized soot would be able to resist the impact of heavy rains, which may occur during the operation of wind turbines.

#### 4. Conclusions

This paper presented systematic experimental investigations on the icephobic properties of carbon soot coated Al and steel substrates. The inherent brittleness of the soot was circumvented by a secondary chemical treatment with ethanol and fluorocarbon solution. We found that the functionalized coatings exhibit enhanced mechanical strength and surface adhesion under compressed air scavenging, spinning and water jetting, which has important impli-

cations for their practical applicability. Also, the as prepared soot surfaces remained free of ice in the entire range of substrate temperatures at various impact dynamics scenarios. Our experiments correlated well with the kinetic model for three-dimensional heterogeneous nucleation and revealed that the average soot particle size falls into the length scale of icephobicity. In addition, upon frosting of the soot, the icy droplets nucleated in a ball-up shape and were easily removed using negligible amount of thermal energy. This implied reduced ice adhesion on the functionalized soot, attributed to the weakening and disruption of the ice bonds caused by the air trapped within the surface. Moreover, upon frosting and subsequent thermal heating above the freezing temperature, the soot coating was dynamically defrosted, which is of particular interest for a variety of systems in condensate environments. Last but not least, the high fabrication scalability of our approach, along with the enhanced durability of the soot coating, may further advance and facilitate the development of long lasting and inexpensive icephobic surfaces, which is of utmost importance for their industrial applicability. Achieving this goal goes through elucidation of the soot’s frosting/defrosting mechanism, its water vapor repellency at certain circumstances and the physicochemical nature of the soot-ethanol interactions, which is planned as a future work. Although the prevention of atmospheric icing is a complex and non-trivial task, we believe that the results of this study are fundamental for the significant extension and enrichment of the current strategies for passive icing protection.

#### Acknowledgments

The authors wish to acknowledge the VCU’s Nanomaterials Core Characterization Facility for providing access to the surface characterization equipment. Also, the startup support from Virginia Commonwealth University under grant 137422 is greatly acknowledged. Dr. Esmerlyan wishes to gratefully acknowledge Prof. Neil Shirtcliffe from Rhine-Waal University of Applied Sciences for his comments about the chemistry of Grangers Performance Proofer and fruitful discussions.

#### Appendix A. Supplementary data

Supplementary data associated with this article can be found, in the online version, at <http://dx.doi.org/10.1016/j.apsusc.2016.08.101>.

#### References

- [1] S. Farhadi, M. Farzaneh, S.A. Kulinich, Anti-icing performance of superhydrophobic surfaces, *Appl. Surf. Sci.* 257 (2011) 6264–6269.
- [2] R.P. Sear, Nucleation: theory and applications to protein solutions and colloidal suspensions, *J. Phys. Condens. Matter* 19 (2007) 033101.
- [3] E.B. Moore, V. Molinero, Structural transformation in supercooled water controls the crystallization rate of ice, *Nature* 479 (2011) 506–508.
- [4] C.R. Sullivan, V.F. Petrenko, J.D. McCurdy, V. Kozliouk, Breaking the ice: de-icing power transmission lines with high-frequency high-voltage excitation, *IEEE Ind. Appl. Mag.* 9 (2003) 49–54.
- [5] Y.H. Yeong, R. Mudafort, A. Steele, I. Bayer, E. Loth, Water droplet impact dynamics at icing conditions with and without superhydrophobicity, *AIAA Paper* 3134 (2012) 1–14.
- [6] A.M. Palacios, J.L. Palacios, L. Sánchez, Eliciting a human understandable model of ice adhesion strength for rotor blade leading edge materials from uncertain experimental data, *Expert Syst. Appl.* 39 (2012) 10212–10225.
- [7] R.W. Gent, N.P. Dart, J.T. Cansdale, Aircraft icing, *Philos. Trans. R Soc. A* 358 (2000) 2873–2911.
- [8] P. Appiah-Kubi, US Inflight Icing Accidents and Incidents 2006–2010, Master’s Thesis, University of Tennessee, 2011.
- [9] N. Dalili, A. Edrissy, R. Cariveau, A review of surface engineering issues critical to wind turbine performance, *Renew. Sustain. Energy Rev.* 13 (2009) 428–438.
- [10] O. Parent, A. Ilinca, Anti-icing and de-icing techniques for wind turbines: critical review, *Cold Reg. Sci. Tech.* 65 (2011) 88–96.

- [11] S. Tarquini, C. Antonini, A. Amirfazli, M. Marengo, J. Palacios, Investigation of ice shedding properties of superhydrophobic coatings on helicopter blades, *Cold Reg. Sci. Tech.* 100 (2014) 50–58.
- [12] S. Ramanathan, V.V. Varadhan, V.K. Varadhan, De-Icing of Helicopter Blades Using Piezoelectric Actuators, *Smart Structures and Materials 2000: Smart Electronics and MEMS*, SPIE Publishing, Seattle, WA, 2002, pp. 354–363.
- [13] J. Palacios, E. Smith, J. Rose, R. Royer, Ultrasonic de-icing of wind-tunnel impact icing, *J. Aircraft* 48 (2011) 1020–1027.
- [14] L. Mishchenko, B. Hatton, V. Bahadur, J.A. Taylor, T. Krupenkin, J. Aizenberg, Design of ice-free nanostructured surfaces based on repulsion of impacting water droplets, *ACS Nano* 4 (2010) 7699–7707.
- [15] S. Jung, M. Dorrestijn, D. Raps, A. Das, C.M. Megaridis, D. Poulikakos, Are superhydrophobic surfaces best for icephobicity? *Langmuir* 27 (2011) 3059–3066.
- [16] J.B. Boreyko, C.P. Collier, Delayed frost growth on jumping-drop superhydrophobic surfaces, *ACS Nano* 7 (2013) 1618–1627.
- [17] M. Zou, S. Beckford, R. Wei, C. Ellis, G. Hatton, M.A. Miller, Effects of surface roughness and energy on ice adhesion strength, *Appl. Surf. Sci.* 257 (2011) 3786–3792.
- [18] V. Hejazi, K. Sobolev, M. Nosonovsky, From superhydrophobicity to icephobicity: forces and interaction analysis, *Sci. Rep.* 3 (2013) 02194.
- [19] C. Antonini, M. Innocenti, T. Horn, M. Marengo, A. Amirfazli, Understanding the effect of superhydrophobic coatings on energy reduction in anti-icing systems, *Cold Reg. Sci. Tech.* 67 (2011) 58–67.
- [20] D. Richard, D. Quere, Bouncing water drops, *Europhys. Lett.* 50 (2000) 769–775.
- [21] A. Alizadeh, M. Yamada, R. Li, W. Shang, S. Otta, et al., Dynamics of ice nucleation on water repellent surfaces, *Langmuir* 28 (2012) 3180–3186.
- [22] P. Tourkine, M.L. Merrer, D. Quere, Delayed freezing on water repellent materials, *Langmuir* 25 (2009) 7214–7216.
- [23] P. Guo, Y. Zheng, M. Wen, C. Song, Y. Lin, L. Jiang, Icephobic/anti-icing properties of micro/nanostructured surfaces, *Adv. Mater.* 24 (2012) 2642–2648.
- [24] L. Cao, A.K. Jones, V.K. Sikka, J. Wu, D. Gao, Anti-icing superhydrophobic coatings, *Langmuir* 25 (2009) 12444–12448.
- [25] M. Nosonovsky, V. Hejazi, Why superhydrophobic surfaces are not always icephobic, *ACS Nano* 6 (2012) 8488–8491.
- [26] S. Jung, M.K. Tiwari, N.V. Doan, D. Poulikakos, Mechanism of supercooled droplet freezing on surfaces, *Nat. Commun.* 3 (2012) 615.
- [27] S.A. Kulnich, M. Farzaneh, How wetting hysteresis influences ice adhesion strength on superhydrophobic surfaces, *Langmuir* 25 (2009) 8854–8856.
- [28] T.M. Schutzius, S. Jung, T. Maitra, P. Eberle, C. Antonini, C. Stamatopoulos, D. Poulikakos, Physics of icing and rational design of surfaces with extraordinary icephobicity, *Langmuir* 31 (2015) 4807–4821.
- [29] T. Verho, C. Bower, P. Andrew, S. Franssila, O. Ikkala, R.H.A. Has, Mechanically durable superhydrophobic surfaces, *Adv. Mater.* 23 (2011) 673–678.
- [30] A. Milionis, E. Loth, I.S. Bayer, Recent advances in the mechanical durability of superhydrophobic materials, *Adv. Colloid Interface Sci.* 229 (2016) 57–79.
- [31] K.D. Esmeryan, C.E. Castano, A.H. Bressler, M. Abolghasemibizaki, R. Mohammadi, Rapid synthesis of inherently robust and stable superhydrophobic carbon soot coatings, *Appl. Surf. Sci.* 369 (2016) 341–347.
- [32] K.D. Esmeryan, G. McHale, C.L. Trabi, N.R. Gerdali, M.I. Newton, Manipulated wettability of a superhydrophobic quartz crystal microbalance through electrowetting, *J. Phys. D: Appl. Phys.* 46 (2013) 345307.
- [33] N.J. Shirtcliffe, private communication May 2016.
- [34] X. Deng, L. Mammen, H.J. Butt, D. Volmer, Candle soot as a template for a transparent robust superamphiphobic coating, *Science* 335 (2012) 67–70.
- [35] K.D. Esmeryan, E.I. Radeva, I.D. Avramov, Durable superhydrophobic carbon soot coatings for sensor applications, *J. Phys. D Appl. Phys.* 49 (2016) 025309.
- [36] N.J. Shirtcliffe, S. Aqil, C. Evans, G. McHale, M.I. Newton, C.C. Perry, P. Roach, The use of high aspect ratio photoresist (SU-8) for super-hydrophobic pattern prototyping, *J. Micromech. Microeng.* 14 (2004) 1384–1389.
- [37] A. Alizadeh, V. Bahadur, S. Zhong, W. Shang, R. Li, J. Ruud, M. Yamada, L. Ge, A. Dhinojwala, M. Sohal, Temperature dependent droplet impact dynamics on flat and textured surfaces, *Appl. Phys. Lett.* 100 (2012) 111601.
- [38] L.H. Seeley, G.T. Seidler, Two-dimensional nucleation of ice from supercooled water, *Phys. Rev. Lett.* 87 (2001) 055702.
- [39] V. Bertola, Drop impact on a hot surface: effect of a polymer additive, *Exp. Fluids* 37 (2004) 653–664.
- [40] V. Bergeron, D. Bonn, J.Y. Martin, L. Vovelle, Controlling droplet deposition, *Nature* 405 (2000) 772–775.
- [41] X.Y. Liu, A new kinetic model for three-dimensional heterogeneous nucleation, *J. Chem. Phys.* 111 (1999) 1628–1635.
- [42] J.B. Boreyko, R.R. Hansen, K.R. Murphy, S. Nath, S.T. Retterer, C.P. Collier, Controlling condensation and frost growth with chemical micropatterns, *Sci. Rep.* 6 (2016) 19131.
- [43] K.D. Esmeryan, T.A. Yordanov, L.G. Vergov, Z.G. Raicheva, E.I. Radeva, Humidity tolerant organic vapor detection using a superhydrophobic quartz crystal microbalance, *IEEE Sens. J.* 15 (2015) 6318–6325.
- [44] S. Henning, M. Ziese, A. Kiselev, H. Saathoff, O. Möhler, T.F. Mentel, A. Buchholz, C. Spindler, V. Michaud, M. Monier, K. Sellegri, F. Stratmann, Hygroscopic growth and droplet activation of soot particles: uncoated succinic or sulfuric acid coated, *Atmos. Chem. Phys.* 12 (2012) 4525–4537.
- [45] J.B. Boreyko, B.R. Srijanto, T.D. Nguyen, C. Vega, M.F. Cabrera, C.P. Collier, Dynamic defrosting on nanostructured superhydrophobic surfaces, *Langmuir* 29 (2013) 9516–9524.



# Kinetically driven graphite-like to diamond-like carbon transformation in low temperature laminar diffusion flames

Karekin D. Esmeryan<sup>a,b</sup>, Carlos E. Castano<sup>c</sup>, Ashton H. Bressler<sup>a</sup>, Mehran Abolghasemibizaki<sup>a</sup>, Christian P. Fergusson<sup>a</sup>, Allan Roberts<sup>a</sup>, Reza Mohammadi<sup>a,\*</sup>

<sup>a</sup> Department of Mechanical and Nuclear Engineering, Virginia Commonwealth University, Richmond, VA 23284, USA

<sup>b</sup> Georgi Nadjakov Institute of Solid State Physics, 72, Tzarigradsko Chaussee Blvd., 1784 Sofia, Bulgaria

<sup>c</sup> Nanomaterials Core Characterization Facility, Department of Chemical and Life Science Engineering, Virginia Commonwealth University, Richmond, VA 23284, USA

## ARTICLE INFO

### Article history:

Received 7 November 2016

Received in revised form 18 January 2017

Accepted 20 January 2017

Available online 21 January 2017

### Keywords:

Carbon nanoparticles

Diamond-like carbon

Laminar diffusion flames

Rapeseed oil

Reaction kinetics

Soot

## ABSTRACT

Historically, the synthesis of diamond and graphite via combustion flames stands out as a simplified, scalable and inexpensive approach. Unfortunately, this method is not beneficial for industrial applications in coatings due to limitations related with the high flame and substrate temperatures. Here, we report novel findings about the formation mechanism of graphite-like and diamond-like supported nanostructures in low temperature laminar diffusion flames. Both materials are formed upon controllable combustion at atmospheric pressure of a cylindrical paper wick immersed in rapeseed oil. An accurate adjustment of the incident air flow and the amount of available fuel allow deposition of carbon soot or diamond-like carbon (DLC). The DLC formation is favorable in a narrow stoichiometric range at flame temperatures within ~210–260 °C and beyond this range the particles precipitate as soot. The comparative structural analysis using scanning electron microscopy, Raman spectroscopy, X-ray photoelectron spectroscopy and transmission electron microscopy, along with the full thermal and stoichiometric profiles for the chosen combustion conditions, suggest a kinetically driven graphite-to-diamond transformation rather than a thermodynamically induced phase transition. Our results reveal a new direction in the principles of graphite and diamond formation in flames that could be applied to surmount the existing shortcomings in flame synthesis.

© 2017 Elsevier B.V. All rights reserved.

## 1. Introduction

The life in its present form would be impossible without the participation of carbon, as it is a common chemical element that provides the building blocks of various drugs, pesticides and dyes [1]. The structural diversity of carbon is unrivaled in the periodic table, but regardless of the tremendous research activities on the other allotropic forms, including fullerenes and carbon nanotubes, so far, diamond and graphite remain the most industrially exploited carbon allotropes [2].

Among the well known methods for synthesis of diamond and graphite, such as detonation of carbon-based explosives [3], plasma-enhanced chemical vapor deposition [4], pulsed laser deposition [5,6], ion beam/magnetron sputtering [7–9], etc., the combustion flame synthesis at atmospheric pressure offers overwhelming simplicity and several advantages [10–14]. For instance, the chemically reactive environment

of the flame ensures high deposition rates of over 0.028 μm/s and ~1.5–2 μm/s for diamond-like and graphite-like nanostructures, respectively, within a single-step process [15,16]. Also, the method is scalable and has a potential for a large-volume continuous production at low cost [13]. Furthermore, in terms of the diamond deposition, the combustion method can produce high-quality diamond, since the atmospheric oxygen etches the graphitic impurities very efficiently [15]. In addition, the combustion systems are highly convective and any changes in the oxygen-fuel ratio, fuel composition and/or the deposition conditions allow an accurate and fast adjustment of the physical properties of diamond coatings [15,17].

Although the combustion flame technique is a versatile tool, its applicability is more laboratory than industrially oriented. One of the important technological constraints is related to the high flame temperature (~600 °C up to ~3000 °C, depending on the material burned and flame type [18]) that hinders the practical usability of substrates with low thermal sustainability. Another disadvantage is that the flame, either laminar or turbulent, could induce large radial inhomogeneity in the growth rate, surface morphology or the quality of the layers [19]. Also, the formation mechanism of carbon nanoparticles and their

\* Corresponding author.

E-mail address: [rmohammadi@vcu.edu](mailto:rmohammadi@vcu.edu) (R. Mohammadi).

dynamics during the fuel combustion are not completely clarified [20], which also impedes the successful industrial adoption of the flame method.

Substantial progress in regard to the fundamentals of carbonaceous nanoparticles formation in various flames has been achieved in the past two decades [21–28]. Theoretical models based on the chemical kinetics of the incipient particles have been used to determine the particles size distribution in laminar premixed flames, as well as the onset of the transition from coalescent to aggregate particle growth [21–23]. Thereby, important insights about the internal structure and dynamics of the incipient carbon particles, along with their clustering at high temperatures have been provided [24–26]. It has been designated that the gas-phase chemistry, flame temperature, and the burner-to-substrate distance are critical for the morphology and structure of diamond and graphite nanomaterials [21, 23, 27, 28]. Thus, many features of the gas-phase dynamics seem quite well understood, although it is still relatively hard to define the exact reaction mechanisms [28]. Further progress towards the enrichment of the state-of-the-art in flame synthesis has recently been achieved by our research group. We have developed a novel chimney-based combustion method that overcomes the technological constraints of the high flame temperature and promotes the deposition of carbon nanostructures with an adjustable fraction of graphitic-like and diamond-like phases [29]. Surprisingly, in the conditions of low temperatures ( $T_{\text{flame}} \sim 270^\circ\text{C}$ ) we have observed graphite-to-diamond transformation triggered without additional catalysts or reagents (only rapeseed oil has been used as a hydrocarbon precursor). Also, relatively uniform carbon films have been deposited across the substrate, especially for the graphite-like coatings (soot), with slight  $\pm 7.5\%$  film thickness deviations [29].

However, in the absence of a catalyst, the direct graphite-to-diamond transformation is associated with high pressures and/or temperatures due to the separation of two phases by a high energy barrier ( $\sim 0.4$  eV per atom), despite of their comparable free energies ( $\sim 0.02$  eV difference per atom) [30, 31]. Furthermore, since graphite is the stable form of carbon at ambient pressures, the formation of diamond from carbon-rich fuels requires high flame and substrate temperatures that will provide the thermal energy needed for activation of the gas species [10–12, 15, 17]. Therefore, the observed phase transition at low flame temperatures is questionable and highly unlikely from a thermodynamic point-of-view [30, 31]. In contrary to that concept, recent experiments have shown the presence of four well known allotropic forms of carbon in a candle flame, namely diamond, graphite, fullerenes and amorphous carbon [32, 33]. Moreover, in an odd research, the incomplete combustion of naphthalene has lead to local alteration of the interlayer spacing between the concentric shells of carbon onions from 0.34 nm (graphite-like) to 0.29 nm (diamond-like) [34]. Similar result has also been reported for carbon nanoparticles generated from the flame of paraffin oil, where some of the lattice spacings are ascribed to diamond-like carbon [35]. These findings, along with the recently proposed non-equilibrium route to diamond formation [36], suggest that the catalyst-free graphite-to-diamond transition at low flame temperatures might not be an artifact. Unfortunately, there is a profound lack of follow-up research articles that at least can partially enlighten on the mechanism of diamond formation in the case of low temperature combustion flames.

The primary objective of this paper is to provide new insights about the nature of nascency of diamond in low temperature laminar diffusion flames. Based on an enhanced combustion system with an accurate air flow control, we demonstrate that the diamond deposition from the incomplete combustion of rapeseed oil is favorable in a narrow stoichiometric range at flame temperatures within  $\sim 210$ – $260^\circ\text{C}$ . These observations suggest a kinetically driven graphite-to-diamond transformation rather than a thermodynamically induced phase transition.

## 2. Experimental

### 2.1. Detailed description of the combustion system

The most recent model of our combustion system with a precise air flow control is depicted in Fig. 1. An Intex Quick-Fill 12v-DC electric air pump is powered by an Antec BP550 PLUS modular power supply and used to provide the atmospheric oxygen required for the combustion process. The air pushed by the pump flows through  $\sim 70$  cm long tubing with an internal diameter (ID) of  $\sim 1$  cm before reaching a controllable gas flow meter (McMaster Carr 5079K25). The latter ensures an adjustable air flow within  $0.0014$ – $0.0052$   $\text{m}^3/\text{min}$  that reaches an inverted tin funnel (McMaster Carr 8996T12) connected to the flow meter via an additional  $\sim 20$  cm long aluminum pipe with an ID  $\sim 1.1$  cm and  $\sim 50$  cm of tubing. The metal pipe is sealed to the funnel by using high temperature stove cement (McMaster Carr 7573A31, RUTLAND brand) and a ring stand supports that configuration by clamping to the aluminum tube.

During the experiments, a cylindrical-shaped paper wick was immersed in a Pyrex dish containing rapeseed oil, which was used as a hydrocarbon precursor. After ignition of the wick and subsequent stabilization of its flame, the air pump was switched on and the funnel was gently pulled above the wick. Then, the air flow was accurately set via the flow meter and finally the funnel was lowered over the inflamed wick. According to this setup, several combustion scenarios were simulated at three distinct wick dimensions (diameter and height  $d \times h = 0.9 \times 2.5$  cm;  $1.2 \times 2.5$  cm and  $2.4 \times 2.5$  cm) and air flow ranging within  $0.0014$ – $0.0052$   $\text{m}^3/\text{min}$  with a step of  $\sim 0.0005$ – $0.0009$   $\text{m}^3/\text{min}$ . The choice of these parameters was related to tuning of the oxygen-fuel ratio, which is critical for the physical properties of the deposited carbon nanostructures [16, 21, 29]. Thus, by manipulating *in-situ* the combustion of rapeseed oil and observing the corresponding morphological and structural changes in the nanomaterials, we were capable of determining the probable mechanism of graphite-to-diamond transformation.

### 2.2. Flame characteristics

An inverted tin funnel was utilized to generate a laminar diffusion flame, whose characteristics are illustrated in Fig. 2.

In the absence of a funnel, the flame flow of the ignited wick was turbulent and the atmospheric oxygen diffused into the vaporized fuel (rapeseed oil), creating three visible flame regions, namely outer, inner and center. After applying the funnel, the combustion was still maintained by diffusion, but the gas flow converted from turbulent to laminar due to the narrow exhaust vent. At that stage, four distinct regions with specific flame/flow characteristics were observed. The first

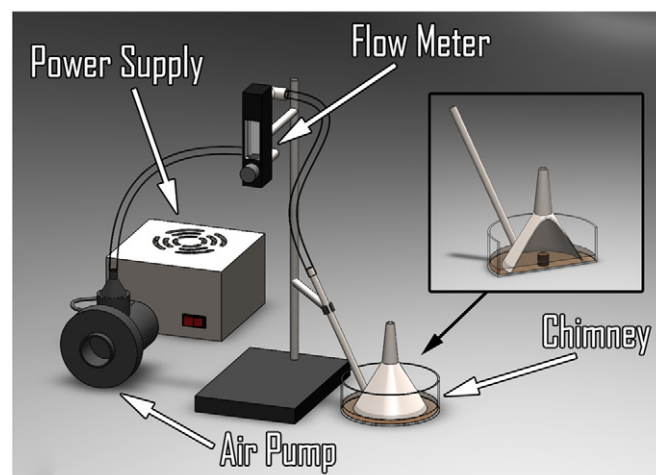


Fig. 1. General view of the combustion system.



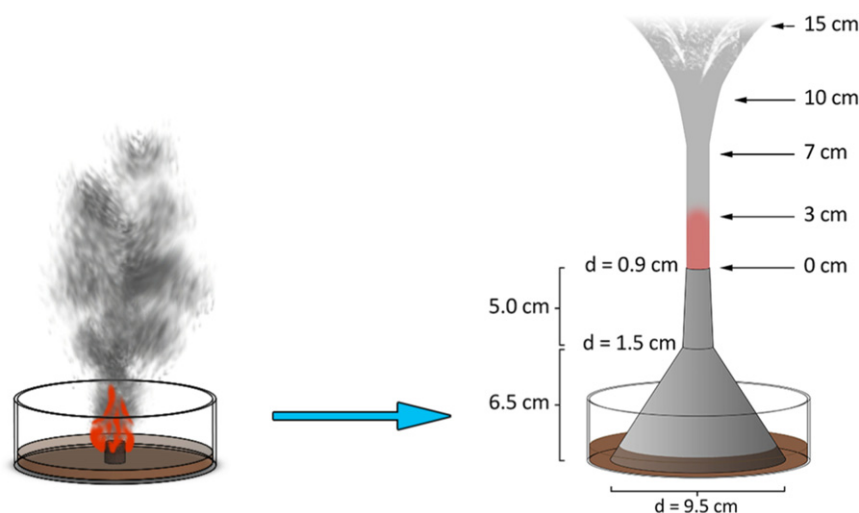


Fig. 2. Schematic representation of the flame characteristics.

one was located within 0–3 cm above the funnel's tip and associated with a laminar flame flow possessing orange-red color, caused by the incandescence of very fine soot particles produced in the flame. The second region was situated within 3–7 cm above the funnel and referred to as post-flame (thermal plume) region, where the flame completely vanished [18]. For our particular case, however, the flow in that region was still laminar, while at the third and fourth fume domains (7–10 cm; 10–15 cm), also assigned to the thermal plume region, the gas-flow reconverted to turbulent.

The flame temperature in an open atmosphere and upon controlled combustion in the funnel was measured using a Signstek 3 1/2 6802 II dual channel digital thermometer with a WRNK- 187 K-type thermocouple probe sensor, allowing thermal readings within 0–1100 °C with a measurement accuracy of  $\pm 0.1$ – $0.4$  °C. Initially, the probe of digital thermometer was placed in the flame of the burning wick and its temperature was recorded after reaching stable value within  $\pm 0.5$  °C. Subsequently, the same procedure was applied upon setting the funnel and the flame temperature was determined above the funnel's tip at a specific distance associated with each flame/fume region (see Fig. 2). According to that setup, a certain amount of solid carbonaceous particles with a very low apparent density of  $\sim 0.04$ – $0.59$  g/cm<sup>3</sup> may accumulate on the sensor probe [29]. However, this would adversely affect the readings only upon precipitation of sufficiently thick carbon films (e.g. tenth of a mm) causing shielding of the temperature effect.

### 2.3. Determination of the oxygen-fuel ratio and deposition conditions

The oxygen-fuel ratio is defined as the mass ratio of oxygen to fuel vapor available in the combustion process [10–12,15,17,19]. However, due to the presence of a liquid phase in the combustion reactor and since a cylindrical wick with a certain surface area was used to provide the oil vapor; we determined the oxygen-fuel ratio in relative molar units. The exact oxygen content was deduced as one fifth of the total air flow reaching the reactor, as the air contains  $\sim 20\%$  oxygen and  $\sim 80\%$  nitrogen. The mole fraction of oxygen was then calculated by knowing that at standard temperature and pressure 1 mol of air occupies 22.4 l. The fuel content was estimated by measuring the amount of liquid rapeseed oil consumed for 20 min continuous combustion at each particular air flow and wick dimensions (see Section 2.1). Then, the molar mass of the evaporated liquid was determined by taking into account the molecular weight of rapeseed oil (992 g/mol) and its mass density (0.9186 g/cm<sup>3</sup>) [37].

The deposition of carbon nanostructures was performed on  $2.5 \times 2.5$  cm microscope glass slides (Fisher Scientific, USA) at burner-to-substrate distance  $L \sim 3$ – $15$  cm, corresponding to each flame/flow

region, for a variety of oxygen-fuel ratios determined by the chosen air flow and wick's dimensions. The deposition time  $t$  was varied within 20–60 s in order to produce  $\sim 10$ – $40$   $\mu\text{m}$  thick carbon coatings [29].

### 2.4. Surface characterization

Circumstantial characterization data of the synthesized carbonaceous nanoparticles are provided in our previous investigation [29]. Here, we utilized scanning electron microscopy (SEM), Raman spectroscopy, X-ray photoelectron spectroscopy (XPS), transmission electron microscopy (TEM) and X-ray diffraction (XRD) ensuring the data required for comparative analysis and establishment of the probable formation mechanism. The SEM experiments were performed using a Hitachi SU-70 field emission scanning electron microscope and images were taken at magnifications up to 25 kX. Raman spectra of the coatings were recorded from 1000 to 1900 cm<sup>−1</sup> with an acquisition time of 300 s in a Horiba LabRam HR Evolution Confocal Raman Spectrometer, using a 20 mW/532 nm He-Ne laser excitation system. Subsequently, the spectra were deconvoluted via a five-peak fitting procedure after a linear baseline subtraction. The high resolution XPS data were collected with a Thermo Fisher ESCALAB 250 X-ray photoelectron spectrometer at a step of 0.1 eV. The molecular structure of carbon samples was evaluated via TEM and XRD using a Zeiss Libra 120 system operating at 120 kV with a point-to-point resolution of 0.34 nm and a Panalytical X'Pert Pro diffractometer operating in Bragg-Brentano mode, respectively. An incident X-ray beam was generated with Cu K $\alpha$  radiation ( $\lambda = 1.54$  Å) and the samples were scanned from 20° to 100° of  $2\theta$ , at 0.0032826° scan step size, 1° anti-scatter slit, 1/2° fixed divergence slit and 15 mm mask.

## 3. Results and discussion

### 3.1. Morphological features of the generated nanoparticles

Fig. 3 represents the morphology of carbon nanoparticles during different stages of the combustion process.

As seen in Fig. 3a, the open flame generates quasispherical nanoparticles that aggregate in a fractal-like network composed of elongated carbon chains separated by micro- nanoscale pores. Such a configuration is associated with superhydrophobic carbon soot that is highly fragile upon mechanical intervention and water interactions due to the prevalent sp<sup>2</sup> hybridization and the presence of dangling  $\pi$ – $\pi^*$  bonds [16,29,38]. Upon controlled combustion in our funnel, however, the soot changes its morphology and structure, and three prominent transition states occur. Initially, at an air flow of 0.0042 m<sup>3</sup>/min, the soot is in



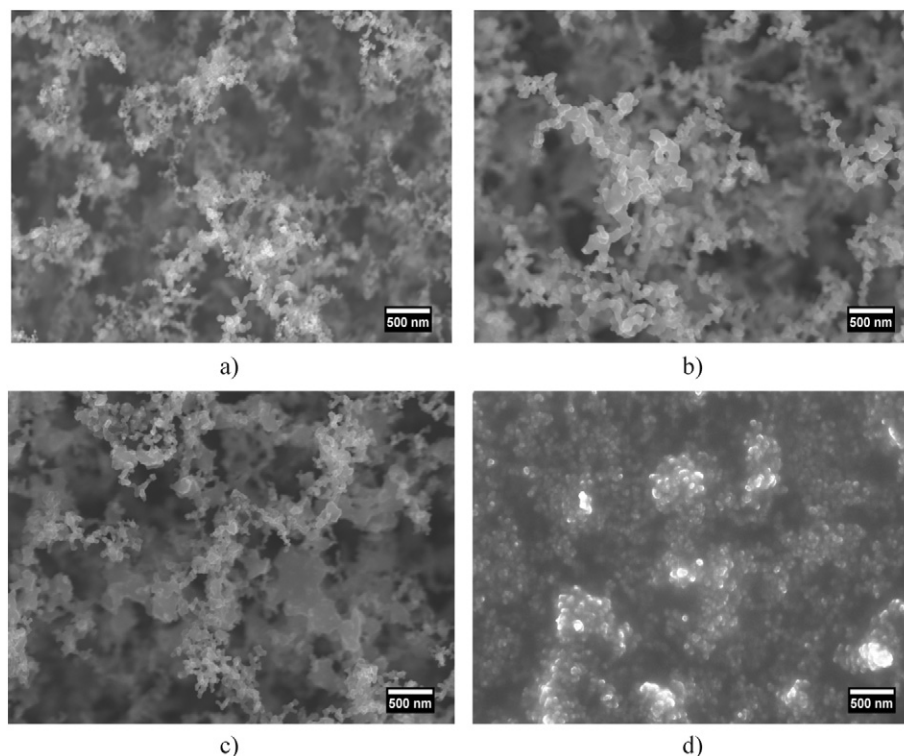


**Fig. 3.** Scanning electron micrographs of carbon nanostructures deposited at wick dimensions of  $1.2 \times 2.5$  cm and  $L \sim 3$  cm via a) an open flame and b) upon controllable combustion at an air flow of  $0.0042 \text{ m}^3/\text{min}$ , c)  $0.0033 \text{ m}^3/\text{min}$  and d)  $0.0024 \text{ m}^3/\text{min}$ .

an intermediate state, where most of the carbon chains look dense and fused, but some small areas still contain sphere-like particles (see Fig. 3b). Further reduction of the air flow to  $0.0033 \text{ m}^3/\text{min}$  induces a complete morphological transformation of the soot. At that stage, the nanoparticles are tightly connected and fused; forming elongated quasisquares, but the overall fractal-like structure is preserved. This arrangement corresponds to inherently robust carbon soot with an increased  $\text{sp}^3$  hybridization and substantially reduced amount of  $\pi-\pi^*$  bonds [16,29]. A subsequent decrease in the air flow to  $0.0024 \text{ m}^3/\text{min}$  causes a remarkable modification of both the morphology and structure of the uncombusted carbon particles. They convert into fine nanoscale grains, growing as bigger carbon clusters with reduced porosity compared to the soot (see Fig. 3d). These features of the particles completely match those in our previous study and presume the formation of highly  $\text{sp}^3$  hybridized diamond-like carbon (DLC) with a short-range ordered nanocrystallinity [29]. The reported results suggest also an oxygen-fuel ratio dependent graphite-to-diamond transformation, which is partially supported by the kinetic models of soot formation in laminar premixed flames [21–23]. The models do not address possible structural transitions, but do explain the morphological alteration in the soot as a consequence of the reduced oxygen content and will be used as a key reference later in the article.

### 3.2. Structural analysis

To verify that the grain-like clusters deposited via the current experimental setup could be ascribed to DLC, we performed Raman spectroscopy, the results of which are shown in Fig. 4.

The visible Raman spectrum of amorphous carbon, such as soot, shows two prominent features and some minor modulations that can accurately be analyzed using a five-band fitting procedure [39]. According to that approach, the intensity peaks at  $\sim 1590 \text{ cm}^{-1}$  and  $\sim 1350 \text{ cm}^{-1}$  are associated with the G-band and D1-band of disordered graphite. The first one corresponds to the ideal graphitic lattice vibration mode with  $E_{2g}$  symmetry, while the D1-band is “forbidden” in

perfect graphite and arises only in the presence of disorder due to the activation of  $A_{1g}$  symmetry mode [39,40]. Another three bands, labeled as D2, D3 and D4, complement the Raman spectra and account for lattice vibrations analogous to that of the G-band (D2-band), amorphous carbon fraction of soot (D3-band) and  $\text{sp}^2-\text{sp}^3$ , C—C or C =C stretching vibrations (D4-band) [39]. The exact location of all five bands and their intensity depends on the type of material and its molecular structure (short-range order) [39,40].

At an open flame, the corresponding Raman spectrum accounts for the formation of highly disordered graphitic carbon with almost equal intensities of D1-band and G-band, giving an  $I_{D1}/I_G$  ratio of 0.9. Also, the high D1-band intensity is strictly related to a sixfold aromatic ring structure of the particles, while the D3-band accounts for the large fraction of amorphous carbon soot [39,40]. Such an interpretation is in perfect agreement with the quasispherical fractal-like network of the soot, revealed by the SEM (see Fig. 3a). Upon controlled combustion at an air flow of  $0.0033 \text{ m}^3/\text{min}$ , both D1-band and D3-band decrease their intensities and the  $I_{D1}/I_G$  ratio reduces up to  $\sim 0.76$ . Intuitively, this is attributed to the decreased quantity of disordered aromatic ring-shaped particles, which is clearly evident from the alteration of the soot's morphology (see Fig. 3c), as well as the increased amount of  $\text{sp}^3$  bonds in the material [16,29]. We referred this state to as “modified” carbon soot with inherent robustness in terms of water jetting and dynamic water droplet interactions [16]. Although the spectra in Fig. 4a and b are similar to those reported for nanodiamonds, the location of G-band at  $1591 \text{ cm}^{-1}$  differs towards that of nanodiamond ( $\sim 1640 \text{ cm}^{-1}$ ), indicating the absence of diamond phase and nanostructures composed mainly of graphitic shells [31].

Further reduction of the air flow to  $0.0024 \text{ m}^3/\text{min}$  causes a significant modification of the Raman spectrum. First, the D1-band intensity decreases vastly and the  $I_{D1}/I_G$  ratio collapses to  $\sim 0.67$ , indicating less disordered structure and distribution of clusters with orders and dimensions different than those of the aromatic rings [40]. Moreover, the D1-band shifts up to  $\sim 1360 \text{ cm}^{-1}$  and overlaps the Raman scattering peak for bulk diamond at  $\sim 1332 \text{ cm}^{-1}$  [2,40]. Second, the G-band is also

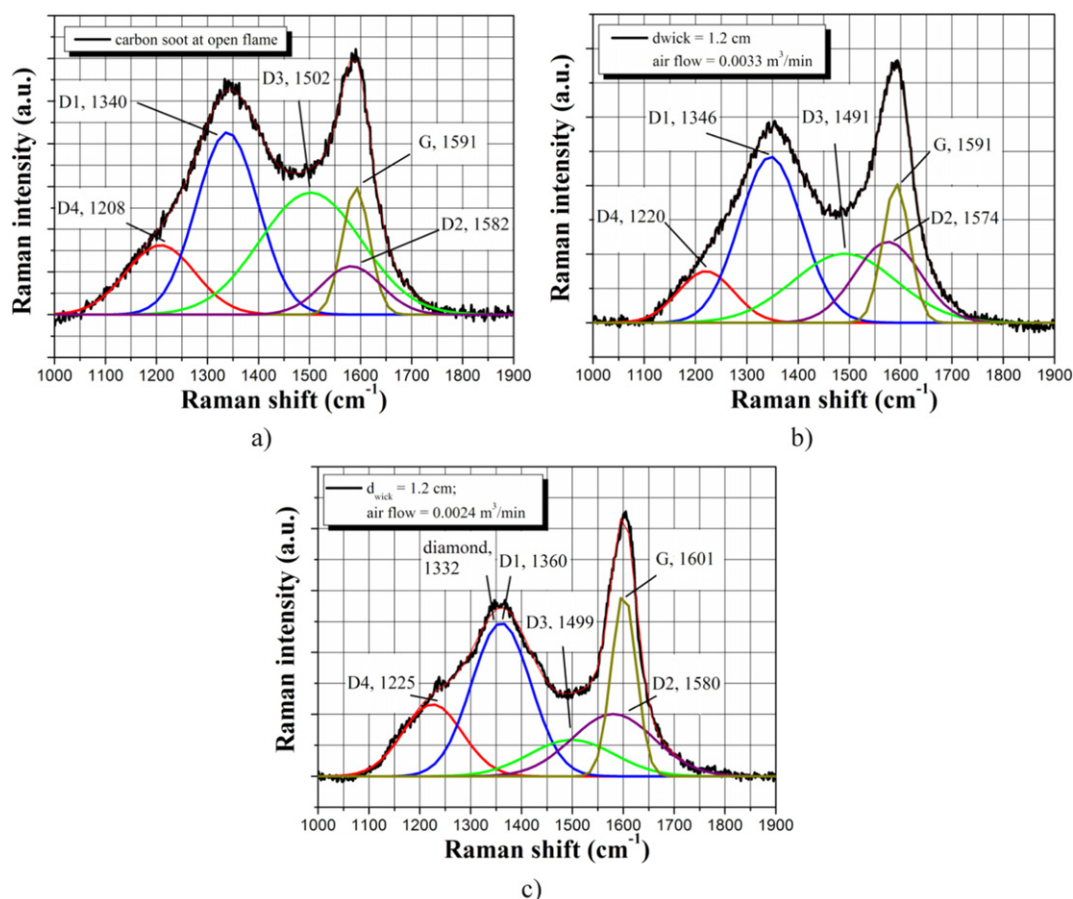


**Fig. 4.** Raman spectra of carbon nanostructures deposited at wick dimensions of  $1.2 \times 2.5$  cm and  $L \sim 3$  cm via a) an open flame and b) upon controllable combustion at an air flow of  $0.0033 \text{ m}^3/\text{min}$  and c)  $0.0024 \text{ m}^3/\text{min}$ . The goodness-of-fit is indicated by a high correlation coefficient value within 0.995–0.997.

shifted up from  $\sim 1591 \text{ cm}^{-1}$  to  $1601 \text{ cm}^{-1}$ , likely as a result of the increased  $\text{sp}^3$  content triggered by a change of  $\text{sp}^2$  configuration from rings to olefinic  $\text{C}=\text{C}$  groups with higher vibration frequencies [40]. In addition, the D3-band is less prominent in comparison with its intensity for the first two regimes of combustion (Fig. 4a, b); meaning that the overall soot content is low. Very similar spectral behavior is reported for nanodiamonds synthesized by ethanol dissociation [41] or using low power density microwave plasma-enhanced chemical vapor deposition [2]. These results support the probability for structural soot-to-DLC

transformation, implied by the SEM imaging and unambiguously stated in our previous report [29].

Another corroborative argument is that the grain-like clusters showed in Fig. 3d, as well as their Raman spectrum in Fig. 4c, may correspond to an amorphous carbon with  $\sim 80\% \text{ sp}^3$  bonds [29]. This is confirmed by a high-resolution XPS to the C1s performed on the grain-like nanostructures, as shown in Fig. 5.

The survey scan of these nanostructures reveals that the main component is carbon being  $\sim 92.5 \text{ at.}\%$  accompanied by oxygen with atomic

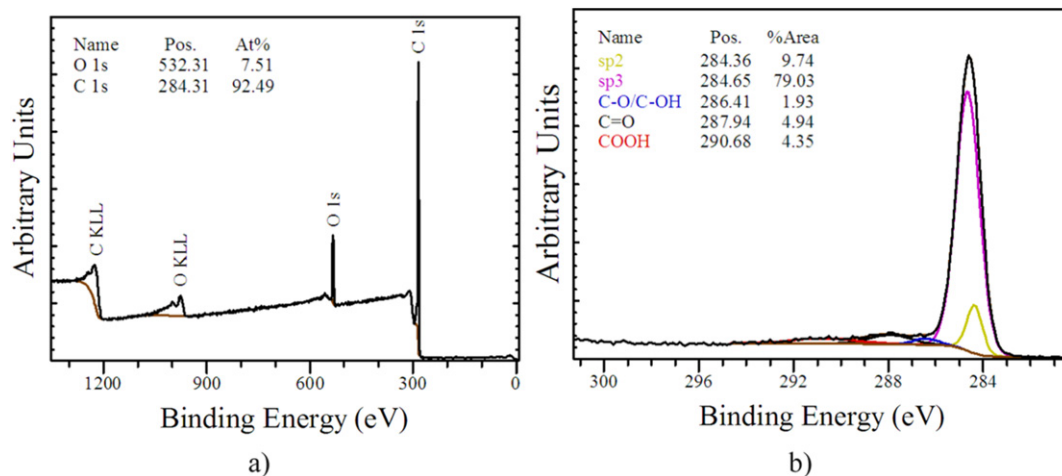


**Fig. 5.** Experimental data of a) XPS spectrum and b) C1s photoelectron core level of the grain-like clusters deposited at wick dimensions of  $1.2 \times 2.5$  cm, upon controlled combustion at an air flow of  $0.0024 \text{ m}^3/\text{min}$  and  $L \sim 3$  cm.

percentage of  $\sim 7.5$  at.%. The two minor  $C_{KLL}$  and  $O_{KLL}$  peaks at higher binding energies correspond to the emission of Auger electrons of carbon and oxygen elements. In addition, the deconvolution of C1s shows mainly  $sp^3$  hybridized carbon with  $sp^3$  content approaching  $\sim 80\%$ , along with the presence of other functional groups such as epoxy/hydroxyl ( $C-O-C/C-OH$ ), carbonyl ( $C=O$ ) and carboxylic acid ( $COOH$ ) groups. The peak of  $COOH$  group is wide, suggesting the possibility for  $\pi-\pi^*$  bonds formation, associated with the negligible  $sp^2$  hybridization ( $\sim 10\%$ ). Our material is considered in the literature as tetrahedral amorphous carbon (ta-C) that belongs to the family of DLC, thus, confirming the proposed structural transition [2,40].

The molecular structure of the samples was further investigated using TEM along with selected area electron diffraction (SAED) and XRD, as presented in Figs. 6 to 8

The TEM image in Fig. 6a confirms the spherical-like morphology of the soot generated via an open flame. The corresponding SAED pattern (Fig. 7a) exhibits a few continuous rings and diffused halos, suggesting the presence of a short-range order and amorphous phase. The diffraction rings are mainly assigned to graphite (G) structure and one peak that possibly could match diamond (D). Upon controlled combustion at an air flow of  $0.0033 \text{ m}^3/\text{min}$  (Fig. 6b), the scanned area indicates overlapped and fused carbon nanoparticles, whereas the SAED pattern shown in Fig. 7b mainly two diffused halos, one assigned to graphitic-like and the other to diamond-like nanostructures. In contrast, Fig. 6c illustrates more crystalline structure of the particles generated at an air flow of  $0.0024 \text{ m}^3/\text{min}$ . Denser composites with non-spherical morphology are observed and the rings in the SAED pattern are well defined (see Fig. 7c). The atomic d-spacing of the nanostructures in this particular case can be ascribed to both graphitic-like and diamond-like carbon with less amorphous phase in overall. A summary of these measurements along with the STD d-spacing for diamond and graphite is presented in Table 1.

Although graphitic-like structures are still present, the appearance of mainly  $sp^3$  hybridized carbon and a short-range nanocrystallinity (see Fig. 5 and Table 1) imply that the combustion regime at an air flow of  $0.0024 \text{ m}^3/\text{min}$  and wick dimensions of  $1.2 \times 2.5 \text{ cm}$  tends to form carbon with mostly diamond phase.

Finally, the XRD measurements shown in Fig. 8 will clarify whether the synthesized material at an air flow of  $0.0024 \text{ m}^3/\text{min}$  should be considered as nanodiamond or DLC. By definition, diamond is a tetrahedral ( $sp^3$ ) bonded allotrope of carbon; however, not every material with considerable  $sp^3$  bonding could possess the properties of bulk diamond [2]. This is the case for DLC, which has many of the bulk diamond features, but is fundamentally amorphous [2]. Furthermore, the

appearance of crystallinity and mainly tetrahedral bonds is not an absolute prerequisite for the possession of bulk diamond properties, as the grain size and the amount of amorphous grain boundaries can “shift” the material towards DLC or bulk diamond [2].

The XRD spectrum shows one strong peak at  $2\theta$  of  $28.5^\circ$  ( $2^\circ$  apart from the graphite peak), which probably is induced by the graphite-like carbon content in the material. In addition, a weak peak at  $2\theta$  of  $43.5^\circ$  clearly shows the appearance of (111) textured diamond. This peak is with negligible intensity, which means that the crystallinity is indeed on a short-range and most of the material is amorphous. Therefore, based on the detailed characterization and the nomenclature for crystalline and amorphous diamond [2], we conclude that the above discussed nanostructures should be considered as DLC rather than nanodiamond.

### 3.3. Structural and morphological variations in the nascent nanoparticles as a function of the experimental conditions

In this section, we aim to clarify the degree of importance of the flame temperature, oxygen-fuel ratio, burner-to-substrate distance  $L$  and the deposition time  $t$  for the formation of graphite-like or diamond-like materials. Fig. 9 reveals 2-D and 3-D maps of the flame temperature profiles, recorded in an open environment and upon controlled combustion.

The incomplete combustion of rapeseed oil in the open atmosphere creates an orange-red colored flame, whose temperature varies within  $520\text{--}580^\circ\text{C}$ , which is in good agreement with the data reported for diffusion flames in open environments [18]. The observed deviations of  $\sim 60^\circ\text{C}$  from measurement to measurement (three sets for each size of the wick) are likely due to the turbulent nature of the flame. Since it moves around chaotically, some cooler fluxes from the surrounding atmosphere interact with the sensor probe, causing these slight upward or downward thermal shifts. In contrast, upon controlled combustion, the thermal readings are reproducible and two major parameters affect the flame color and its temperature, namely the air flow and wick's dimensions.

Careful analysis of the 3-D maps in Fig. 9 shows that at constant air flow and distance  $L$  (e.g.  $0.0052 \text{ m}^3/\text{min}$ ;  $L \sim 3 \text{ cm}$ ), a gradual increase in the wick's diameter ( $d_{\text{wick}}$ ) from  $0.9 \text{ cm}$  to  $2.4 \text{ cm}$  leads to an increase in the flame temperature ( $T_{\text{flame}}$ ) from  $\sim 200^\circ\text{C}$  up to  $\sim 450^\circ\text{C}$ . This is a consequence of the larger amount of fuel involved in the combustion that is giving off more heat in the subsequent exothermic chemical reaction. On the other hand, at constant  $d_{\text{wick}}$  of  $0.9 \text{ cm}$  and  $L \sim 3 \text{ cm}$ , the reduction of air flow from  $0.0052 \text{ m}^3/\text{min}$  to  $0.0033 \text{ m}^3/\text{min}$  causes an

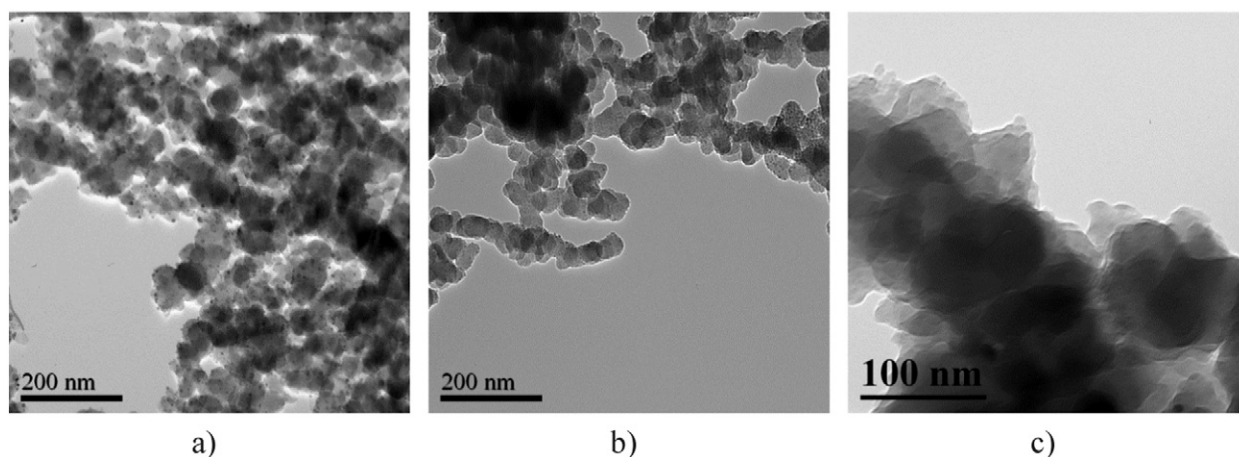


**Fig. 6.** TEM images of the carbon nanostructures deposited at wick dimensions of  $1.2 \times 2.5 \text{ cm}$  and  $L \sim 3 \text{ cm}$  via a) an open flame and b) upon controllable combustion at an air flow of  $0.0033 \text{ m}^3/\text{min}$  and c)  $0.0024 \text{ m}^3/\text{min}$ .



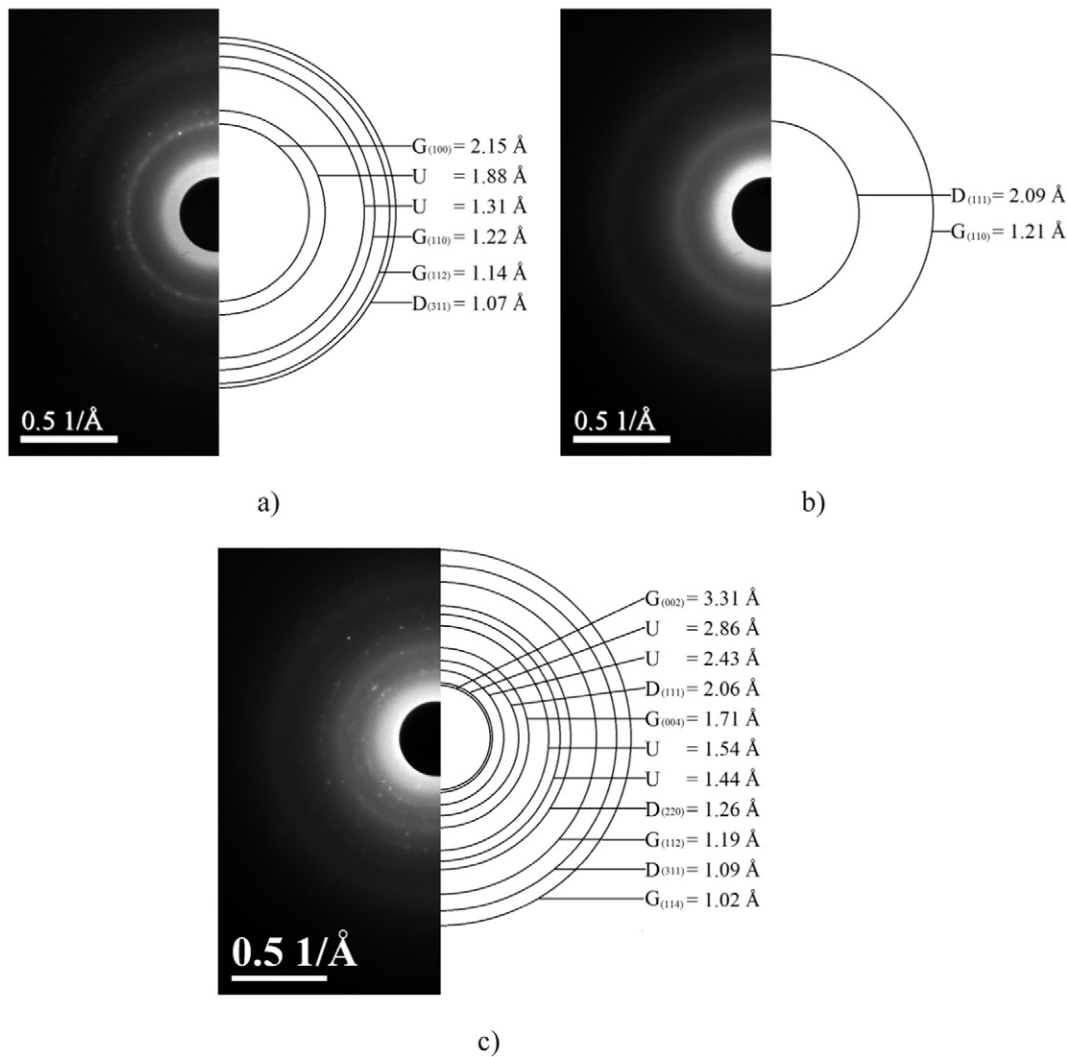


**Fig. 7.** SAED images of the carbon nanostructures deposited at wick dimensions of  $1.2 \times 2.5$  cm and  $L \sim 3$  cm via a) an open flame and b) upon controllable combustion at an air flow of  $0.0033 \text{ m}^3/\text{min}$  and c)  $0.0024 \text{ m}^3/\text{min}$ . The indices G, D and U correspond to graphite, diamond and unknown phase, respectively.

increase in  $T_{\text{flame}}$  with  $\sim 77^\circ\text{C}$  (see Fig. 9b), followed by relatively rapid cooling of  $\sim 67^\circ\text{C}$  at air flow of  $0.0019 \text{ m}^3/\text{min}$ . Similar temperature trend is observed in Fig. 9c, which implies that the amount of released thermal energy does not necessarily decay by reducing the air flow, as the combustion efficiency depends also on the success rate of oxidation

[42]. In addition, at equal other conditions (constant  $d_{\text{wick}}$  and air flow), the variations in distance  $L$  induce corresponding changes in the flame temperature due to the specific characteristics of each flame/flow region (see Section 2.2).

Simultaneously with the thermal measurements, we coated approximately hundred  $2.5 \times 2.5$  cm glass slides with carbon nanoparticles, generated at each measurement position, in order to correlate their morphological and structural peculiarities with the relevant combustion conditions. Regardless of the  $d_{\text{wick}}$ , an air flow of  $0.0052 \text{ m}^3/\text{min}$  promotes the formation of soot particles with either conventional (spherical) or mixed shape, assembled in chain-like aggregates (see Fig. 3a and b), and the flame's orange-red color is similar to that of an open flame. However, the transition to “modified” soot with inherent robustness (see Fig. 3c) is strongly influenced by the air flow and wick's surface area, which also affect the flame appearance. At a  $d_{\text{wick}} = 0.9$  cm, the morphological alteration occurs at an air flow of  $0.0024 \text{ m}^3/\text{min}$  and subsequent increase in  $d_{\text{wick}}$  to 1.2–2.4 cm shifts up the transition point to flow values of  $0.0033 \text{ m}^3/\text{min}$  and  $0.0042 \text{ m}^3/\text{min}$ , respectively. In these stoichiometric regions, the flame width decreases and its color changes to dark red-brown, indicating an enhanced sooting tendency due to the lean oxygen content (at equal deposition time, the reduction of oxygen causes deposition of thicker soot coatings, as reported in ref. [16]). Identical behavior is observed upon analysis of the experimental conditions that trigger the soot-to-DLC transformation. First, the fume

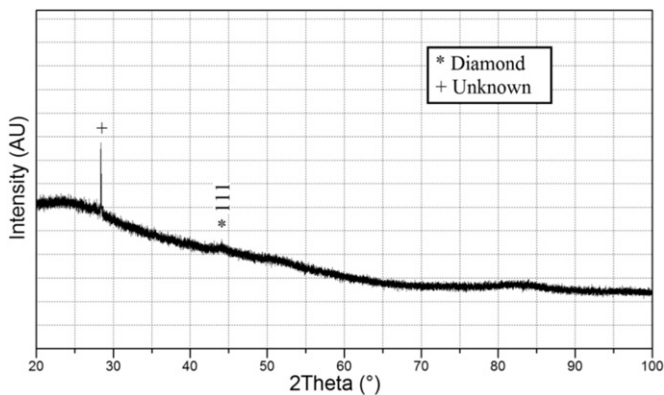


**Fig. 8.** X-ray diffraction of a glass slide coated with carbon nanostructures generated upon controlled combustion at wick dimensions of  $1.2 \times 2.5$  cm, an air flow of  $0.0024 \text{ m}^3/\text{min}$ , and  $L \sim 3$  cm.

**Table 1**

Comparison between the calculated d-spacing (Å) from the SAED patterns at different combustion regimes and the STD d-spacings and Miller index for diamond and graphite.

Open flame	Calculated d-spacing (Å)		d-spacing and Miller index for some C allotropes			
	Air flow 0.0033 m <sup>3</sup> /min	Air flow 0.0024 m <sup>3</sup> /min	Diamond PDF 00-006-0675 Cubic Fd-3m		Graphite PDF 00-023-0064 Hexagonal P63/mmc	
			d-spacing (Å)	Miller index (h k l)	d-spacing (Å)	Miller index (h k l)
2.15	2.09	3.31	2.06	1 1 1	3.36	0 0 2
		2.86			2.13	1 0 0
		2.43			2.03	1 0 1
1.88	1.21	2.06	1.26	2 2 0	1.67	0 0 4
1.31		1.71			1.23	1 1 0
		1.54			1.16	1 1 2
	1.07	1.44	1.07	3 1 1	0.99	1 1 4
1.22		1.26				
1.14		1.19				
1.07		1.09				
		1.02	0.89	4 0 0		

The numbers in bold correspond to either graphite or diamond nanostructures. The latter is coloured in blue, while the previous in red.

alters its color to a light gray, while the flame is completely vanished. Second, the deposition of diamond-like structures becomes favorable only at air flows of 0.0019, 0.0024 and 0.0033 m<sup>3</sup>/min when the wick's diameter ( $d_{wick}$ ) is 0.9, 1.2 and 2.4 cm, respectively. Beyond this narrow range, the combustion conditions promote the formation of “modified”,

mixed or conventional soot particles. Interestingly, a similarity in the  $T_{flame}$  is observed in the vicinity of each transition, regardless of the chosen experimental conditions, as shown in Table 2.

According to Table 2, in two of three scenarios the flame temperature difference between the ranges for modified soot and DLC formation is ~60 °C. On the other hand, the substrate-to-burner distance  $L$  and deposition time  $t$  are irrelevant to the type of synthesized material. However, high-quality carbon nanostructures can be deposited only at  $L \sim 3$  cm and for larger distances the quality rapidly decreases, likely due to the presence of oxidizing agents in the ambient atmosphere [28]. Furthermore, the time  $t$  determines only the thickness of the deposited carbon materials and does not affect any of their physicochemical properties. The above results, along with the resemblance of the  $T_{flame}$  at the transition regions, presume stoichiometric threshold that governs the particles' formation, as hinted in Fig. 10.

The oxygen-fuel ratio diagram confirms that the wick's larger surface area ensures increased amount of oil involved in the combustion, which also correlates with the increased flame temperature. Interestingly, the initial reduction of air flow causes unexpected gradual increase in the oxygen-fuel ratio to a point, where the relative oil vapor content becomes sufficient to decrease that ratio. At this point, different for each  $d_{wick}$ , the required stoichiometric threshold is reached and the nascency of diamond is preferential. Moreover, regardless of the equalized flame temperature values (see Table 2), the incipency of diamond phase is favorable upon increase in the fuel content, because the hydrocarbons are unevenly distributed within the flame, which may facilitate or suppress the successful diamond growth [43]. In other words, there should be a sufficient amount of so called “carbon source” throughout

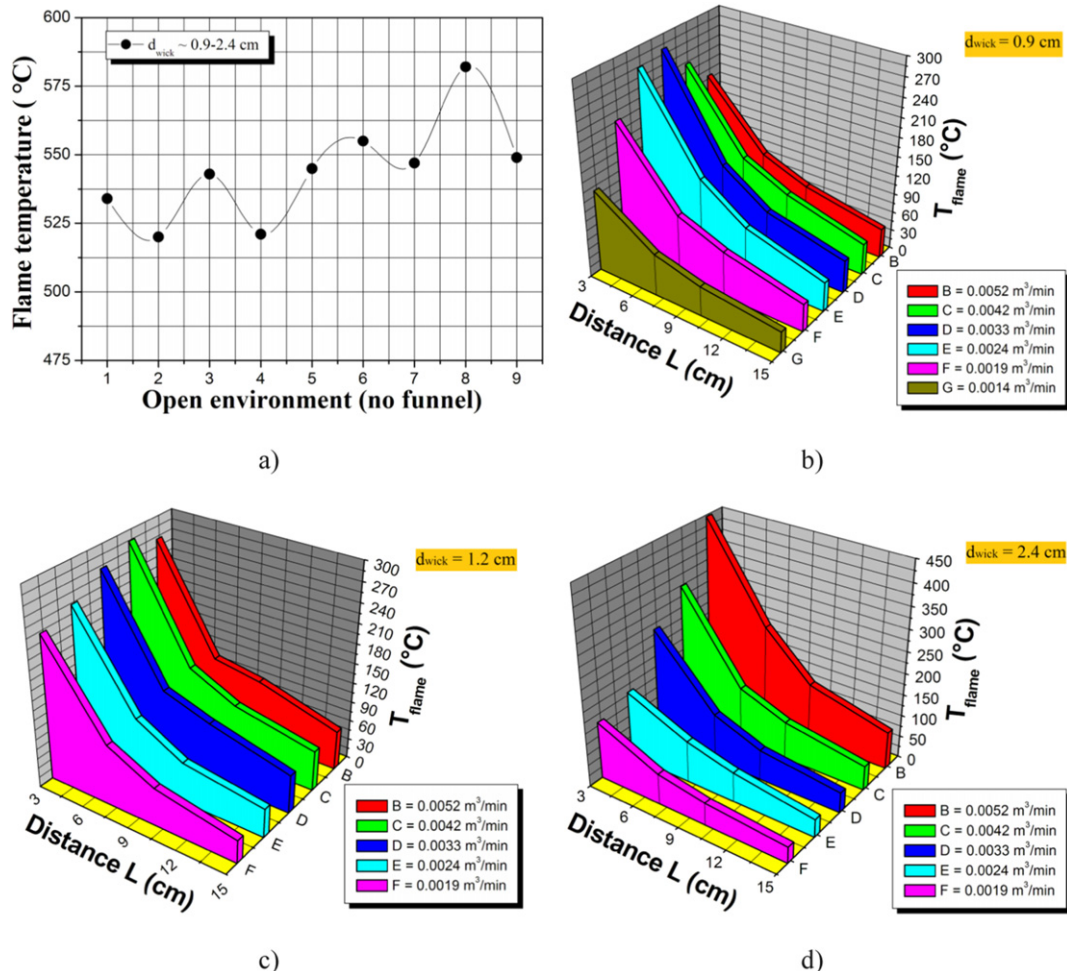


**Fig. 9.** Flame temperature profile in a) an open environment and b) upon controlled combustion at wick dimensions of 0.9 × 2.5 cm, c) 1.2 × 2.5 cm and d) 2.4 × 2.5 cm.

**Table 2**

Summarized experimental data for the type of synthesized carbon materials as a function of the deposition conditions.

Air flow (m <sup>3</sup> /min)	d <sub>wick</sub> (cm)	T <sub>flame</sub> (°C)	L (cm)	Material
0.0052	0.9	200	3	Conventional soot
0.0042	0.9	240	3	Mixed soot
0.0033	0.9	277	3	Mixed soot
0.0024	0.9	270	3	Modified soot
0.0019	0.9	210	3	DLC
0.0052	1.2	270	3	Mixed soot
0.0042	1.2	285	3	Mixed soot
0.0033	1.2	270	3	Modified soot
0.0024	1.2	240	3	DLC
0.0019	1.2	225	3	No deposition
0.0052	2.4	450	3	Mixed soot
0.0042	2.4	325	3	Modified soot
0.0033	2.4	263	3	DLC
0.0024	2.4	150	3	No deposition
0.0019	2.4	125	3	No deposition

the flame in order to promote the formation of the required carbonaceous material [43]. These observations suggest that just a small part of the oxygen in the system is efficiently used to oxidize the fuel, while perhaps the excessive amount is released via the exhaust vent (funnel's tip). Hence, the estimation of the exact stoichiometry during the combustion process has a qualitative rather than a quantitative character. Nevertheless, the experimental conditions are in good agreement with the state-of-the-art in flame synthesis of diamond, since its formation is favorable in limited stoichiometric regions with sufficient mole fractions of fuel and lean oxygen content that suppresses the appearance of potential oxidizing agents [17,28]. Moreover, the observed tendency in DLC formation and the measured flame temperatures are in excellent agreement with the findings in our previous study, thereby, confirming that the basic mechanism of soot-to-DLC transformation is identical in both combustion systems [29].

### 3.4. Probable mechanism of the observed graphite-to-diamond transformation

The next few paragraphs provide new insights, although speculative to a certain extent, about the observed structural modifications during the incomplete combustion of rapeseed oil. For that purpose, we describe the formation mechanism of graphite-like and diamond-like nanostructures via the theory of soot formation in flames along with relevant numerical models for the reaction kinetics of the incipient carbonaceous particles [21–23,44]. Our considerations exclude the possibility for thermodynamically induced phase transition, since the maximum measured flame temperature of ~580 °C is well below the temperature of oxyacetylene flames, commonly used for thermal activation of the gas species and subsequent diamond formation [10–12,15,17]. Also, the proposed mechanism does not consider the probability for direct

diamond formation from amorphous precursors, since this method requires high pressures and/or temperatures, which is inconsistent with the experimental conditions of diamond synthesis in this paper [45,46]. In addition, the results in Section 3.3 imply that the structural transition occurs in the flame. For instance, the incipency of DLC outside the flame (i.e. on the substrate surface) is unlikely due to the necessity of substrate temperatures within ~500–750 °C [10]. These values are unachievable with our combustion system based on the thermal profiles in Fig. 9 and previously measured substrate temperatures [29]. If the carbon particles indeed undergo transformation on the substrate, then any variations in the substrate-to-burner distance  $L$  should cause the deposition of carbon nanostructures with different morphology [47]. Furthermore, it has been observed that diamond formation on solid substrates is strongly influenced by the deposition time  $t$  and the diamond peak in the Raman spectrum has been detected after prolonged and continuous deposition [17]. Since  $L$  and  $t$  are responsible for the quality and thickness of the material, and not for its physico-chemical properties (see Section 3.3), the hypothesis for substrate-guided soot and DLC growth seems inapplicable to our particular conditions.

According to the fundamentals of combustion, the solid particulate matter formation begins with homogeneous nucleation of polycyclic aromatic hydrocarbons (PAHs) generated by thermal decomposition of the vaporized fuel (here, rapeseed oil) [44]. These PAHs pack together into hexagonal face-centered arrays, known as platelets, which further arrange in layers to form crystallites and the primary spherical soot particle (typically  $10^3$  crystallites per particle). The subsequent formation of larger particles and aggregates is governed by the interplay between several processes such as coalescence, coagulation, surface growth and aggregation [21–23]. Initially, the pristine soot particles collide to one another and coalesce completely at small scales (units of nm) [22]. As the size of secondary particles becomes significantly larger than that of the constituent primary particles, the coalescence is replaced by coagulation, followed by chain-like aggregation due to insufficient time for complete fusing [22]. The validity of this hypothesis is confirmed experimentally in Fig. 3a, as the SEM imaging shows a fractal-like network of quasispherical soot particles with approximate size of 50 nm, exceeding by a factor of ~25 the size of pristine particulate [44]. Since the overall process has duration of a few milliseconds, a detailed modeling shows an equal growth rate for the candidate and already aggregated particles. Hence, the models suggest simultaneous occurrence of nucleation, surface growth and aggregation [21,22].

On the other hand, the particles' morphology is strongly influenced by the nucleation rate that depends on the oxygen-fuel ratio and its manipulation can trigger a transition from coalescent to aggregate particle growth [21]. At low rates and constant surface growth, the aggregated particles acquire a spherical shape, while at intensive nucleation the degree of particle overlapping increases significantly [21]. In fact, an experimental study of post-flame soot particles in laminar diffusion flames shows a remarkable similarity of the soot's morphology at low oxygen-ethene ratio with that illustrated in Fig. 3c [48]. Unfortunately, the authors do not disclose any data regarding the ratio of chemical bonds in the soot; therefore, it is impossible to establish full correlation between their and our findings. Moreover, the relevant numerical models do not account for possible structural alterations in the pristine particles ( $sp^2/sp^3$  ratio, for instance), caused by changes in the oxygen-fuel ratio and subsequently the nucleation rate [21–23]. However, a study of the early history of soot formation from various hydrocarbon diffusion flames shows that the soot's structure and morphology could be manipulated depending on the fuel's chemistry and distance between the exit port and collecting substrate [47]. Surprisingly, and in line with our observations, the earliest deposits from benzene (aromatic molecule) are of non-aromatic nature [47]. These results support the hypothesis that at certain reaction kinetics an aromatic molecule (e.g. the PAHs that nucleate as conventional quasispherical soot) can be transformed into a non-aromatic one (e.g. non-aromatic grain-like clusters of DLC).

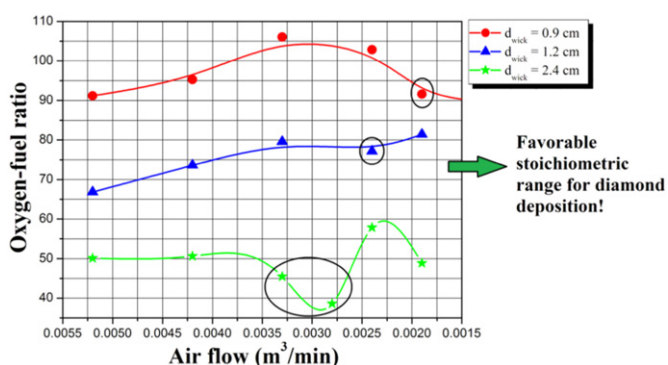


Fig. 10. Oxygen-fuel ratio towards the applied air flow and wick's surface area.



Although there is a lack of a numerical model that may complement the experimental data, we believe that the morphological modifications and the corresponding changes in  $sp^2/sp^3$  content are closely linked to variations in the reaction kinetics. For instance, during the first stage of collision, the primary solid particles collide and completely coalesce, but this event occurs at a certain kinetic energy of the gas flow. Since from thermodynamic point-of-view this energy depends on the gas temperature i.e. the flame/fume temperature, one can assume with sufficient conviction that cooler flames will possess lower kinetic energy and the gas molecules (the PAHs) along with the nucleated particles will undergo elastic collisions with reduced velocity and magnitude. Thereby, we hypothesize that the strength of elastic impact is governed by the particles' kinetic energy and their morphology, and structure are determined by the current impact conditions. In this research, the air flow and wick's dimensions are mainly responsible for the values of oxygen-fuel ratio and flame temperature, thus, for the magnitude of subsequent elastic collisions within the flame/gas flow and the transformation of pristine soot to DLC. These speculations correlate well with the proposed nonequilibrium route to nanodiamond formation, where the authors demonstrate that carbon onions can directly be transformed into nanodiamond by kinetically driven mechanism [36]. Identically to our results, carbon onion to nanodiamond conversion is highly successful in a narrow range of incident energies (in our case, specific oxygen-fuel ratio and flame temperature) and beyond that the impact energy is either insufficient to overcome the barrier between  $sp^2$  and  $sp^3$  bonding or high enough to destroy the crystalline region [36].

Of course, the above considerations may raise additional questions regarding the probability of diamond formation simultaneously with the soot rather than a subsequent transformation [32,33] or concerns related with the effect of fuel's chemistry on the particles' morphology and structure [47]. If diamond forms along with the soot, at least a small portion of diamond-like carbon and/or nanodiamond should be available in the final structure deposited at an open flame (no funnel). The coating at this regime is typical superhydrophobic carbon soot with undetectable diamond phase (on a macro and micro scale). In fact, diamond in a candle flame is captured via anodic aluminum oxide foils, ensuring "original state" of the particles at the collecting position [32]. Furthermore, along with nanodiamonds, graphite, fullerenes and amorphous carbon are identified based on the chosen flame region [32]. It is well known that each flame region has a different temperature; therefore, we assume that various carbon particles are collected simply because the kinetics at each region is different. Also, even if the formation is simultaneous, the average candle flame temperature is  $\sim 1400^\circ\text{C}$  [18], which is  $\sim 2.4$  times higher temperature in comparison with that of the burning rapeseed oil. Thus, the candle might be able of supporting "local" thermodynamic phase transition of the nucleated particles within the flame. On the other hand, the concern about the fuel's chemistry is interesting and relevant. The results in this research might be achievable only with a limited number of hydrocarbon precursors, since various fuels decompose differently due to their chemical bonds and composition. As a consequence, the energy released during the initial phase of thermal decomposition and the subsequent flame temperature and reaction kinetics might vary from fuel to fuel, which would affect the particles' formation. The above question is a subject of fundamental importance and requires thorough and detailed theoretical and experimental investigations that are not in the scope of the present article, but will be planned as a future work.

#### 4. Conclusions

In this study, we considered the formation mechanism of graphite-like and diamond-like nanostructures in low temperature laminar diffusion flames. An enhanced combustion system, composed of an inverted tin funnel connected to a flow meter and an air pump, was used to manipulate *in-situ* the incomplete combustion of a cylindrical paper wick immersed in rapeseed oil. The morphological and structural analysis

of the as synthesized materials showed the precipitation of either carbon soot or DLC. Furthermore, the flame temperature profiles and the oxygen-fuel ratios, for the chosen combustion conditions, revealed that the DLC nanostructures could be generated only in a narrow stoichiometric range and  $T_{\text{flame}} \sim 210\text{--}260^\circ\text{C}$ . Beyond that, the carbon nanoparticles were associated with conventional (spherical), mixed or modified (quasisquare shaped) soot. These observations suggested a novel principle of graphite and diamond growth in flames, related with alteration of the reaction kinetics during the combustion process. Our hypotheses correlated partially with the kinetic models of soot formation in flames and were also supported by the recently disclosed nonequilibrium route for nanodiamond formation. We believe that the considered formation mechanism, although speculative to a certain extent, provides new and important information about the fundamentals of combustion and may be used as a benchmark for further development of detailed numerical models.

#### Future work

The future research activities encompass the usage of fuels with different physicochemical properties (chemical composition, flash point, density, viscosity, etc.) in order to assess their influence on the structure and morphology of the generated carbon nanostructures. Also, a comprehensive numerical model that will further enlighten on the reaction kinetics during diamond and graphite synthesis in low temperature diffusion flames is required.

#### Acknowledgments

The authors wish to acknowledge the VCU's Nanomaterials Core Characterization Facility for providing access to the surface characterization equipment. Also, the startup support from Virginia Commonwealth University under grant 137422 is greatly acknowledged.

#### References

- [1] S.H. Friedman, The four worlds of carbon, *Nat. Chem.* 4 (2012) 426.
- [2] O.A. Williams, Nanocrystalline diamond, *Diam. Relat. Mater.* 20 (2011) 621–640.
- [3] V.V. Danilenko, On the history of the discovery of nanodiamond synthesis, *Phys. Solid State* 46 (2004) 595–599.
- [4] R.J. Nemanich, J.A. Carlisle, A. Hirata, K. Haenen, CVD diamond- research, applications and challenges, *MRS Bull.* 39 (2014) 490–494.
- [5] S.S. Yap, W.O. Siew, C.H. Nee, T.Y. Tou, Parametric studies of diamond-like carbon by pulsed Nd: YAG laser deposition, *Diam. Relat. Mater.* 20 (2011) 294–298.
- [6] I. Kumar, A. Khare, Multi- and few-layer graphene on insulating substrate via pulsed laser deposition technique, *Appl. Surf. Sci.* 317 (2014) 1004–1009.
- [7] J. Zemek, P. Jiricek, J. Houdkova, A. Artemenko, M. Jelinek, Diamond-like carbon and nanocrystalline diamond film surfaces sputtered by argon cluster ion beams, *Diam. Relat. Mater.* 68 (2016) 37–41.
- [8] Z. Wu, X. Tian, G. Gui, C. Gong, S. Yang, P.K. Chu, Microstructure and surface properties of chromium-doped diamond-like carbon thin films fabricated by high power pulsed magnetron sputtering, *Appl. Surf. Sci.* 276 (2013) 31–36.
- [9] A.N. Yurkov, N.N. Melnik, V.V. Sychev, V.V. Savranskii, D.V. Vlasov, V.I. Konov, Synthesis of carbon films by magnetron sputtering of a graphite target using hydrogen as plasma-forming gas, *Bull. Lebedev Phys. Inst.* 38 (2011) 263.
- [10] Y. Hirose, S. Amanuma, K. Komaki, The synthesis of high quality diamond in combustion flames, *J. Appl. Phys.* 68 (1990) 6401–6405.
- [11] I. Doi, M.S. Haga, Y.E. Nagai, Properties of DLC films deposited by an oxyacetylene flame, *Diam. Relat. Mater.* 8 (1999) 1682–1685.
- [12] J.B. Donnet, H. Oulanti, T.L. Huu, M. Schmitt, Synthesis of large single crystal diamond using combustion flame method, *Carbon* 44 (2006) 374–380.
- [13] N.K. Memon, S.D. Tse, J.F. Al-Sharab, H. Yamaguchi, A.B. Goncalves, et al., Flame synthesis of graphene films in open environments, *Carbon* 49 (2011) 5064–5070.
- [14] H. Zhu, T. Kuang, B. Zhu, S. Lei, Z. Liu, S.P. Ringer, Flame synthesis of carbon nanostructures Ni-plated hardmetal substrates, *Nanoscale Res. Lett.* 6 (2011) 331.
- [15] K.L. Yarina, D.S. Dandy, E. Jensen, J.E. Butler, Growth of diamond films using an enclosed methyl-acetylene and propadiene combustion flame, *Diam. Relat. Mater.* 7 (1998) 1491–1502.
- [16] K.D. Esmerlyan, C.E. Castano, A.H. Bressler, M. Abolghasemibazaki, R. Mohammadi, Rapid synthesis of inherently robust and stable superhydrophobic carbon soot coatings, *Appl. Surf. Sci.* 369 (2016) 341–347.
- [17] U. Bergmann, K. Lummer, B. Atakan, K.K. Höinghaus, Flame deposition of diamond films: an experimental study of the effects of stoichiometry, temperature, time and the influence of acetone, *Ber. Bunsenges. Phys. Chem.* 102 (1998) 906–914.

- [18] V. Babrauskas, Temperatures in Flames and Fires, [www.doctorfire.com/flametmp.html](http://www.doctorfire.com/flametmp.html). Last access: October 25, 2016.
- [19] J.J. Schermer, W.A.L.M. Elst, L.J. Giling, The influence of differences in gas phase between turbulent and laminar acetylene-oxygen combustion flames on diamond growth, *Diam. Relat. Mater.* 4 (1995) 1113–1125.
- [20] F. Ossler, S.E. Canton, J. Larsson, X-ray scattering studies of the generation of carbon nanoparticles in flames and their transition from gas phase to condensed phase, *Carbon* 47 (2009) 3498–3507.
- [21] M. Balthasar, M. Frenklach, Detailed kinetic modeling of soot aggregate formation in laminar premixed flames, *Combust. Flame* 140 (2005) 130–145.
- [22] P. Mitchell, M. Frenklach, Particle aggregation with simultaneous surface growth, *Phys. Rev. E* 67 (2003) 061407.
- [23] N. Morgan, M. Kraft, M. Balthasar, D. Wong, M. Frenklach, P. Mitchell, Numerical simulations of soot aggregation in premixed laminar flames, *Proc. Combust. Inst.* 31 (2007) 693–700.
- [24] T.S. Totton, D. Chakrabarti, A.J. Misquitta, M. Sander, D.J. Wales, M. Kraft, Modelling the internal structure of nascent soot particles, *Combust. Flame* 157 (2010) 909–914.
- [25] T.S. Totton, A.J. Misquitta, M. Kraft, A quantitative study of the clustering of polycyclic aromatic hydrocarbons at high temperatures, *Phys. Chem. Chem. Phys.* 14 (2012) 4081–4094.
- [26] F. Ossler, L. Vollenhag, S.E. Canton, J.B.A. Mitchell, J.L. Garrec, et al., Dynamics of incipient carbon particle formation in a stabilized ethylene flame by in situ extended-small-angle and wide-angle X-ray scattering, *Carbon* 51 (2013) 1–19.
- [27] M. Okkerse, C.R. Kleijn, H.E.A. van der Akker, M.H.J.M. de Croon, G.B. Marin, Two-dimensional simulation of an oxy-acetylene torch diamond reactor with a detailed gas-phase and surface mechanism, *J. Appl. Phys.* 88 (2000) 4417.
- [28] K.K. Höinghaus, A. Löwe, B. Atakan, Investigations of the gas phase mechanism of diamond deposition in combustion CVD, *Thin Solid Films* 368 (2000) 185–192.
- [29] K.D. Esmeryan, C.E. Castano, A.H. Bressler, C.P. Fergusson, R. Mohammadi, Single-step flame synthesis of carbon nanoparticles with tunable structure and chemical reactivity, *RSC Adv.* 6 (2016) 61620–61629.
- [30] R.Z. Khaliullin, H. Eshet, T.D. Kühne, J. Behler, M. Parrinello, Nucleation mechanism for the direct graphite-to-diamond phase transition, *Nat. Mater.* 10 (2011) 693–697.
- [31] V.N. Mochalin, O. Shenderova, D. Ho, Y. Gogotsi, The properties and applications of nanodiamonds, *Nat. Nanotechnol.* 7 (2012) 11–23.
- [32] Z. Su, W. Zhou, Y. Zhang, New insights into the soot nanoparticles in a candle flame, *Chem. Commun.* 47 (2011) 4700–4702.
- [33] W.Z. Zhou, F.J. Yu, H.F. Greer, Z. Jiang, P.P. Edwards, Electron microscopic studies of growth of nanoscale catalysts and soot particles in a candle flame, *Appl. Petrochem. Res.* 2 (2012) 15–21.
- [34] M. Choucair, J.A. Stride, The gram-scale synthesis of carbon onions, *Carbon* 50 (2012) 1109–1115.
- [35] J.C. Vinci, L.A. Colon, Fractionation of carbon-based nanomaterials by anion-exchange HPLC, *Anal. Chem.* 84 (2012) 1178–1183.
- [36] N.A. Marks, M. Lattemann, D.R. McKenzie, Nonequilibrium route to nanodiamond with astrophysical implications, *Phys. Rev. Lett.* 108 (2012) 075503.
- [37] G. Anastopoulos, Y. Zannikou, S. Stourmas, S. Kalligeros, Transesterification of vegetable oils with ethanol and characterization of the key fuel properties of ethyl esters, *Energies* 2 (2009) 362–376.
- [38] K.D. Esmeryan, E.I. Radeva, I.D. Avramov, Durable superhydrophobic carbon soot coatings for sensor applications, *J. Phys. D: Appl. Phys.* 49 (2016) 025309.
- [39] A. Sadezky, H. Muchkenhuber, H. Grothe, R. Niessner, U. Pöschl, Raman microspectroscopy of soot and related carbonaceous materials: spectral analysis and structural information, *Carbon* 43 (2005) 1731–1742.
- [40] A.C. Ferrari, J. Robertson, Interpretation of Raman spectra of disordered and amorphous carbon, *Phys. Rev. B* 61 (2000) 14095–14107.
- [41] A. Kumar, P.A. Lin, A. Xue, B. Hao, Y.K. Yap, R.M. Sankaran, Formation of nanodiamonds at near-ambient conditions via microplasma dissociation of ethanol vapour, *Nat. Commun.* 4 (2013) 2618.
- [42] R. Sonnier, B. Otazaghine, L. Ferry, J.M.L. Cuesta, Study of the combustion efficiency of polymers using a pyrolysis-combustion flow calorimeter, *Combust. Flame* 160 (2013) 2182–2193.
- [43] T.X. Li, K. Kuwana, K. Saito, H. Zhang, Z. Chen, Temperature and carbon source effects on methane-air flame synthesis of CNTs, *Proc. Combust. Inst.* 32 (2009) 1855–1861.
- [44] O.I. Smith, Fundamentals of soot formation in flames with application to diesel engine particulate emissions, *Prog. Energy Combust. Sci.* 7 (1981) 275–291.
- [45] K. Higashi, A. Onodera, Non-catalytic synthesis of diamond from amorphous carbon at high static pressure, *Physica B + C* 139–140 (1986) 813–815.
- [46] J. Zhang, V. Prakapenka, A. Kubo, A. Kavner, H.W. Green, L.F. Dobrzhinetskaya, Diamond formation from amorphous carbon and graphite in the presence of COH fluids: an *in situ* high-pressure and -temperature laser-heated diamond anvil cell experimental study, in: L. Dobrzhinetskaya, S.W. Fariad, S. Wallis, S. Cuthbert (Eds.), *Ultrahigh-pressure Metamorphism*, Elsevier 2007, pp. 113–124.
- [47] K. Saito, A.S. Gordon, F.A. Williams, W.F. Stickley, A study of the early history of soot formation in various hydrocarbon diffusion flames, *Combust. Sci. Technol.* 80 (1991) 103–119.
- [48] J.F. Widmann, J.C. Yang, T.J. Smith, S.L. Manzello, G.W. Mulholland, Measurement of the optical extinction coefficients of post-flame soot in the infrared, *Combust. Flame* 134 (2003) 119–129.



# Rolling viscous drops on a non-wettable surface containing both micro- and macro-scale roughness

Mehran Abolghasemibizaki,<sup>1</sup> Connor J. Robertson,<sup>2</sup> Christian P. Fergusson,<sup>1</sup> Robert L. McMasters,<sup>2</sup> and Reza Mohammadi<sup>1,a)</sup>

<sup>1</sup>*Department of Mechanical and Nuclear Engineering, Virginia Commonwealth University, Richmond, Virginia 23284, USA*

<sup>2</sup>*Department of Mechanical Engineering, Virginia Military Institute, Lexington, Virginia 24450, USA*

(Received 21 November 2017; accepted 4 February 2018; published online 16 February 2018)

It has previously been shown that when a liquid drop of high viscosity is placed on a non-wettable inclined surface, it rolls down at a constant descent velocity determined by the balance between viscous dissipation and the reduction rate of its gravitational potential energy. Since increasing the roughness of the surface boosts its non-wetting property, the drop should move faster on a surface structured with macrot textures (ribbed surface). Such a surface was obtained from a superhydrophobic soot coating on a solid specimen printed with an extruder-type 3D printer. The sample became superoleophobic after a functionalization process. The descent velocity of glycerol drops of different radii was then measured on the prepared surface for varied tilting angles. Our data show that the drops roll down on the ribbed surface approximately 27% faster (along the ridges) than on the macroscopically smooth counterpart. This faster velocity demonstrates that ribbed surfaces can be promising candidates for drag-reduction and self-cleaning applications. Moreover, we came up with a modified scaling model to predict the descent velocity of viscous rolling drops more accurately than what has previously been reported in the literature. *Published by AIP Publishing.* <https://doi.org/10.1063/1.5016824>

## I. INTRODUCTION

Liquid-solid interaction has been studied for decades because of its involvement in many applications such as lubrication,<sup>1,2</sup> filtration,<sup>3–6</sup> surface cooling,<sup>7–9</sup> surface cleaning,<sup>10–13</sup> and liquid transportation.<sup>14–17</sup> Sometimes it is desired to prevent this interaction in certain applications; hence, the fabrication and implementation of the so-called non-wettable surfaces has been widely investigated by scientists over the past several years.<sup>12,13,18–25</sup> Generally, wettability of a solid surface associated with a particular liquid is assessed through the contact angle ( $\theta$ ) of the liquid drop deposited on the solid substrate.<sup>26</sup> The higher the contact angle, the more non-wettable the surface is. By definition, the surface is called superhydrophobic or superoleophobic if it makes a contact angle of greater than  $150^\circ$  with water or oil, respectively. It has been illustrated that such non-wettable surfaces demonstrate some exceptional properties such as anti-biofouling,<sup>18,19</sup> anti-corrosion,<sup>19–22</sup> drag-reduction,<sup>23,24</sup> and self-cleaning.<sup>12,13</sup> Most of these applications involve the movement of droplets on the surface that may not be straight.

Motion of a liquid drop on an inclined solid substrate generated by its own weight is a combination of rolling and sliding depending on the viscosity of the drop as well as the wettability of the substrate.<sup>27–29</sup> In fact, for high viscous liquids, the motion would be pure rolling with no slip-length<sup>28</sup> and if the liquid partially wets the surface, the larger drops run faster.<sup>29</sup> For the case of large viscosity and non-wettable

surfaces, Mahadevan and Pomeau claimed that the drop rolls down at an equilibrium descent velocity ( $V$ ).<sup>30</sup> They studied the motion of a liquid drop with viscosity ( $\mu$ ), surface tension ( $\gamma$ ), density ( $\rho$ ), and radius ( $R$ ) on a tilted plane at an angle of  $\alpha < 1$  radian (i.e.,  $< 57^\circ$ ) and proposed a scaling model to predict  $V$  by balance between viscous dissipation and the rate of decrease of the gravitational potential energy. Afterwards, Richard and Qu  r   experimentally examined this scaling model and showed for drops with radii smaller than the capillary length  $\kappa^{-1} = \sqrt{\frac{\gamma}{\rho g}}$  ( $g$  is the gravitational acceleration), the smaller the drop, the faster it rolls (something in contrast with the case of partially wettable surface). However, the provided equations were not able to accurately explain their presented results.<sup>31</sup> They also showed that the descent velocity is independent of the radius of the drop for  $R > \kappa^{-1}$ . In addition, Aussillous and Qu  r   obtained a liquid marble by rolling a liquid drop (mixture of water and glycerol with  $\mu > 200$  mPa s) in a hydrophobic powder and then studied its motion on an inclined solid surface.<sup>32</sup> Since the contact angle of the viscous liquid marble was close to  $180^\circ$ , they expressed the same explanation for the motion as Mahadevan and Pomeau did.<sup>30</sup> However, they showed that their equations were valid only for  $\alpha < 10^\circ$ .

The current paper presents a modified scaling model to predict the descent velocity of a rolling viscous drop much more accurately up to  $\alpha \sim 45^\circ$ . It is worth noting that the water motion, which is a mixture of rolling and sliding, should not be confused with the objective of the current study, i.e., rolling of glycerol (with a viscosity 1000-fold greater than that of water). Moreover, we show that a numerical coefficient is crucial in the related equations and must be considered because it reflects

<sup>a)</sup>Author to whom correspondence should be addressed: rmohammadi@vcu.edu. Telephone: (804)827-3997. Fax: (804)827-7030.

the non-wettability (i.e., contact angle) of the surface, something that is missing in the aforementioned studies. To do this systematically, we carefully examined the motion of glycerol drops with different radii rolling on a macroscopically smooth non-wettable surface, made of functionalized soot, at 6 different tilting angles. We also show that the drop rolls  $\sim 27\%$  faster if the tilting non-wettable surface is not macroscopically smooth but contains cylindrical ridges of hundreds of micrometers in diameter. This phenomenon might be due to the preserved air layers underneath the drop, which means this surface pattern/morphology (combination of nano/micro and macro roughness) may be useful in drag-reduction applications and self-cleaning surfaces.

## II. EXPERIMENTAL METHOD

### A. Sample preparation

Soot has been used in many studies as a superhydrophobic coating layer, yet the deposition and stabilizing processes have been varied.<sup>33–38</sup> In this study, we used the chimney-modified method of deposition<sup>35</sup> and functionalized the soot as explained in detail in our previous study.<sup>38</sup> In summary, exposing our solid substrates to the black fumes generated from our oil-based combustion unit,<sup>37</sup> at an air flow rate of  $0.0031 \text{ m}^3/\text{min}$ , provided a uniform layer of untreated soot coating. To improve the wettability and strength of the as-synthesized soot, we functionalized it using a method that was composed of dipping in ethanol (99%, Sigma-Aldrich, USA) for 5 s (ethanol treatment), followed by perfluorocarbon treatment consisting of immersion in a solution of 12.5 wt. % perfluorocarbon (Granger's Performance Proofer, Granger's Ltd., UK) and 87.5 wt. % de-ionized (DI) water for 10 min.

It has been shown that for the relatively thick soot layers, synthesized using the method that we previously developed and used here, the material of the solid substrate (glass, polymer, or metal) has no effect on the wettability and characterization of the coating.<sup>35,36</sup> As such, the solid substrates used for wetting characterization of the coating were  $25 \times 25 \text{ mm}$  glass slides (Fisher Scientific, USA). For the rolling-drop experiments, two rectangular prisms of  $50 \times 50 \times 10 \text{ mm}$  were printed in polyethylene terephthalate glycol-modified (PETG) using an extruder-type 3D printer (Ultimaker 2, Netherlands) with a nozzle of  $0.4 \text{ mm}$  in diameter and the speed of  $12 \text{ mm/s}$ . One of the specimens was used with its original surface finish after printing, fully covered with cylindrical ridges of  $2b = 300 \text{ }\mu\text{m}$  in diameter (ribbed surface) with the resolution of about  $5 \text{ }\mu\text{m}$ . The other one was polished with 600 and 1200 grit sand papers (Allied High Tech Products, Inc., USA) to obtain a surface with no macroscopic-sized textures, which we call smooth surface. Prior to the soot deposition, both surfaces were cleaned with a detergent and then sonicated in water-ethanol solution for 30 min.

Four different liquids, water, diiodomethane, glycerol, and olive oil were used for studying the wettability and surface energy of our non-wettable coating. For the rolling droplet experiments, only glycerol, whose viscosity is sufficiently high, was used.

### B. Surface free energy examination

Soot has previously been used as a template to fabricate superamphiphobic coatings.<sup>33</sup> The synthesis of such surfaces, however, includes chemical vapor deposition followed by calcination at  $600 \text{ }^\circ\text{C}$ , which constrains its applicability. The fabrication process of the functionalized soot presented here, and in our previous study,<sup>38</sup> can be applied on any type of solid substrate even with low thermal stability such as plastic and wood. Recently, our research group has shown that ethanol treatment reduces the porosity and thickness of the soot layer so that its robustness improves significantly.<sup>36,39</sup> Here we examined how ethanol and perfluorocarbon treatments change the surface free energy and water/oil repellency of the soot.

Theoretically, contact angle ( $\theta$ ) of a sessile liquid drop on a solid surface correlates the surface free energy of the solid ( $\gamma_s$ ), the energy of the solid-liquid interface ( $\gamma_{sl}$ ), and the surface tension of the liquid ( $\gamma_l$ ) through Young's equation [Eq. (1a)].<sup>40</sup>  $\theta$  and  $\gamma_l$  can experimentally be measured, which we did using a Drop Shape Analyzer (DSA-25E, KRÜSS, Germany); thus, having an additional equation for  $\gamma_{sl}$  makes it mathematically possible to determine  $\gamma_s$ . It is known that  $\gamma_s$  and  $\gamma_l$  are the summation of their own dispersive and polar components, denoted with superscript  $d$  and  $p$  in Eqs. (1b) and (1c), respectively.<sup>41–43</sup> The permanent dipoles, induced dipoles, and hydrogen bond forces are responsible for the polar component, whereas the non-polar van der Waals forces are the origin of the dispersive component<sup>43</sup>

$$\gamma_s - \gamma_{sl} = \gamma_l \cos \theta, \quad (1a)$$

$$\gamma_s = \gamma_s^d + \gamma_s^p, \quad (1b)$$

$$\gamma_l = \gamma_l^d + \gamma_l^p. \quad (1c)$$

The solid-liquid interaction, i.e.,  $\gamma_{sl}$ , is directly related to the extent of polarity and non-polarity of the solid and the liquid. Using the geometric mean, Owens and Wendt proposed an equation for  $\gamma_{sl}$ .<sup>41</sup> Alternatively, Wu claimed that for low-energy surfaces, the harmonic mean should be used to obtain  $\gamma_{sl}$ , as expressed in the following equation:<sup>42</sup>

$$\gamma_{sl} = \gamma_s + \gamma_l - 4 \frac{\gamma_s^d \gamma_l^d}{\gamma_s^d + \gamma_l^d} - 4 \frac{\gamma_s^p \gamma_l^p}{\gamma_s^p + \gamma_l^p}. \quad (2)$$

Substituting Eq. (2) into Eq. (1a) yields Eq. (3),

$$\frac{\gamma_l (1 + \cos \theta)}{4} = \frac{\gamma_s^d \gamma_l^d}{\gamma_s^d + \gamma_l^d} + \frac{\gamma_s^p \gamma_l^p}{\gamma_s^p + \gamma_l^p}. \quad (3)$$

According to Eq. (3), the dispersive and polar components of the solid surface can be calculated by measuring the contact angle of two liquids whose  $\gamma_l^d$  and  $\gamma_l^p$  are known. Here, a non-polar liquid (diiodomethane, Fisher Scientific, USA) and a relatively polar one (water), whose surface tension components are presented in Table I,<sup>43</sup> were used to calculate the surface energy of the untreated soot (as-synthesized), the ethanol-treated soot, the perfluorocarbon-treated soot, and the functionalized (ethanol-treated followed by perfluorocarbon treatment) soot coatings.

TABLE I. Surface tension components of the liquids used to evaluate surface energy of the four solid surfaces studied. We have measured the total surface tension values (second column) in our experiments, while their contributing components (third and fourth columns) have been estimated by consulting Ref. 43.

Liquid	$\gamma_l$ (mN/m)	$\gamma_l^d$ (mN/m)	$\gamma_l^p$ (mN/m)
Water (H <sub>2</sub> O)	72.8	21.8	51.0
Diiodomethane (CH <sub>2</sub> I <sub>2</sub> )	48.5	48.5	0.0

### C. Rolling drop setup

Glycerol (99%, Acros Organics, USA) of density  $\rho = 1261 \text{ kg/m}^3$ , surface tension  $\gamma = 64.6 \pm 0.1 \text{ mN/m}$ , and viscosity  $\mu = 1076 \pm 5 \text{ mPa s}$  at  $23^\circ \text{C}$  was used as the viscous liquid. The surface tension and viscosity were measured by means of our DSA-25E and a rheometer (MCR301, Anton Paar, USA), respectively. Using a precisely controlled automated syringe and calibrated tips, glycerol drops of volume  $6\text{--}116 \mu\text{l}$  were formed with  $<5\%$  error. The drops were gently placed on the non-wettable smooth and ribbed surfaces tilted at 6 different angles ( $\alpha \sim 5^\circ\text{--}45^\circ$ ) and allowed to roll down under the influence of their own weights. The tilting angles were made by a stepper motor controlled by an Arduino microcontroller and were confirmed by a digital level (DWL-80e, Digi-Pas, USA).

Using a high-speed camera (Phantom Miro ex2, Ametek, USA), the motion of the glycerol drops was filmed at 1200 frames/s (fps) at first. After analyzing the videos via Tracker open-source computer software, it was found that 1200 fps was unnecessarily high; therefore, the frame rates were adjusted accordingly from 120 to 600 fps. Each test was repeated three

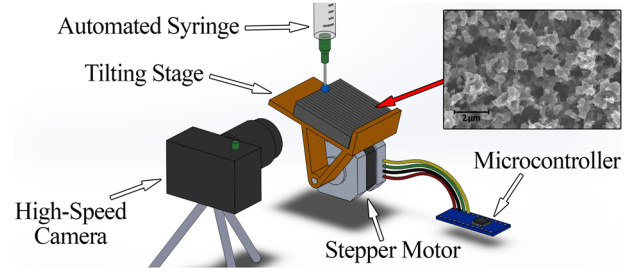


FIG. 1. The schematic diagram of the experimental setup. The inset is a scanning electron microscopy (SEM) image of a functionalized soot coating that illustrates its nano-/micro-sized roughness.

times and the measured velocities fluctuated  $<5\%$ . All the experiments were conducted at  $\sim 23^\circ \text{C}$  and  $\sim 38\%$  relative humidity. Figure 1 shows the schematic diagram of the experimental setup as well as the roughness of the functionalized soot coating.

## III. RESULTS AND DISCUSSION

### A. Wettability and surface free energy of the soot-based coatings

Table II states the measured contact angles of water ( $\rho = 1000 \text{ kg/m}^3$ ,  $\gamma = 72.8 \pm 0.2 \text{ mN/m}$ ), diiodomethane ( $\rho = 3322 \text{ kg/m}^3$ ,  $\gamma = 48.5 \pm 0.3 \text{ mN/m}$ ), glycerol ( $\rho = 1261 \text{ kg/m}^3$ ,  $\gamma = 64.6 \pm 0.1 \text{ mN/m}$ ), and olive oil ( $\rho = 930 \text{ kg/m}^3$ ,  $\gamma = 33.1 \pm 0.1 \text{ mN/m}$ ) on the four solid substrates investigated. It should be noted that drops with a volume of  $\sim 5 \mu\text{l}$  were used for water, glycerol, and olive oil. For diiodomethane, however,  $\sim 1 \mu\text{l}$  drops were used due to its high density and

TABLE II. Contact angle values of water, diiodomethane, glycerol, and olive oil on untreated soot, ethanol-treated soot, perfluorocarbon-treated soot, and functionalized soot.

Solid surface	Water (deg)	Diiodomethane (deg)	Glycerol (deg)	Olive oil (deg)
Soot (untreated)	$155.1 \pm 1.5$	$\sim 0.0$	$147.1 \pm 2.4$	$\sim 0.0$
Ethanol-treated soot	$147.7 \pm 2.4$	$\sim 0.0$	$127.8 \pm 0.9$	$\sim 0.0$
Perfluorocarbon-treated soot	$168.1 \pm 1.4$	$103.9 \pm 4.5$	$167.6 \pm 1.8$	$153.8 \pm 1.1$
Functionalized soot	$166.8 \pm 0.9$	$105.0 \pm 4.4$	$169.1 \pm 1.3$	$157.5 \pm 0.9$

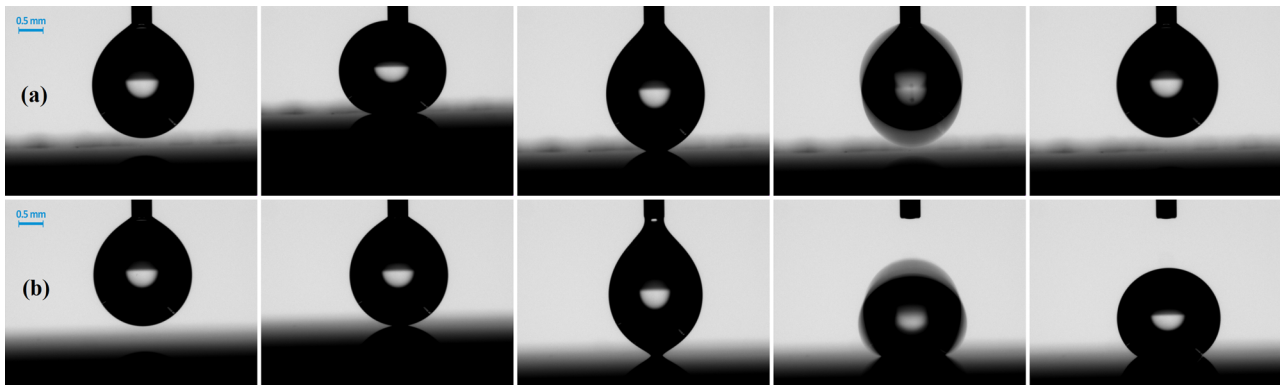


FIG. 2. (a) The top row from left to right shows that the un-treated soot cannot detach a  $5 \mu\text{l}$  water drop from the needle of  $0.2 \text{ mm}$  inside diameter due to its Cassie-Baxter state of wetting. (b) The bottom row illustrates how the same size drop sticks to the ethanol-treated soot as soon as it touches the surface (Wenzel state).

TABLE III. The results of surface energy calculations for the different types of soot-based coatings. The values were obtained using Eq. (3) and the data presented in Tables I and II.

Solid surface	$\gamma_s$ (mJ/mm <sup>2</sup> )
Soot (untreated)	37.9
Ethanol-treated soot	38.6
Perfluorocarbon-treated soot	5.2
Functionalized soot	5.0

low surface tension. The contact angles were measured on the macroscopically smooth samples (without ribs).

Since diiodomethane and olive oil (non-polar liquids<sup>43,44</sup>) spread instantly on both the soot and ethanol-treated soot coatings (Table II and Fig. S1 of the [supplementary material](#)), it is concluded that the ethanol treatment does not change the non-polarity of the soot. However, since the ethanol treatment makes the soot denser and reduces its porosity,<sup>36,39</sup> the contact angles of water and glycerol (polar liquids<sup>45</sup>) on the ethanol-treated soot are smaller than those on the untreated soot. Moreover, Fig. 2(a) shows how a 5  $\mu$ l water drop suspended from a needle (of 0.2 mm inside diameter) cannot be detached by the untreated soot, while the ethanol-treated soot detaches the drop from the needle easily [Fig. 2(b)]. This also illustrates that this treatment alters the wetting state of the soot from Cassie-Baxter to Wenzel regime.

According to the data of Table II, the interaction with perfluorocarbon solution drastically changes the wettability of the coating so that it repels both polar and non-polar liquids,

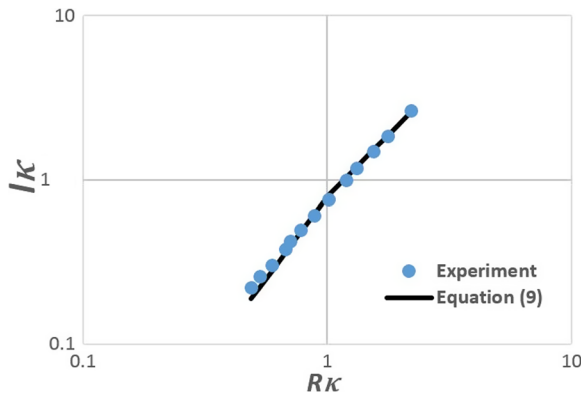


FIG. 3. The radius ( $l$ ) of the solid-liquid contact area for glycerol drops of different initial radii ( $R$ ) sitting on the horizontal macroscopically smooth, non-wettable surface. Both values were normalized with the capillary length  $\kappa^{-1} = \sqrt{\gamma/\rho g} = 2.27$  mm.

which means that the surface energy of the coating must have become very low. The surface energies of the solid surfaces were calculated using Eq. (3) and casting the mean value of the contact angles of water and diiodomethane presented in Table II and their surface tension components listed in Table I. Table III shows that the calculated surface energy reduces drastically from 37.9 mJ/mm<sup>2</sup> for the soot and 38.6 mJ/mm<sup>2</sup> for the ethanol-treated soot to 5.2 mJ/mm<sup>2</sup> for perfluorocarbon-treated soot and 5.0 mJ/mm<sup>2</sup> for functionalized soot, respectively, due to the generation of a fluorine-based layer on top of the coatings.<sup>36,39</sup> Such a low surface energy results in the oil repellency of the functionalized soot coating with the contact angle hysteresis of  $\sim 0.9^\circ$  for glycerol and makes the surface a great candidate for the rolling drop test (no liquid pinning).

## B. Rolling viscous drop

The motion of glycerol ( $\rho = 1261$  kg/m<sup>3</sup>,  $\gamma = 64.6 \pm 0.1$  mN/m, and  $\mu = 1076 \pm 5$  mPa.s) drops on the polished PETG sample (smooth surface) coated with functionalized soot and inclined at 6 different angles ( $\alpha = 5^\circ$ – $45^\circ$ ) was investigated here in order to find the modified scaling model for predicting their descent velocities. Considering the case of a small liquid drop ( $R < \kappa^{-1}$ ) sitting on a horizontal non-wettable solid surface, the capillary forces endeavor to keep the spherical shape of the drop whereas gravity tends to increase the solid-liquid contact area. Mahadevan and Pomeau<sup>30</sup> stated that the radius of the contact disk ( $l$ ) is related to the radius of the drop ( $R$ ) and the displacement of the center of mass of the drop ( $\delta$ ) due to its weight as

$$l \approx \sqrt{R\delta}. \quad (4)$$

As the drop is almost spherical except in the vicinity of the substrate, they explained geometrically that the increase in the surface area of the drop due to flattening because of contact with the substrate is in the order of  $\Delta s \approx l^4/R^2$ .<sup>30</sup> Therefore, balancing the increase in the surface energy  $\gamma\Delta s \approx \gamma l^4/R^2$  and the decrease in the potential energy of the drop  $\rho R^3 g \delta$  yields the expression for  $\delta$  as

$$\delta \approx \rho g R^3 / \gamma. \quad (5)$$

Finally, substituting Eq. (5) into Eq. (4) results in

$$l \approx R^2 / \kappa^{-1}, \quad (6)$$

where  $\kappa^{-1}$  is capillary length, as mentioned earlier ( $\kappa^{-1} = \sqrt{\gamma/\rho g}$ ). For the case of  $R > \kappa^{-1}$ , gravity dominates the surface tension and flattens the drop to a pancake shape. Since the thickness of the pancake ( $w$ ) scales with the capillary length

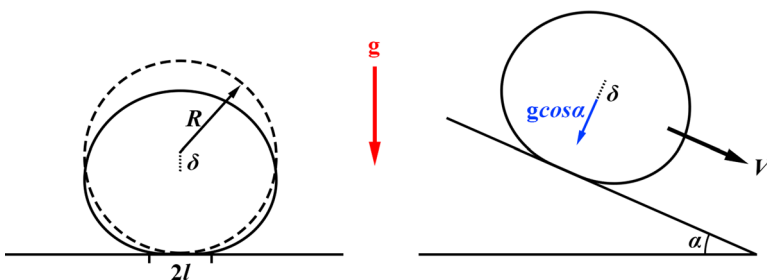


FIG. 4. For the case of the rolling drop on a tilted surface at the angle of  $\alpha$ ,  $\delta$  is a consequence of the normal component of gravity to the surface.



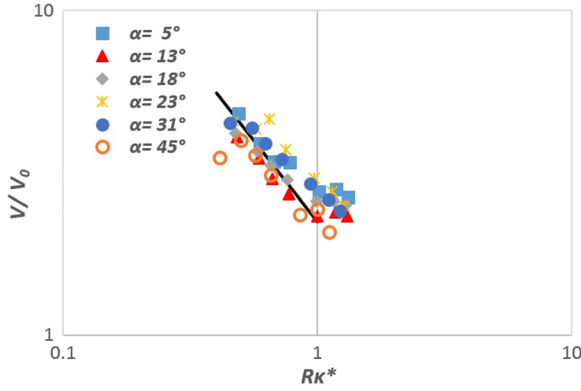


FIG. 5. The normalized velocity of the rolling drops as a function of their normalized radii for the 6 different tilting angles  $\alpha = 5^\circ$ – $45^\circ$  tested in this study. The solid black line represents  $\frac{V}{V_0} = 2.23 \frac{\kappa^{*-1}}{R}$ .

( $\kappa^{-1}$ ), conservation of mass ( $l^2 w \sim R^3$ ) concludes that the radius of the contact scales as

$$l \approx R^{3/2} / \kappa^{-1/2}. \quad (7)$$

One approach to estimate the numerical coefficients of Eqs. (6) and (7), which have to be the same, is to use the conservation of mass for flattened heavy drops. It is well established that the thickness of the flattened drop due to its own weight is:  $w = \sqrt{2(1 - \cos \theta)} \kappa^{-1}$ .<sup>31,46,47</sup> For non-wettable surfaces, where  $\theta > 150^\circ$ , the height can be considered  $w \approx 2\kappa^{-1}$ . Casting this value in the conservation of mass, which is  $\rho \pi l^2 w = \rho \frac{4\pi}{3} R^3$ , results in

$$l \approx \sqrt{\frac{2}{3} \frac{R^3}{\kappa^{-1}}} = 0.81 R^{3/2} / \kappa^{-1/2}. \quad (8)$$

Moreover, it has been reported that numerically solving the Laplace equation yields a numerical coefficient in the order of 0.8.<sup>32</sup> We measured the contact radius of the glycerol drop on the smooth (non-wettable) surface, which was horizontally oriented, as a function of its initial radius. The best numerical coefficient for Eqs. (6) and (7) to fit our data was found to be 0.79 using a least-squares fit of the data shown in Fig. 3; thus, the contact radius can be calculated from Eq. (9) for our experiments.

$$\begin{cases} l = 0.79 R^2 \kappa & \text{for } R < \kappa^{-1} \\ l = 0.79 R^{\frac{3}{2}} \kappa^{\frac{1}{2}} & \text{for } R > \kappa^{-1} \end{cases}. \quad (9)$$

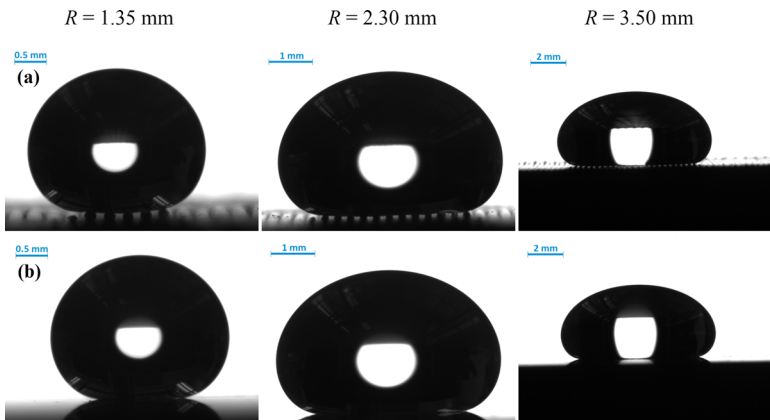


FIG. 6. Glycerol drops of different radii deposited on (a) ribbed and (b) smooth surfaces. The capillary length for glycerol is  $\sim 2.27$  mm.

For the case of small drops ( $R < \kappa^{-1}$ ) rolling down an inclined non-wettable surface with Stokes flow ( $Re = \rho V R / \mu < 1$ ), low velocity ( $Ca = \mu V / \gamma < 1$ ), and little change in the spherical shape of the drops, Mahadevan and Pomeau<sup>30</sup> claimed that the rate of decrease in the gravitational potential energy [LHS in Eq. (10)] balances with the viscous dissipation [RHS in Eq. (10)]. This happens in the portion of the volume of the rolling drop influenced by the contact region,  $\sim l^3$ , as

$$\rho R^3 g V \sin \alpha \approx \mu \left( \frac{V}{R} \right)^2 l^3. \quad (10)$$

Solving Eq. (10) for  $V$  and substituting Eq. (6) in it, Richard and Quéré came up with an equation to predict the descent velocity of a rolling droplet.<sup>31</sup> Using their equation, which is related to  $\sin \alpha$  and  $\kappa^{-1}$ , and plotting the normalized values of the measured velocities of the rolling drops with different radii for the varied tilting angles of our study (Fig. S2 of the [supplementary material](#)), we noticed that the data did not correlate on a single plot, similar to what Richard and Quéré found in their study, but did not address. This means that a key factor has been missing in the related equations and the scaling model needs to be modified.

As explained earlier, Eq. (5) for  $\delta$  is obtained with the balance between the increase in the surface energy by  $\gamma l^4 / R^2 \approx \gamma \delta^2$  and the decrease in the potential energy of the drop by  $\rho R^3 g \delta$  generated by its own weight. For a rolling drop on an inclined surface, the displacement of the center of mass caused by the *normal* component of gravity should be considered (see Fig. 4); hence, the reduction in the potential energy is  $\rho R^3 g \delta \cos \alpha$ . Consequently,  $\delta \approx \rho g R^3 \cos \alpha / \gamma$  and

$$l \approx R^2 / \kappa^{*-1}, \quad \text{where } \kappa^{*-1} = \sqrt{\gamma / \rho g \cos \alpha}. \quad (11)$$

The modified scaling model to predict the descent velocity of a rolling viscous drop on a non-wettable solid substrate tilted at an angle of  $\alpha$  is obtained by combining Eqs. (10) and (11) as

$$V \approx \frac{\rho R^5 g \sin \alpha}{\mu l^3} = \frac{\gamma}{\mu} \frac{\kappa^{*-1}}{R} \tan \alpha. \quad (12)$$

According to Eq. (12), when the radius of the drop reaches the critical value of  $\kappa^{*-1}$ , the velocity reaches the value of  $V_0 = \frac{\gamma}{\mu} \tan \alpha$ . Figure 5 shows that all the normalized velocities of the rolling drops ( $V/V_0$ ) with respect to their normalized

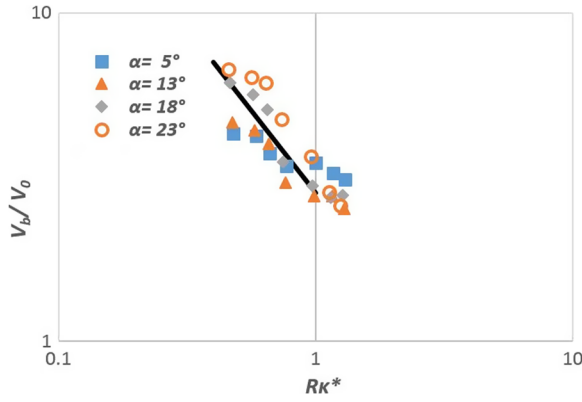


FIG. 7. The plot depicts the normalized velocity of the rolling drops versus their normalized radii on the ribbed surface for varied tilting angles ( $\alpha$ ). The solid black line represents  $\frac{V_b}{V_0} = 2.83 \frac{\kappa^{*-1}}{R}$ .

sizes ( $R\kappa^*$ ) collapse into a single plot with the numerical coefficient of 2.23 for the 6 different tilting angles tested in this work. The reason that our Eq. (12) fits better with the experimental data is its dependence to  $\tan \alpha$  and  $\kappa^{*-1}$ , whereas to  $\sin \alpha$  and  $\kappa^{-1}$  as expressed in Refs. 30–32. Moreover, since  $V \propto \frac{1}{l^3}$ , it can be speculated that the numerical coefficient for Eq. (11) must have been  $1/\sqrt[3]{2.23} = 0.77$ , a value indeed close to what we found for Eq. (9). Moreover, since the thickness ( $w$ ) of a flattened heavy drop is independent of its size<sup>31,46,47</sup> and the velocity gradient scales as  $V/w$  in its entire volume  $\propto R^3$  [instead of  $V/R$  and  $\propto l^3$  for small drops in Eq. (10)<sup>30</sup>], the velocity is independent of the radius of the drop for  $R > \kappa^{*-1}$ , similar to what has been reported in Refs. 31 and 32.

We also measured the contact radius of the glycerol drops deposited on the non-wettable, ribbed surface, fully decorated with cylindrical ridges of  $2b = 300 \mu\text{m}$  diameter. It turns out that Eq. (9) is also valid for this surface. Figure 6 illustrates how drops of different radii sit on (a) ribbed and (b) smooth samples.

The reflection of light underneath the drops on the ribbed surface illustrates that this surface pattern keeps macroscopic air pockets beneath the drop. When the drop rolls on such a surface, it encounters either the air pocket or the solid substrate. The relation between the probability of air ( $P_a$ ) and the solid ( $P_s$ ) surface being in contact with the rolling drop can be geometrically found from the following equations:

$$\frac{P_s}{P_a} = \frac{\frac{\pi}{2}b^2}{2b^2 - \frac{\pi}{2}b^2} = 3.7, \quad (13a)$$

$$P_s + P_a = 1. \quad (13b)$$

Hence  $P_s = 0.79$  and  $P_a = 0.21$ . This means that the area of contact between solid and liquid reduces to  $\sim 79\%$  on such a surface pattern compared to the smooth one. As explained earlier, since viscous dissipation occurs in the part of the volume ( $\sim l^3$ ) of the rolling drop influenced by the contact region, the velocity is proportional to  $\frac{1}{l^3}$ . Considering the fact that this partial volume of the rolling drop on the ribbed surface is  $\sim 79\%$  of that on the smooth one, the relation between the descent velocity of an equivalent-sized drop on ribbed ( $V_b$ ) and smooth ( $V_s$ ) surfaces will be  $\frac{V_b}{V_s} \approx \frac{1}{0.79} \approx 1.27$ . We measured the descent velocity of rolling glycerol drops on the ribbed surface under the same conditions as for the smooth surface. Figure 7 shows that the normalized velocities of the rolling drops (along the axis of the cylindrical ridges) concur well with the modified scaling model, yet with a numerical coefficient of 2.83, which is indeed 27% higher than that of the smooth surface. This means that the droplet rolls down faster on the ribbed surface due to the air pockets shown in Fig. 6. It should also be mentioned that the drops almost instantly rolled at the associated descent velocity on the smooth surface, whilst their motions were slightly accelerated on the ribbed surface before reaching  $V_b$  especially for higher  $\alpha$ . For instance, the 50 mm length of our samples was not long enough for the drops to reach an equilibrium descent velocity when they were rolling along the ridges at a  $31^\circ$ -tilted angle; thus, the data have not been presented here.

In addition, we measured the descent velocity of the drops rolling perpendicular to the ridges and found a numerical coefficient of 2.53 for such rolling (Fig. S3 of the [supplementary material](#)). This value is still 13% higher than that of the smooth surface but not comparable to 27% that was obtained for the case of rolling droplets along the ridges. This may be attributed to the fact that when the drop rolls perpendicular to the ridges, the ridges play a barrier role and hinder the motion.<sup>48</sup> Interestingly, we found that the skin patterns of a human being's palm, the sole of the foot, and the finger print look similar to the ribbed pattern as shown in Fig. 8. This similarity, along with the faster motion of liquid drops on the ribbed surface, shows that this surface pattern may be useful in designing enhanced self-cleaning surfaces.

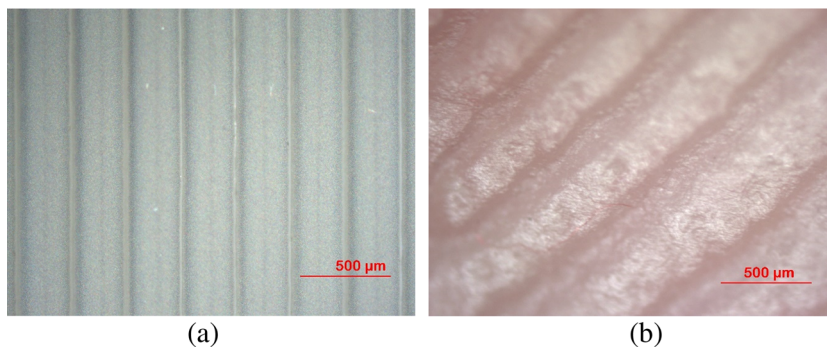


FIG. 8. (a) The image of ribbed surface coated with functionalized soot and (b) skin pattern of the fingertip, taken using a Axio Lab optical microscope (Zeiss, Germany).

## IV. CONCLUSIONS

In this paper, first the wettability of chimney-modified soot coating was investigated by measuring the contact angles of polar (water and glycerol) and non-polar (diiodomethane and olive oil) liquids before and after its interaction with ethanol and perfluorocarbon solutions. It was shown that the ethanol treatment increases the surface energy of the soot, yet does not alter its non-polar nature. Moreover, the perfluorocarbon treatment generates a fluorine-based layer on top of the soot and reduces its surface energy down to  $\sim 5.0$  mJ/mm<sup>2</sup>. This functionalized soot coating with such a low surface energy demonstrated oil repellency with contact angles of  $\sim 157.5^\circ$  for olive oil and  $\sim 169.1^\circ$  for glycerol.

Second, the motion of glycerol drops with different sizes rolling down on the non-wettable smooth and ribbed surfaces at 6 different angles of tilt was studied and a modified scaling model was given to predict the descent velocity more accurately, Eq. (12). The experimental results exhibited a good agreement with this modified scaling model, even for a tilting angle as high as  $\sim 45^\circ$ . Moreover, it was shown that the drops roll  $\sim 27\%$  faster (along the ridges) on the ribbed surface compared to the smooth one due to the preserved air pockets underneath the drops. This indicates that a ribbed surface pattern may be valuable in designing enhanced self-cleaning surfaces.

## SUPPLEMENTARY MATERIAL

See [supplementary material](#) for figures that show instant spreading of non-polar liquids on soot, data not collapsing to a single plot after normalization, and data for drops rolling down perpendicular to ridges.

## ACKNOWLEDGMENTS

The authors gratefully acknowledge Mr. Karam Nashwan Al Milaji and Dr. Hong Zhao for their assistance in measuring the viscosity of glycerol. In addition, we thank Mr. Austin Reid for his help with 3D-printing the rectangular prisms and Dr. Carlos Castano for his aid with taking the SEM image at VCU-NCC. The Dissertation Assistantship Award (M.A.) and the startup Grant No. 137422 (R.M.) from Virginia Commonwealth University as well as the VMI Summer Undergraduate Research Institute grant (C.J.R.) are gratefully acknowledged for financially supporting this work.

<sup>1</sup>E. Omrani, B. Barari, A. D. Moghadam, P. K. Rohatgi, and K. M. Pillai, "Mechanical and tribological properties of self-lubricating bio-based carbon-fabric epoxy composites made using liquid composite molding," *Tribol. Int.* **92**, 222 (2015).

<sup>2</sup>B. Barari, E. Omrani, A. D. Moghadam, P. L. Menezes, K. M. Pillai, and P. K. Rohatgi, "Mechanical, physical and tribological characterization of nano-cellulose fibers reinforced bio-epoxy composites: An attempt to fabricate and scale the 'Green' composite," *Carbohydr. Polym.* **147**, 282 (2016).

<sup>3</sup>H. R. Nejad, E. Samiei, A. Ahmadi, and M. Hoorfar, "Gravity-driven hydrodynamic particle separation in digital microfluidic systems," *RSC Adv.* **5**, 35966 (2015).

<sup>4</sup>M. Davoudi, J. Fang, and G. Chase, "Barrel shaped droplet movement at junctions of perpendicular fibers with different orientations to the air flow direction," *Sep. Purif. Technol.* **162**, 1 (2016).

- <sup>5</sup>M. Amrei, M. Davoudi, G. Chase, and H. V. Tafreshi, "Effects of roughness on droplet apparent contact angles on a fiber," *Sep. Purif. Technol.* **180**, 107 (2017).
- <sup>6</sup>H. Nejad and M. Hoorfar, "Purification of a droplet using negative dielectrophoresis traps in digital microfluidics," *Microfluid. Nanofluid.* **18**, 483 (2015).
- <sup>7</sup>D. Khojasteh, S. M. Mousavi, and R. Kamali, "CFD analysis of Newtonian and non-Newtonian droplets impinging on heated hydrophilic and hydrophobic surfaces," *Indian J. Phys.* **91**, 513 (2017).
- <sup>8</sup>D. Khojasteh, A. Bordbar, R. Kamali, and M. Marengo, "Curvature effect on droplet impacting onto hydrophobic and superhydrophobic spheres," *Int. J. Comput. Fluid Dyn.* **31**, 310 (2017).
- <sup>9</sup>S. A. Mayer, R. G. Kowalski, M. Presciutti, N. D. Ostapovich, E. McGann, B.-F. Fitzsimmons, D. R. Yavagal, Y. E. Du, A. M. Naidech, and N. A. Janjua, "Clinical trial of a novel surface cooling system for fever control in neurocritical care patients," *Crit. Care Med.* **32**, 2508 (2004).
- <sup>10</sup>S. J. Kang, V. Vandadi, J. D. Felske, and H. Masoud, "Alternative mechanism for coffee-ring deposition based on active role of free surface," *Phys. Rev. E* **94**, 063104 (2016).
- <sup>11</sup>V. Vandadi, S. J. Kang, and H. Masoud, "Reciprocal theorem for convective heat and mass transfer from a particle in Stokes and potential flows," *Phys. Rev. Fluids* **1**, 022001 (2016).
- <sup>12</sup>Z. Yang, L. Wang, W. Sun, S. Li, T. Zhu, W. Liu, and G. Liu, "Superhydrophobic epoxy coating modified by fluorographene used for anti-corrosion and self-cleaning," *Appl. Surf. Sci.* **401**, 146 (2017).
- <sup>13</sup>W.-T. Cao, Y.-J. Liu, M.-G. Ma, and J.-F. Zhu, "Facile preparation of robust and superhydrophobic materials for self-cleaning and oil/water separation," *Colloids Surf., A* **529**, 18 (2017).
- <sup>14</sup>M. Paknahad, H. R. Nejad, and M. Hoorfar, "Development of a digital micropump with controlled flow rate for microfluidic platforms," *Sens. Transducers* **183**, 84 (2014).
- <sup>15</sup>M. K. D. Manshadi, D. Khojasteh, M. Mohammadi, and R. Kamali, "Electroosmotic micropump for lab-on-a-chip biomedical applications," *Int. J. Numer. Modell.: Electron. Networks, Devices Fields* **29**, 845 (2016).
- <sup>16</sup>J. Fang, M. Davoudi, and G. Chase, "Drop movement along a fiber axis due to pressure driven air flow in a thin slit," *Sep. Purif. Technol.* **140**, 77 (2015).
- <sup>17</sup>M. Soleimani, R. J. Hill, and T. G. van de Ven, "Bubbles and drops on curved surfaces," *Langmuir* **29**, 14168 (2013).
- <sup>18</sup>K. D. Esmerlyan, C. E. Castano, M. Abolghasemibizaki, and R. Mohammadi, "An artful method for *in-situ* assessment of the anti-biofouling potential of various functional coatings using a quartz crystal microbalance," *Sens. Actuators, B* **243**, 910 (2017).
- <sup>19</sup>Z. Wang, Y. Su, Q. Li, Y. Liu, Z. She, F. Chen, L. Li, X. Zhang, and P. Zhang, "Researching a highly anti-corrosion superhydrophobic film fabricated on AZ91D magnesium alloy and its anti-bacteria adhesion effect," *Mater. Charact.* **99**, 200 (2015).
- <sup>20</sup>Y. Wei, L. Hongtao, and Z. Wei, "Preparation of anti-corrosion superhydrophobic coatings by an Fe-based micro/nano composite electro-brush plating and blackening process," *RSC Adv.* **5**, 103000 (2015).
- <sup>21</sup>N. Wang, D. Xiong, Y. Deng, Y. Shi, and K. Wang, "Mechanically robust superhydrophobic steel surface with anti-icing, UV-durability, and corrosion resistance properties," *ACS Appl. Mater. Interfaces* **7**, 6260 (2015).
- <sup>22</sup>E.-C. Cho, C.-W. Chang-Jian, H.-C. Chen, K.-S. Chuang, J.-H. Zheng, Y.-S. Hsiao, K.-C. Lee, and J.-H. Huang, "Robust multifunctional superhydrophobic coatings with enhanced water/oil separation, self-cleaning, anti-corrosion, and anti-biological adhesion," *Chem. Eng. J.* **314**, 347 (2017).
- <sup>23</sup>S. Zhang, X. Ouyang, J. Li, S. Gao, S. Han, L. Liu, and H. Wei, "Underwater drag-reducing effect of superhydrophobic submarine model," *Langmuir* **31**, 587 (2014).
- <sup>24</sup>M. Davoudi, E. Moore, and G. Chase, "Motion of water drops on hydrophobic expanded polymer mat surfaces due to tangential air flow," *J. Taiwan Inst. Chem. Eng.* (published online).
- <sup>25</sup>Y. Zhan, M. Ruan, W. Li, H. Li, L. Hu, F. Ma, Z. Yu, and W. Feng, "Fabrication of anisotropic PTFE superhydrophobic surfaces using laser microprocessing and their self-cleaning and anti-icing behavior," *Colloids Surf., A* **535**, 8 (2017).
- <sup>26</sup>P.-G. De Gennes, F. Brochard-Wyart, and D. Quéré, *Capillarity and Wetting Phenomena: Drops, Bubbles, Pearls, Waves* (Springer Science & Business Media, 2013).
- <sup>27</sup>M. Reyssat, D. Richard, C. Clanet, and D. Quéré, "Dynamical superhydrophobicity," *Faraday Discuss.* **146**, 19 (2010).
- <sup>28</sup>S. P. Thampi, R. Adhikari, and R. Govindarajan, "Do liquid drops roll or slide on inclined surfaces?," *Langmuir* **29**, 3339 (2013).

- <sup>29</sup>B. S. Yilbas, A. Al-Sharafi, H. Ali, and N. Al-Aqeeli, "Dynamics of a water droplet on a hydrophobic inclined surface: Influence of droplet size and surface inclination angle on droplet rolling," *RSC Adv.* **7**, 48806 (2017).
- <sup>30</sup>L. Mahadevan and Y. Pomeau, "Rolling droplets," *Phys. Fluids* **11**, 2449 (1999).
- <sup>31</sup>D. Richard and D. Quéré, "Viscous drops rolling on a tilted non-wettable solid," *Europhys. Lett.* **48**, 286 (1999).
- <sup>32</sup>P. Aussillous and D. Quéré, "Liquid marbles," *Nature* **411**, 924 (2001).
- <sup>33</sup>X. Deng, L. Mammen, H.-J. Butt, and D. Vollmer, "Candle soot as a template for a transparent robust superamphiphobic coating," *Science* **335**, 67 (2012).
- <sup>34</sup>K. Seo and M. Kim, "Candle-based process for creating a stable superhydrophobic surface," *Carbon* **68**, 583 (2014).
- <sup>35</sup>K. D. Esmeryan, C. E. Castano, A. H. Bressler, M. Abolghasemibizaki, and R. Mohammadi, "Rapid synthesis of inherently robust and stable superhydrophobic carbon soot coatings," *Appl. Surf. Sci.* **369**, 341 (2016).
- <sup>36</sup>K. D. Esmeryan, A. H. Bressler, C. E. Castano, C. P. Fergusson, and R. Mohammadi, "Rational strategy for the atmospheric icing prevention based on chemically functionalized carbon soot coatings," *Appl. Surf. Sci.* **390**, 452 (2016).
- <sup>37</sup>K. D. Esmeryan, C. E. Castano, A. H. Bressler, M. Abolghasemibizaki, C. P. Fergusson, A. Roberts, and R. Mohammadi, "Kinetically driven graphite-like to diamond-like carbon transformation in low temperature laminar diffusion flames," *Diamond Relat. Mater.* **75**, 58 (2017).
- <sup>38</sup>M. Abolghasemibizaki and R. Mohammadi, "Droplet impact on superhydrophobic surfaces fully decorated with cylindrical macrottextures," *J. Colloid Interface Sci.* **509**, 422 (2018).
- <sup>39</sup>K. D. Esmeryan, C. E. Castano, and R. Mohammadi, "Interactions of superhydrophobic carbon soot coatings with short alkyl chain alcohols and fluorocarbon solutions," *Colloids Surf., A* **529**, 715 (2017).
- <sup>40</sup>T. Young, "An essay on the cohesion of fluids," *Philos. Trans. R. Soc. London* **95**, 65 (1805).
- <sup>41</sup>D. K. Owens and R. Wendt, "Estimation of the surface free energy of polymers," *J. Appl. Polym. Sci.* **13**, 1741 (1969).
- <sup>42</sup>S. Wu, *Calculation of Interfacial Tension in Polymer Systems* (Wiley Online Library, 1971).
- <sup>43</sup>S. Chiu, S.-J. Hwang, C. Chu, and D. Gan, "The influence of Cr-based coating on the adhesion force between epoxy molding compounds and IC encapsulation mold," *Thin Solid Films* **515**, 285 (2006).
- <sup>44</sup>M.-C. Michalski, S. Desobry, M.-N. Pons, and J. Hardy, "Adhesion of edible oils to food contact surfaces," *J. Am. Oil Chem. Soc.* **75**, 447 (1998).
- <sup>45</sup>S. Wu, *Polymer Interface and Adhesion* (M. Dekker, 1982).
- <sup>46</sup>F. Brochard-Wyart, H. Hervet, C. Redon, and F. Rondelez, "Spreading of 'heavy' droplets: I. Theory," *J. Colloid Interface Sci.* **142**, 518 (1991).
- <sup>47</sup>C. Extrand and S. I. Moon, "When sessile drops are no longer small: Transitions from spherical to fully flattened," *Langmuir* **26**, 11815 (2010).
- <sup>48</sup>X. Jiang and H. Z. Li, "Liquid drops hurdling barriers of various geometries," *Adv. Mater. Interfaces* **4**, 1700516 (2017).



## Parameter Estimation Involving Droplets on Flat and Cylindrical Non-wettable Surfaces

Mehran Abolghasemibizaki<sup>a</sup>, Connor J. Robertson<sup>b</sup>, Christian P. Fergusson<sup>a</sup>, Robert L. McMasters<sup>b</sup> and Reza Mohammadi<sup>a,\*</sup>

<sup>a</sup> Department of Mechanical and Nuclear Engineering, Virginia Commonwealth University, Richmond, VA, 23284, USA

<sup>b</sup> Department of Mechanical Engineering, Virginia Military Institute, Lexington, VA, 24450, USA

**Introduction:** Liquid-solid interaction has been the focus of many studies because of its wide applicability in areas such as surface cooling, energy conservation, lubrication, liquid transportation and microfluidic devices [1-7]. The research results presented here include two studies, one of which involves the equilibrium descent velocity of rolling viscous drops on tilted surfaces under the influence of gravity [8]. The other involves the impact of free-falling drops on a curved surface in an effort to determine the contact time when impacting the surface [9].

**First Experiment Description:** Glycerol droplets of seven radii ( $R = 1.11\text{-}3.00\text{ mm}$ ) were placed on a surface tilted at 6 different angles ( $\alpha = 5^\circ\text{-}45^\circ$ ) and the terminal descent velocities of the droplets were measured with a high-speed camera. This experiment is depicted schematically in Figure 1. The objective of the experiment is to develop a mathematical model to fit the data generated through the multiple experimental variations. It has been shown that, when a liquid drop of high viscosity (glycerol with viscosity of  $\mu = 1076 \pm 5\text{ mPa.s}$ ) is placed on a non-wettable inclined surface, it rolls down at a constant descent velocity ( $V$ ) since the viscous dissipation ( $\mu(\frac{V}{R})^2 l^3$ ) balances with the reduction rate of the gravitational potential energy ( $\rho R^3 g V \sin \alpha$ ) of the drop, where  $\rho$  is the density of the drop and  $l$  is the radius of the liquid-solid contact area, shown in Figure 1. Such a balance results in an interesting rule that the descent velocity is proportional to the reciprocal of the radius of the drop, i.e. the smaller the drop, the faster it rolls.

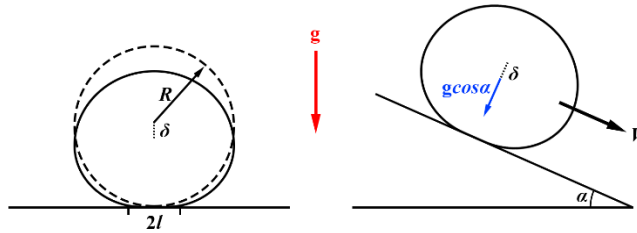


Figure 1. The schematic configuration of the rolling drop on a tilted surface at the angle of  $\alpha$ . The displacement of the center of mass of the drop ( $\delta$ ) is a consequence of the normal component of gravity to the surface.

The solid substrate used in this work became non-wettable after depositing a layer of soot and a chemical treatment afterwards, which is explained in detail in our previous papers [10-12]. Sitting on a horizontal non-wettable solid surface, the contact radius ( $l$ ) is determined by the balance between the capillary forces and gravity, such that the capillary forces endeavor to keep the spherical shape of the drop and exhibit smaller  $l$ , whereas the gravitational forces tend to flatten the drop and increase the solid-liquid contact area by shifting down the center of mass of

the drop. The measured terminal velocities for the various experimental conditions mentioned above were used in order to find a modified scaling model (Eq. 1a) for predicting such a descent velocity. Considering the fact that the displacement of the center of mass of the drop on the inclined surface is the consequence of the normal component of the gravity to the surface, the data was found to follow a common function as shown in Figure 2. In this functional fit, the numerical coefficient which correlates the normalized descent velocity ( $\frac{V}{V_o}$ ) to the normalized radius of the drop ( $\frac{\kappa^{*-1}}{R}$ ) is found to be  $2.23 \pm 0.63$  at a 95% confidence level. The descent velocity and the radius of the drop were normalized by a modified characteristic velocity and capillary length, as defined in Equation (1b) and (1c) respectively, in which  $\gamma$  is the surface tension of the liquid.

$$(a) \frac{V}{V_o} \approx \frac{\kappa^{*-1}}{R} \quad (b) V_o = \frac{\gamma}{\mu} \tan \alpha \quad (c) \kappa^{*-1} = \sqrt{\frac{\gamma}{\rho g \cos \alpha}} \quad (1)$$

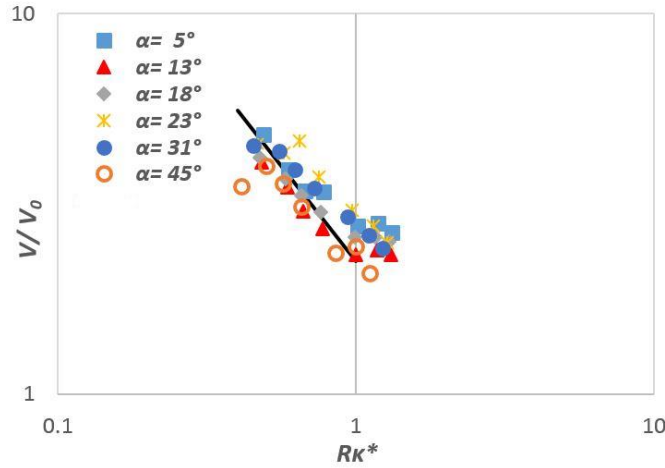


Figure 2. The plot shows that descent velocity of the rolling drop is proportional to the reciprocal of the radius of the drop and all the data points collapse into a single plot ( $\frac{V}{V_o} = 2.23 \frac{\kappa^{*-1}}{R}$  presented by the black line) after normalization.

**Second Experiment Description:** The other experiment involves the impact of water droplets on curved and ribbed-curved surfaces, observing the nature of the impact with a high-speed camera. Sample images from this set of experiments are shown in Figure 3. A previous numerical investigation [13] of this type of droplet impact claimed that the ratio of the radius of the curved surface ( $R$ ) to that of the drop ( $R_o$ ) is a critical factor that must be considered for contact time on curved surfaces. Hence the scaling model has been investigated here for five different radii ratios ( $R/R_o$ ) obtained from 6, 9, and 16  $\mu\text{L}$  droplets impacting surfaces with 9.0 and 12.7 mm diameters. For example, Figure 3 is associated with the impact of a 9  $\mu\text{L}$  droplet on a curved surface of  $R = 4.5$  mm at  $V = 1.0$  m/s ( $R/R_o = 3.49$ ).

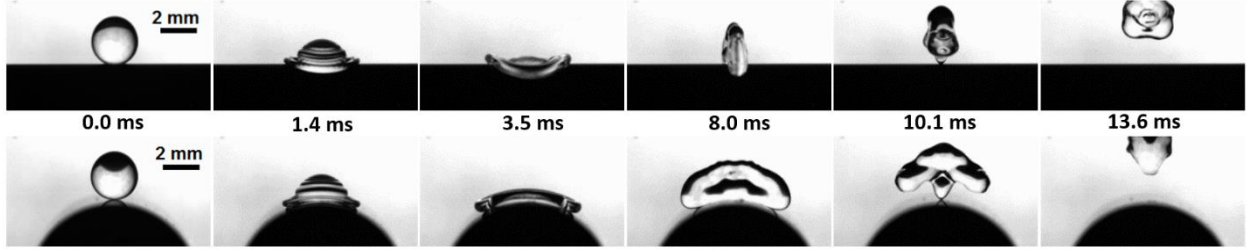


Figure 3. The top row shows the side view of a water droplet impacting a curved superhydrophobic surface and the bottom row shows the front view.

The contact times, composed of spreading and retraction times, of the five cases of impact were examined for various impact velocities ( $V$ ) and we found that the contact time changes with respect to  $V$  in the same manner that the retraction time does because the variability of the spreading time is negligible. For the scaling model the contact time is normalized by the inertial-capillary time scale  $\tau_o = \sqrt{\rho R_o^3 / \gamma}$  and the dimensionless Weber number ( $We = \rho V^2 R_o / \gamma$ ) is considered to exhibit the effect of impact velocity. It can be seen in Figure 4 that the obtained scaling model (Equation 2) fits well with the numerical coefficients of  $2.612 \pm 0.255$  and  $2.528 \pm 0.269$ , for curved and ribbed-curved surfaces respectively, with a 95% confidence. The solid black lines in Figure 4a and b represent  $\frac{t_c}{\tau_o} = 2.612 We^{-0.12}$  and  $\frac{t_c}{\tau_o} = 2.528 We^{-0.12}$ , respectively, and the dashed green lines depict the top and bottom boundaries associated with the corresponding numerical coefficients.

$$t_c = C \tau_o We^{-0.12} \quad (2)$$

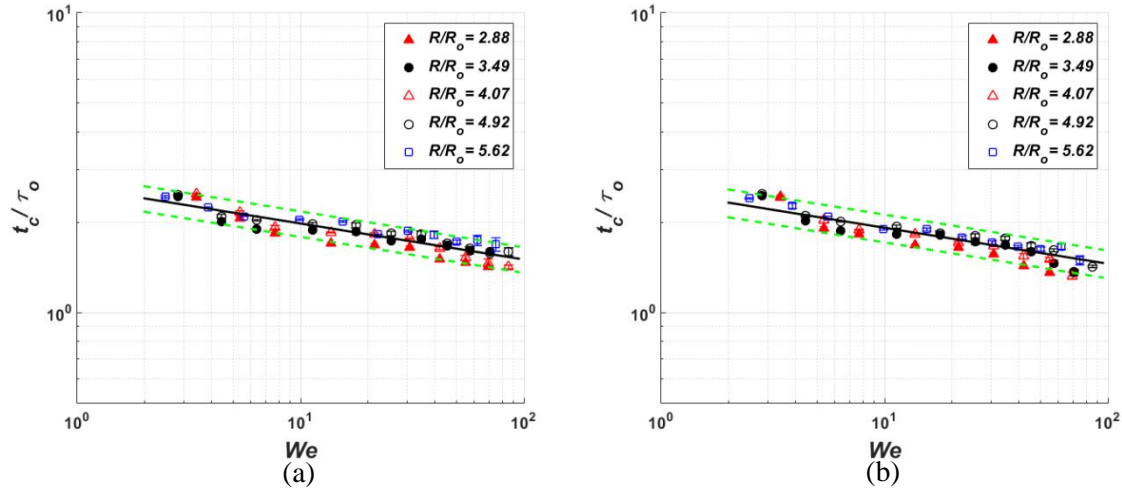


Figure 4. The relationship between contact time and Weber number for (a) smooth curved surfaces and (b) ribbed-curved surfaces.

### References:

[1] D. Khojasteh, S.M. Mousavi, R. Kamali, CFD analysis of Newtonian and non-Newtonian droplets impinging on heated hydrophilic and hydrophobic surfaces, Indian Journal of Physics 91(5) (2017) 513-520.

- [2] M. Abolghasemi, A. Keshavarz, M. Ali Mehrabian, Heat transfer enhancement of a thermal storage unit consisting of a phase change material and nano-particles, *Journal of Renewable and Sustainable Energy* 4(4) (2012) 043124.
- [3] M. Abolghasemi, A. Keshavarz, M.A. Mehrabian, Thermodynamic analysis of a thermal storage unit under the influence of nano-particles added to the phase change material and/or the working fluid, *Heat and Mass Transfer* 48(11) (2012) 1961-1970.
- [4] A. Keshavarz, M. Mehrabian, M. Abolghasemi, A. Mostafavi, Availability (exergy) analysis in a thermal energy storage system with the phase change materials arranged in series, *Proceedings of the Institution of Mechanical Engineers, Part A: Journal of Power and Energy* 225(1) (2011) 44-52.
- [5] E. Omrani, B. Barari, A.D. Moghadam, P.K. Rohatgi, K.M. Pillai, Mechanical and tribological properties of self-lubricating bio-based carbon-fabric epoxy composites made using liquid composite molding, *Tribology International* 92 (2015) 222-232.
- [6] M. Davoudi, E. Moore, G. Chase, Motion of water drops on hydrophobic expanded polymer mat surfaces due to tangential air flow, *Journal of the Taiwan Institute of Chemical Engineers* (2017).
- [7] S. Berry, J. Kedzierski, *New Methods to Transport Fluids in Micro-Sized Devices*, Citeseer, 2008.
- [8] M. Abolghasemibizaki, C.J. Robertson, C.P. Fergusson, R.L. McMasters, R. Mohammadi, Rolling viscous drops on a non-wettable surface containing both micro-and macro-scale roughness, *Physics of Fluids* 30(2) (2018) 023105.
- [9] M. Abolghasemibizaki, R.L. McMasters, R. Mohammadi, Towards the Shortest Possible Contact Time: Droplet Impact on Cylindrical Superhydrophobic Surfaces Structured with Macro-Scale Features, *Journal of Colloid and Interface Science* 521 (2018) 17-23.
- [10] K.D. Esmeryan, C.E. Castano, A.H. Bressler, M. Abolghasemibizaki, R. Mohammadi, Rapid Synthesis of Inherently Robust and Stable Superhydrophobic Carbon Soot Coatings, *Applied Surface Science* 369 (2016) 341-347.
- [11] K.D. Esmeryan, C.E. Castano, A.H. Bressler, M. Abolghasemibizaki, C.P. Fergusson, A. Roberts, R. Mohammadi, Kinetically driven graphite-like to diamond-like carbon transformation in low temperature laminar diffusion flames, *Diamond and Related Materials* 75 (2017) 58-68.
- [12] M. Abolghasemibizaki, R. Mohammadi, Droplet impact on superhydrophobic surfaces fully decorated with cylindrical macrottextures, *Journal of colloid and interface science* 509 (2018) 422-431.
- [13] Y. Liu, M. Andrew, J. Li, J.M. Yeomans, Z. Wang, Symmetry breaking in drop bouncing on curved surfaces, *Nature communications* 6 (2015) 10034-10034.